



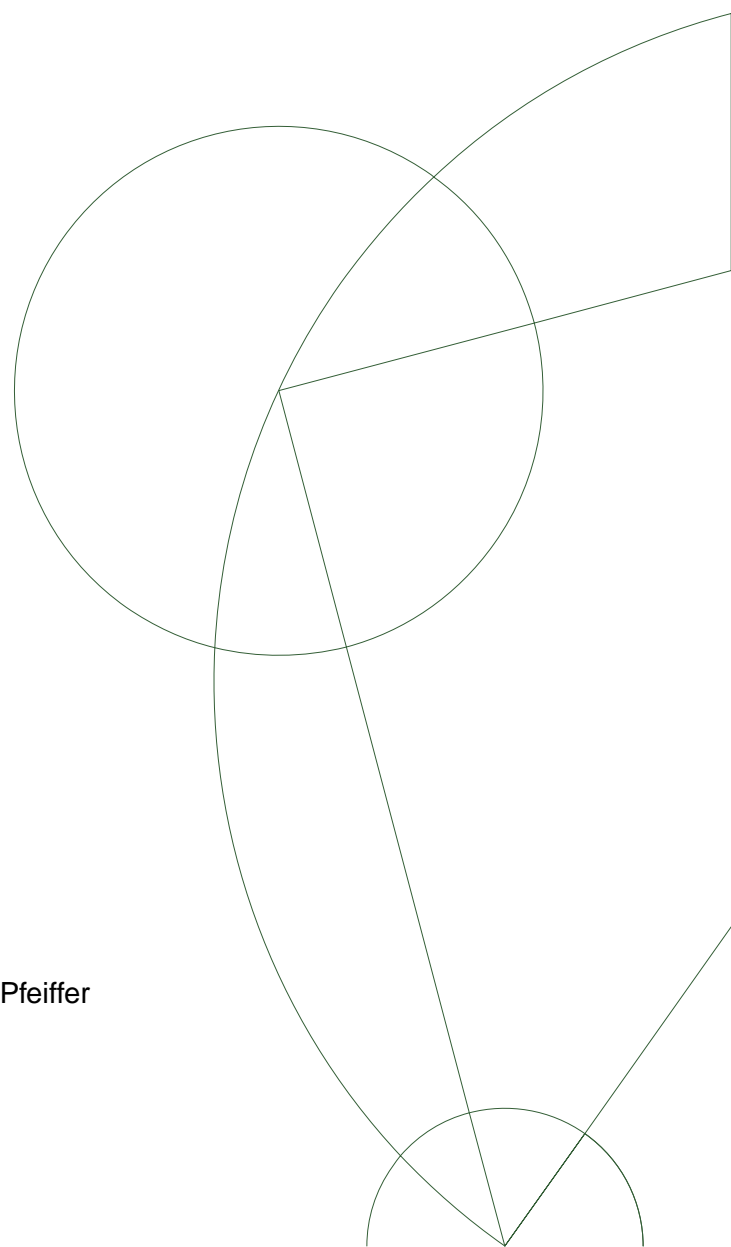
Ph.D Thesis

Martin Bech

X-ray imaging with a grating interferometer

Academic supervisors: Robert Feidenhans'l ahd Franz Pfeiffer

May, 2009



X-ray imaging with a grating interferometer

Submitted to:
The Graduate School of Science
Faculty of Science
Niels Bohr Institute
University of Copenhagen
Denmark

For the PhD degree

by

Martin Bech
Niels Bohr Institute
University of Copenhagen
Universitetsparken 5
DK-2100 Copenhagen

May 2009

Abstract

Improved contrast in X-ray images can be obtained through phase contrast and dark-field imaging. Of the different methods for phase contrast imaging, the recently developed grating based interferometer is well suited for use at different X-ray sources, including a standard X-ray tube.

This thesis explains the principles of a grating based interferometer, and the algorithms for tomographic reconstruction of differential phase contrast and dark-field images are derived. Experimental data recorded at three different X-ray sources are presented, and the data quality depending on source properties are discussed.

Dansk resumé

Siden W. C. Röntgen opdagede røntgenstrålerne i 1895, har man anvendt røntgenbilleder til medicinsk diagnose. Metoden til at tage røntgenbilleder af et objekt er at bestråle objektet med røntgen, og måle hvor meget intensitet objektet har absorberet. Denne metode har grundlæggende ikke ændret sig de sidste hundrede år.

Absorption af røntgenstråler afhænger af grundstof-sammensætningen i objektet. Knogler indeholder calcium og absorberer derfor mere end det bløde væv, som stort set kun består af lettere grundstoffer. Der kan dog være svært at skelne mellem forskellige typer blødt væv, som alle absorberer røntgenstrålerne lige meget.

For at opnå bedre kontrast i røntgenbilleder, er der i de sidste årtier udviklet forskellige metoder til at tage billeder med *fasekontrast*. Lige som i optisk mikroskopi, er fasekontrastbilleder et resultat af refraktion i objektet, og ikke absorption. Yderligere kontrast kan opnås ved at betragte spredte stråler, som man gør i mikroskoper med mørkefelt teknik.

Denne Ph.D. afhandling beskriver hvordan et gitter-interferometer kan anvendes til at tage røntgenbilleder med forbedret kontrast ved hjælp af fasekontrast og mørkefeltbilleder.

Kapitel 1 giver et overblik over forskellige metoder til at tage fasekontrast røntgenbilleder.

Kapitel 2 beskriver hvordan røntgenstråler vekselvirker med objekter, og hvordan absorption og faseforskydning af den elektromagnetiske bølle afhænger af grundstofsammensætning og fotonenergi. Der udledes et udtryk for hvordan periodiske bølger propagerer frit, og det vises at et *fasegitter* med en gitterperiode på 4 mikrometer giver anledning til et interferensmønster få centimeter bag ved gitteret. Dette interferensmønster skyldes den såkaldte Talbot effekt, og mønstret vil gentage sig periodisk ved forskellige afstande fra fasegitteret.

Ved hjælp af et *absorptionsgitter* og en røntgendetektor kan den nøjagtige position af interferensmønsteret bestemmes. Hvis et objekt placeres i røntgenstrålen, vil strålen brydes i små vinkler, som vil få interferensmønsteret til at forskyde sig. Det vil sige at brydningsindekset igennem prøven kan bestemmes ud fra mønsterets forskydning. I kapitel 2 gives også en beskrivelse af interferensmønsterets visibilitet, og hvilken indflydelse røntgenkildens størrelse har på visibiliteten.

Kapitel 3 beskriver hvordan både almindelige absorptionsbilleder, fasekontrastbilleder og mørkefeltbilleder kan konstrueres ud fra de målte interferensmønstre: Mønsterets forskydning giver et differentielt fasekontrast billede,

mønsterets visibilitet giver et mørkefeltbillede, og mønsterets middelværdi giver et almindeligt absorptionsrøntgenbillede.

Teorien bag tomografisk rekonstruktion beskrives også i kapitel 3. De almindelige algoritmer til filtreret tilbageprojektion udvides til at virke med differentiel fasekontrast, og en teori for spredningssignalet introduceres så tomografisk rekonstruktion også kan foretages med mørkefeltbilleder.

Kapitel 4 giver en række eksempler på eksperimentielle resultater med gitter-interferometeret. Der præsenteres resultater fra fire forskellige opstillinger: To ved et almindeligt røntgenapparat, en ved Compact Light Source røntgenkilden under udvikling af Lyncean Technologies Inc., og en ved synkrotronen ESRF i Grenoble. De to opstillinger ved et almindeligt røntgenapparat anvender forskellige afstande mellem gitrene, og har derfor forskellig følsomhed for fasekontrast.

Der gives både eksempler på radiografiske billeder, og på tomografiske rekonstruktioner af de tre typer billeder. Til slut sammenlignes de fire forskellige opstillinger.

Kapitel 5 opsummerer afhandlingen, og det konkluderes at der er potentielle for fasekontrast- og mørkefelt-billeder med gitterinterferometeret.

Publications on which this thesis is based

Publication I

Franz Pfeiffer, Oliver Bunk, Christian David, **Martin Bech**, Geraldine Le Duc, Alberto Bravin and Peter Cloetens

High-resolution Brain Tumor Visualization using Three-dimensional X-ray Phase Contrast Tomography

Physics in Medicine and Biology 52 (2007) 6923–6930

Publication II

Franz Pfeiffer, **Martin Bech**, Oliver Bunk, Phillip Kraft, Eric F. Eikenberry, Christian Brönnimann, Christian Grünzweig and Christian David

Hard-X-ray Dark-field Imaging using a Grating Interferometer

Nature Materials 7 (2008) 134–137

Publication III

Martin Bech, Oliver Bunk, Christian David, Phillip Kraft, Christian Brön-
nimann, Eric F. Eikenberry and Franz Pfeiffer

X-ray imaging with the PILATUS 100k detector

Applied Radiation and Isotopes 66 (2008) 474–478

Publication IV

Franz Pfeiffer, Christian David, Oliver Bunk, Tilman Donath, **Martin Bech**, Geraldine Le Duc, Alberto Bravin and Peter Cloetens

Region-of-Interest Tomography for Grating-Based X-Ray Differential Phase-Contrast Imaging

Physical Review Letters 101 (2008) 168101

Publication V

Martin Bech, Oliver Bunk, Christian David, Ron Ruth, Jeff Rifkin, Rod Loewen, Robert Feidenhans'l and Franz Pfeiffer

Hard X-ray phase-contrast imaging with the Compact Light Source based on inverse Compton X-rays

Journal of Synchrotron Radiation 16 (2009) 43–47

Publication VI

Martin Bech, Torben H. Jensen, Robert Feidenhans'l, Oliver Bunk, Christian David and Franz Pfeiffer

Soft-Tissue Phase-Contrast Tomography with X-Ray Tube Sources
Physics in Medicine and Biology 54 (2009) 2747–2753

Publication VII

Franz Pfeiffer, **Martin Bech**, Oliver Bunk, Tilman Donath, Beat Henrich, Phillip Kraft and Christian David

X-ray dark-field and phase-contrast imaging using a grating interferometer
Journal of Applied Physics 105 (2009) 102006

Acknowledgement

First of all I would like to thank my academic supervisors, Prof. Robert Feidenhans'l and Prof. Franz Pfeiffer, for their constant and persistent effords to keep me busy. I have learned a lot from you.

I would also like to thank professor emeritus Jens Als-Nielsen for answering my many questions on X-ray matter, and for asking many questions back at me.

Special thanks to Torben Haugaard Jensen, for the many great discussions we have had on X-ray topics, for his good company both in the office and at travels for X-ray experiments, and for reading the draft of this thesis.

I would like to thank all of the students and staff of the X-ray group at the Niels Bohr Institute with whom I have shared many great moments at beamtimes, in the office or elsewhere. Thank you Henrik Lemke, Simon Mariager, Andreas Kring, Sonja Rosenlund, Kristoffer 'Kreuff' Haldrup, Keld Theodor, Arvid Böttiger, Maria Thomsen, Søren Kynde, Louise Sperling. Also thanks to the Center for Molecular Movies.

During my studies I have spend some months at the Paul Scherrer Institute in the coherent scattering group. I would like to thank all the people who have helped me during my stays, in particular Franz Pfeiffer and Oliver Bunk for giving me much support and inviting me to their homes when I was far from my own. Thanks to Christian David for his great support and for sharing his knowledge, thanks to Christian Kottler, Christian Gruenzweig, Tilman Donath, Julia Herzen and Martin Dierolf for helping me with my experiments. Thanks to the Dectris group for providing a Pilatus 100k detektor.

A collaboration with the Faculty of Health Sciences and the Faculty of Pharmaceutical Sciences has been established to explore the potential of phase contrast X-ray imaging to clinical applications. Though none of the results obtained are presented in this thesis, I would like to thank the people involved for good collaboration. Thank you Liselotte Højgaard for your enthusiastic involvement and for inviting me to spend a week at the hospital learning about medical imaging at the department of Clinical Physiology and Nuclear Medicine and PET. Thank you Tina Binderup, Rie Hansen, Andreas Kjær and Anne-Marie Heegaard.

The John and Birthe Meyer Foundation is greatly acknowledged for granting funds to establish a project on phase contrast imaging at the Compact Light Source. The experiments at the Compact Light Source have only been possible due to the hard work of all the people at Lyncean Technologies Inc. A special thanks to the founders Ronald Ruth, Jeff Rifkin and Rod Loewen for inviting me to work with this exciting new X-ray source.

I would like to thank the people at ESRF who have invited me to join a collaboration to compare different methods for phase contrast imaging. Thank you Timm Weitkamp, Paola Coan and Alberto Bravin.

Finally, I would like to express my gratitude to my family for their ever lasting love and support. In particular I would like to thank Kristine Steen Jensen for always being there for me, and for helping me to improve. I love you.

A handwritten signature in black ink that reads "Martin Bech". The signature is fluid and cursive, with the first name "Martin" on top and the last name "Bech" below it.

Martin Bech

May 2009

Contents

| | | |
|----------|--|-----------|
| 1 | Introduction | 1 |
| 1.1 | Outline | 1 |
| 1.2 | General motivation | 2 |
| 1.3 | Review | 3 |
| 1.4 | Present work | 6 |
| 2 | Theory | 7 |
| 2.1 | X-ray interaction with matter | 7 |
| 2.1.1 | Refractive index | 9 |
| 2.2 | Wave-front propagation | 13 |
| 2.2.1 | The Talbot effect | 16 |
| 2.2.2 | Fractional Talbot effects | 18 |
| 2.3 | Grating interferometer | 18 |
| 2.3.1 | Plane wave | 19 |
| 2.3.2 | Magnification in curved wave setup | 24 |
| 2.3.3 | Working with incoherent sources | 25 |
| 2.3.4 | The gratings | 26 |
| 2.4 | Visibility | 27 |
| 2.4.1 | Shape of interference pattern | 27 |
| 2.4.2 | Sampling rate | 32 |
| 3 | Data analysis | 35 |
| 3.1 | Image processing | 35 |
| 3.1.1 | Three image signals | 36 |
| 3.1.2 | Linear diffusion coefficient | 42 |
| 3.1.3 | Dark-field images | 45 |
| 3.2 | Tomography | 46 |
| 3.2.1 | Absorption data | 48 |
| 3.2.2 | Differential phase data | 52 |
| 3.2.3 | Dark-field data | 55 |

| | |
|---|------------|
| 4 Results | 57 |
| 4.1 X-ray tube | 58 |
| 4.1.1 Setup | 58 |
| 4.1.2 Visibility and sensitivity | 62 |
| 4.1.3 Sample for absorption images | 67 |
| 4.1.4 Sample for phase contrast imaging | 67 |
| 4.1.5 Phase contrast tomography | 70 |
| 4.1.6 Sample for dark-field imaging | 73 |
| 4.1.7 Dark-field tomography | 75 |
| 4.2 Compact Light Source | 78 |
| 4.2.1 Source | 78 |
| 4.2.2 Grating interferometer | 80 |
| 4.2.3 Visibility | 80 |
| 4.2.4 Projection images | 81 |
| 4.3 Synchrotron data | 82 |
| 4.3.1 Source | 82 |
| 4.3.2 Gratings | 82 |
| 4.3.3 Visibility | 83 |
| 4.3.4 Projection images | 85 |
| 4.3.5 Tomography images | 87 |
| 4.4 Comparison of sources | 89 |
| 5 Conclusion | 91 |
| Bibliography | 95 |
| Publications | 101 |
| Publication I | 101 |
| Publication II | 111 |
| Publication III | 119 |
| Publication IV | 131 |
| Publication V | 137 |
| Publication VI | 145 |
| Publication VII | 155 |

Chapter 1

Introduction

The purpose of this thesis is to describe the grating interferometer and its use for X-ray phase contrast and dark-field imaging. The reader is assumed to have a basic knowledge of optics and X-ray physics, but the most necessary theory is included here.

1.1 Outline

In the quest for better contrast in X-ray imaging, a number of different phase contrast imaging techniques have been explored during the last few decades as described in section 1.3 below. The grating based interferometer is described in this work, theoretically as well as experimentally.

In chapter 2, the interaction between X-rays and matter is described from the point of view of electrons bound in atoms. Refraction is considered as a classical consequence of the electrons vibrating in the electromagnetic field of the X-ray wave, while photoelectric absorption is considered as a quantum effect where the photon is absorbed and an electron is emitted from the atom.

The propagation of X-rays in free space is also important, and the formalism of a Fourier space propagation is derived. In terms of this formalism, the Talbot effect is seen as a periodic temporal revival of a spatially periodic wavefunction.

Practical implementation of the Talbot effect in an experimental setup is described, and the actual visibility of the interference pattern in the practical case of a finite source size is derived.

Chapter 3 describes how the three types of image contrast are extracted from the recorded frames during a phase stepping scan, and how these image

signals can be tomographically reconstructed in order to obtain quantitative three-dimensional volumes from projection images.

The reconstructed quantities are the real and the imaginary part of the refractive index for phase contrast and absorption contrast, respectively. For dark-field tomography, the reconstructed quantity is a *linear diffusion coefficient* which is introduced in section 3.1.2.

Experimental results are presented in chapter 4. Most of the results presented are obtained at a standard X-ray tube, where a source grating ensures a sufficient transverse beam coherence for grating interferometry. Projection images and tomographic reconstructions of different samples illustrate the convenience of having three different contrast modalities, rather than only the standard one.

Images obtained at the European Synchrotron Radiation Source (ESRF) and at the Compact Light Source (CLS) are also presented, and the interference quality in terms of visibility is compared.

Finally, the thesis is concluded in chapter 5, where a brief perspective of grating based X-ray imaging is given.

This thesis is meant as a review of the grating interferometer technique. Though some of the results covered in this work have already been published, the overlap between the results presented here and the published results has been kept at a minimal level, such that additional information can be gained from reading the publications.

The peer-reviewed articles listed in the preamble are attached at the end of this thesis.

1.2 General motivation

Medical imaging is the most common use of X-rays today, including single image diagnostic examinations such as an X-ray image of a broken arm, the lungs, a tooth at the dentist, or mammography screening. Additionally, three dimensional imaging with X-rays are made in a CT (*or CAT*) scanner, reconstructing a volume by Computed Tomography (*or Computed Axial Tomography*). But of course X-rays are used in many applications other than clinical. Such as security screening in the airports, quality control on industrial production lines, and for scientific applications. The primary focus of this thesis is medical imaging, but the theory and conclusions apply as well for many other applications where X-ray imaging is involved.

In the field of visible light microscopy, a number of different techniques exists to produce enhanced image contrast. These techniques include phase contrast and dark-field imaging, where the optical elements of the microscope are rearranged to provide an image different from the standard transmission image.

Likewise, different imaging techniques are sought in the field of X-ray imaging to complement the well known absorption based X-ray image. The development of new contrast techniques has however been limited by the fact that production of X-ray optics is a very challenging task, opposed to optics for visible light and electron beams.

1.3 Review of phase contrast imaging

Crystal interferometer. During the last few decades a number of different approaches to phase contrast X-ray imaging have been reported. A crystal interferometer was presented by Bonse & Hart (1965), based on three silicon beam splitters in Laue geometry that split, redirect and recombine the X-ray beam, see figure 1.1. Figure of all methods A sample is placed in one beam path, and when the split beam is recombined, the phase shift induced by the sample will produce an interference pattern from which the phase shift can be extracted. The experimental results reported show very high phase sensitivity and good image quality, within the limitations of the technique. The beam quality requirements are not very strict, but the silicon crystals act as monochromator selecting a narrow spectral width. Hence a very intense beam is required to reduce exposure time.

The high sensitivity can be used to study small soft tissue samples as done by Momose & Fukuda (1995), and even phase tomography is possible with the crystal interferometer (Beckmann et al. 1997, Momose et al. 2003a). The interferometer is however also very sensitive to mechanical instabilities if the three beam splitters are made from different pieces of silicon crystal (Momose et al. 2001). If, on the other hand, the beam splitters are made from a single crystal, the sample to be investigated can be no larger than the silicon single crystal.

Due to the high sensitivity and limitations to sample size, the crystal interferometer is well suited for high resolution imaging at synchrotron sources where the requirement of high beam intensity is met.

Propagation based imaging. A different approach to phase imaging is propagation based phase contrast (Snigirev et al. 1995). The propagation based imaging (PBI) is in many senses the simplest kind of phase contrast

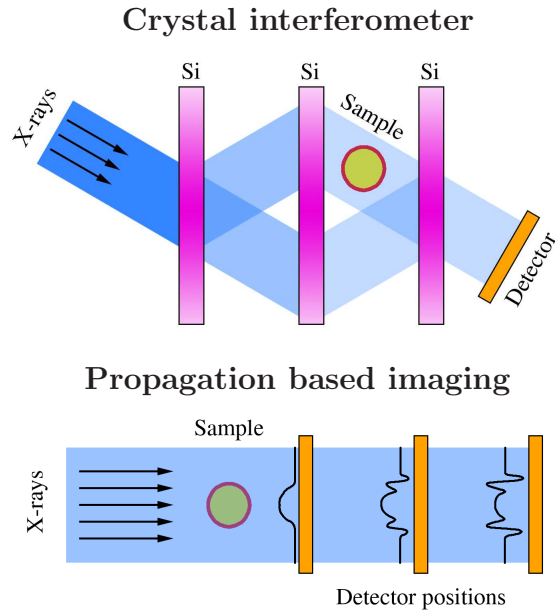


Figure 1.1. Schematic drawings of crystal interferometer and propagation based imaging.

imaging, as no optical elements are required in the beam and the constraint on spectral width is relaxed (Wilkins et al. 1996, Cloetens et al. 1999a). PBI rely on interference fringes arising in the free space propagation in the Fresnel regime, as illustrated in figure 1.1. The measured intensity fringes is thus not a direct measure of the phase like the crystal interferometer, but rather the Laplacian of the phase front (Cloetens et al. 1997).

In order to achieve interference of the propagating beam, a very high degree of spatial coherence is required, and a high resolution detector is needed to observe the fringes. A series of images is then recorded at different propagation distances in order to unambiguously determine the phase of the wave front.

This method is particularly good at edge enhancement, and is hence well suited for *e.g.* fiber samples, foam or localization of inhomogeneities in metals (Cloetens et al. 1999b) also in tomography setup. But for imaging of soft tissue and small density variations this method is not optimal (Nesterets & Wilkins 2008).

Analyzer based imaging. A third approach is analyzer based imaging (ABI) or diffraction enhanced imaging (DEI) where the first derivative of the phase front is measured by detecting refraction angles (Ingal & Beliaevskaya

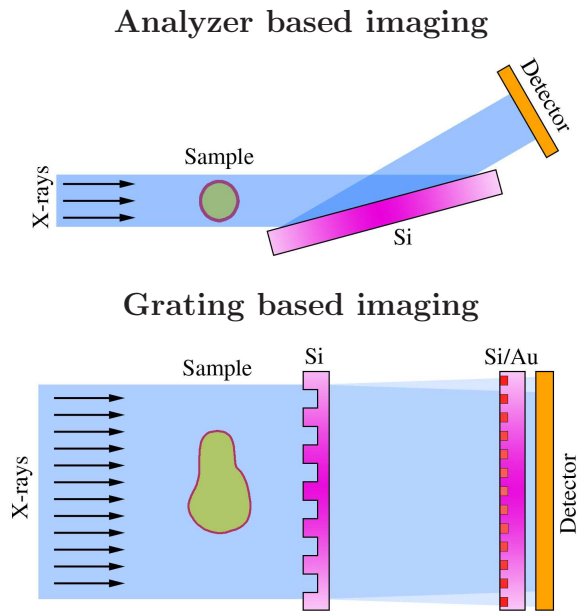


Figure 1.2. Schematic drawings of analyzer based imaging and grating based imaging.

1995, Davis et al. 1995). This method uses a single or a double crystal in Bragg geometry as a collimator to produce a parallel beam (not shown in the figure). The parallel beam penetrates the sample and is then analyzed by a second Bragg crystal that reflects the beam onto a detector (Bravin 2003), see figure 1.2. The incidence angle of the analyzer crystal can be slightly detuned such that the refracted part of the beam is reflected onto the detector. When the angular detuning is varied (analyzer grating is rocked) different refraction angles are analyzed (a rocking curve is recorded). A full data set contains images from several positions on the rocking curve.

ABI has the advantage of high phase sensitivity, though only in the direction perpendicular to the analyzer crystal. At the same time as a phase contrast image can be obtained from the shift of the rocking curve, the shape of the rocking curve can produce a kind of dark-field image of the scattered X-rays (Zhong et al. 2000, Wernick et al. 2003).

Grating based imaging. Grating based imaging (GBI) or shearing interferometry is a fourth approach to phase contrast imaging (Clauser 1998). It is related to the crystal interferometer in the sense that it consists of a beam splitter and a beam analyzer, and GBI is related to ABI by the fact that the first derivative of the phase front is measured, and that dark-field imaging

is possible. GBI has previously been applied to visible light phase contrast (Lohmann & Silva 1971), and has recently been applied to X-ray imaging as well (David et al. 2002, Momose et al. 2003a, Pfeiffer et al. 2006).

The beam splitter grating splits the beam by diffraction, but the diffraction orders are separated by less than a milli-radian, and the diffracted beams are hence not spatially separated, but will interfere to create an intensity pattern downstream of the beamsplitter at a distance defined by the Talbot effect (Talbot 1836, Weitkamp et al. 2005), see figure 1.2. Refraction in a sample is measured by detecting the transverse shift of the interference pattern with a high resolution detector (Takeda et al. 2007) or an analyzer grating.

Tomographic reconstruction of the differential phase is possible even without initial integration to retrieve the quantitative phase shift (Pfeiffer et al. 2007b), and this kind of tomographic reconstruction has turned out to be an advantage to local tomography (see publication IV, Pfeiffer et al. (2008b)).

1.4 Present work

The work of this thesis is carried out on a GBI setup where the beam splitter grating is a pure phase grating giving intensity oscillations which are analyzed with an absorption grating at a fractional Talbot distance. The gratings for this work were all made at the Poul Scherrer Institut (PSI) by Christian David and Christian Gruenzweig (David et al. 2002, 2007a), and the exploration of GBI with these gratings has been carried out as a collaboration between the groups of Christian David (Laboratory for Micro and Nanotechnology) and Franz Pfeiffer (Swiss Light Source) at PSI (Pfeiffer et al. 2005, 2006, 2007a,b, Kottler et al. 2007, David et al. 2007b, Engelhardt et al. 2007, 2008).

The publications attached to this thesis (Pfeiffer et al. 2007, 2008a,b, 2009, Bech et al. 2008, 2009a,b) contain parts of the work presented here, but sections 3.1.2 and 3.1.3 on dark-field imaging described in terms of a *linear diffusion coefficient* is still unpublished, and section 2.4 on recorded visibility as a function of source size is also unpublished though build on a published work by Weitkamp et al. (2006). The experimental results presented in section 4.1.2 comparing first with the fifth fractional talbot distance and different sample positions between the gratings, and section 4.1.7 on dark-field tomography are also currently unpublished.

Chapter 2

Theory

When X-rays penetrate matter, both the amplitude and the phase of the electromagnetic wave describing the X-ray beam are affected. The amplitude gets attenuated and the phase get shifted. Either effect can potentially be used for imaging. But a detector will only measure the intensity of the beam; it is not possible to measure the phase of a photon directly. In order to do phase contrast imaging, it is thus necessary to rely on interference effects.

The theory of how X-ray radiation interacts with matter, and how this interaction can be used for imaging, is described here.

2.1 X-ray interaction with matter

The most common known X-ray property is probably the ability to penetrate matter. Because of this ability, medical doctors can look at bones by taking an X-ray image. The low absorption of X-rays in matter, gives the ability to penetrate. But at the same time we rely on absorption to give image contrast. The concept of phase contrast imaging is to make images from all the penetrated X-rays, such that no X-rays need to be absorbed in order to produce an image.

Due to the wave-particle duality, it may be instructive to consider both wave and particle properties of X-rays. The wavelength of visible light is relatively long, compared to the extent of an atom, and to understand the interaction between visible light and matter, the light must be considered as waves. The reason why X-rays penetrate materials where visible light is absorbed, can be explained by considering the frequency of the electromagnetic wave, and how the field interacts with the dipoles made up of electrons bound to nuclei. Because of the long wavelength of visible light, it is appropriate to consider the atoms classically as an oscillator that can be driven

| Metal | ν_p [Hz] |
|-----------|-----------------------|
| Lithium | 1.94×10^{15} |
| Sodium | 1.43×10^{15} |
| Potassium | 0.95×10^{15} |
| Rubidium | 0.88×10^{15} |

Table 2.1. *Plasma frequencies for some alkali metals (Hecht 2002)*

by the incoming electromagnetic field. This oscillator will have a resonance frequency, that in turn determines the optical properties of the material. In the wave regime, we can compare the frequencies of visible light with X-ray frequencies. Though both visible light and X-rays are electromagnetic radiation, the frequency domain of X-rays ($> 10^{18}$ Hz) is much higher than the frequencies of visible light ($< 10^{15}$ Hz), and in particular the X-ray frequencies are above the resonance frequencies of the considered classical oscillators. Similarly, in metals the optical properties are determined by the plasma frequencies (Hecht 2002). Table 2.1 lists the plasma frequencies of some alkali metal. For visible light with frequencies below the plasma frequency, the index of refraction has a large imaginary part, and the light is absorbed. For X-rays with frequencies above the plasma frequency, the index of refraction has a low imaginary part and the X-rays penetrate.

For X-rays, the wavelength is comparable to the size of an atom, and the wave formalism is no longer adequate. In addition, the particle picture is needed to describe the interaction between X-rays and matter. To describe a quantum mechanical process such as the photoelectric effect, we need to consider an X-ray to be a quantum (a photon) with a certain energy. As opposed to visible photons with energies in the 1 eV range, X-ray photons have energies in the range from 1 keV to 100 keV. As the binding energy of electrons to atoms is of the same magnitude, an X-ray photon can be absorbed by the release of an electron. The binding energy defines an absorption edge, in the sense that an X-ray photon with energy below the binding energy is not absorbed by the electron, whereas an X-ray with a higher energy may be subject to photoelectric absorption with a finite probability.

Scattering is another process in the interaction between X-rays and matter. As opposed to a photon subject to photoelectric absorption, a scattered photon is not absorbed, but merely gets its wave vector changed from \bar{k} to \bar{k}' . Scattering of an X-ray photon can be elastic (*i.e.* the energy of the ph-

ton remains unchanged, known as Thomson scattering) or inelastic (*i.e.* the energy of the photon is changed, known as Compton scattering).

At photon energies far from the absorption edges, the interaction cross section of X-rays with matter decreases with increased photon energy. This goes both for photoelectric absorption and for scattering. *I.e.* higher photon energies give larger penetration depth.

In medical X-ray imaging, the photon energy ranges from 20 keV all the way up above 100 keV. At these energies there are no absorption edges, as the body is made up of light elements with absorption edges well below 20 keV. All electrons then contribute to the scattering and absorption cross-sections. For absorption, the magnitude of the interaction cross-section depends on the photon energy and on the charge of the nucleus to which the electron is bound. The absorption based image contrast is thus a linear combination of the densities of each element in the sample. In the case of coherent scattering, we may consider all electrons to contribute evenly to the interaction with the X-ray photon, giving a linear dependence on the electron density of the sample. In other words, what we measure with an X-ray phase contrast image, is in fact the integrated electron density along the optical axis of the imaging system.

In soft tissue, the primary atomic elements to consider are oxygen, carbon and hydrogen, whereas bones contain large amounts of calcium with a much higher atomic number. This is why a normal X-ray image shows good contrast between bones and soft tissue. The problem with absorption based X-ray imaging, is that it can be very difficult to distinguish different kinds of soft tissue as they may have very similar absorption coefficients. A higher contrast can be obtained by phase contrast imaging instead of the absorption based contrast, as this thesis (among others) illustrates.

The mechanisms behind standard X-ray imaging and phase contrast imaging can be explained by the complex refractive index of the sample.

2.1.1 Refractive index

As in the case with optical light, the interaction between X-ray and matter depends on the wavelength, or photon energy, of the electromagnetic radiation. For simplicity, we shall consider a monochromatic beam in the following. The theory can easily be expanded to include polychromatic beams, by considering the polychromatic beam as a superposition of monochromatic beams.

When calculating refraction effects of X-rays penetrating matter, one can calculate both absorption and phase shift of the X-ray wave from the complex index of refraction n . In homogeneous media with a nonzero electron density,

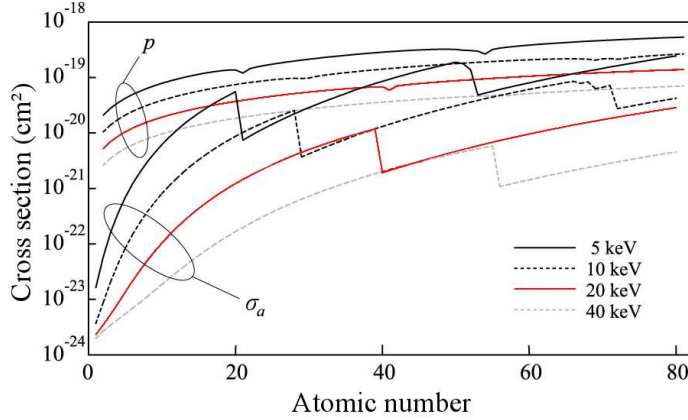


Figure 2.1. Absorption cross-section σ_a and phase shift cross-section $p = 2\pi Zr_0/k$ as a function of element number Z . The red curves indicate a 20 keV photon energy which is a minimum for medical imaging. Figure adapted from Momose et al. (2001).

the refractive index is usually written as $n = 1 - \delta + i\beta$, where δ is given by

$$\delta = 2\pi\rho_a Z r_0 / k^2 \quad (2.1)$$

where ρ_a is the atomic number density*, Z is the atomic number, $r_0 = 2.82 \times 10^{-5} \text{ \AA}$ is the Thomson scattering length (classical electron radius), and $k = |\vec{k}| = 2\pi/\lambda$ is the length of the wave vector. The imaginary part β is given by

$$\beta = \frac{\rho_a \sigma_a}{2k}. \quad (2.2)$$

where the absorption cross-section σ_a is discontinuous at the absorption edges.

Figure 2.1 displays the absorption cross-section σ_a and a phase shift cross-section $p = 2\pi Zr_0/k$ at several different photon energies as a function of element number Z . We see that the phase shift cross-section is three orders of magnitude larger than the absorption cross-section at low atomic numbers, which is an indication that phase contrast imaging is more sensitive to density variations than standard absorption X-ray imaging.

The discontinuities of the absorption cross-section makes the absorption response to energy differences quite different from the phase shift response

*Close to absorption edges, the index of refraction should be corrected by the dispersion correction f' such that $\delta = 2\pi\rho_a(Z + f')r_0/k^2$, see (Als-Nielsen & McMorrow 2001). Far from the edges equation 2.1 is valid, and $\rho_a Z = \rho_e$ the electron density.

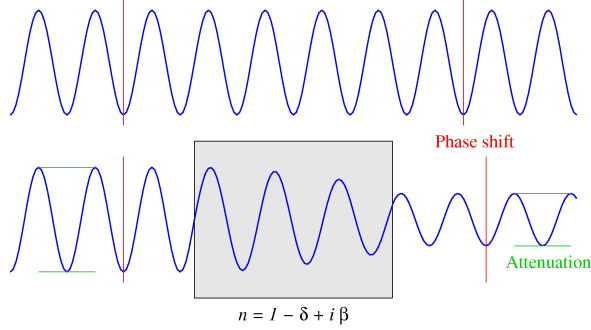


Figure 2.2. Phase shift and attenuation of a wave in a medium. Inside the medium with refractive index $n = 1 - \delta + i\beta$ the wave get phase shifted with respect to the wave propagating in free space, as indicated by red lines, and attenuated, as indicated by green lines.

which is continuous. For comparison, let us assume for a given element and a given X-ray beam that the photon energy is above all absorption edges of the element. For light elements ($Z < 40$) this is the case at photon energies above 20 keV (red curve in figure 2.1). In this case all electrons come into play for photoelectric absorption, and σ_a is approximately given by

$$\sigma_a = 0.02[\text{barn}] \left(\frac{k_0}{k} \right)^3 Z^4 \quad (2.3)$$

where k_0 is the length of the wavevector of a 1 Å photon, and Z is the atomic number of the absorbing atom (Als-Nielsen & McMorrow 2001). Comparing equations 2.1-2.3 we see that δ is proportional to Z/k^2 , while β is proportional to Z^4/k^4 . *I.e.* at higher energies the advantage of phase contrast imaging grows.

To see the effect of the refractive index, consider a wave propagating through a medium. The propagation of an electromagnetic wave through a medium with index of refraction n is described by:

$$\Psi(\bar{r}) = E_0 e^{in\bar{k}\cdot\bar{r}} = E_0 e^{i(1-\delta)\bar{k}\cdot\bar{r}} e^{-\beta\bar{k}\cdot\bar{r}} \quad (2.4)$$

In vacuum, the index of refraction is unity, and hence the propagation of a plane wave in vacuum can be described by:

$$\Psi(\bar{r}) = E_0 e^{i\bar{k}\cdot\bar{r}} \quad (2.5)$$

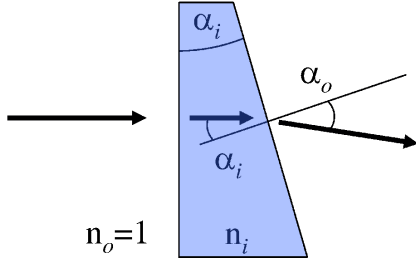


Figure 2.3. Refraction in a wedge. The direction of the beam is perpendicular to the first surface of the wedge, and there is no angular refraction. At the second surface the incident angle α_i is 1° . The index of refraction outside the wedge n_o is unity in free space. For visible light $\alpha_o > \alpha_i$, for X-rays $\alpha_o < \alpha_i$.

As illustrated in figure 2.2 a wave travelling through a medium with refractive index n is both attenuated and phase shifted relative to a ray traveling through vacuum. The phase shift, indicated by red lines in figure 2.2, is given by

$$\Delta\Phi = \delta\bar{k} \cdot \bar{r} \quad (2.6)$$

and the intensity, indicated by green lines in figure 2.2, is given by the square of the wave amplitude

$$\begin{aligned} I &= |E_0 e^{-\beta kr}|^2 \\ &= I_0 e^{-2\beta kr} \\ &= I_0 e^{-\mu r} \end{aligned} \quad (2.7)$$

where $\mu = 2k\beta$ is the *linear absorption coefficient*.

To compare the refraction of X-rays travelling through silicon with that of visible light refracted in a glass lens (silicon oxide) consider the following case: A ray penetrates a wedge shaped object as illustrated in figure 2.3. The surfaces of the wedge meet at an angle chosen to be $\alpha_i = 1^\circ$. From Snell's law we can calculate the refraction angle α_r for visible light refracted in a wedge surrounded by vacuum with $n_o = 1$:

$$n_i \sin(\alpha_i) = n_o \sin(\alpha_o) \quad (2.8)$$

$$\alpha_o \approx n_i \alpha_i, \quad (2.9)$$

$$\begin{aligned} \alpha_r &= \alpha_o - \alpha_i \\ &\approx \alpha_i(n_i - 1) \end{aligned} \quad (2.10)$$

i.e. for a wedge with refractive index $n_i = 1.5$, we get $\alpha_r = 0.5^\circ$. For X-rays

with $\lambda = 1 \text{ \AA}$ the real part of the refractive index is $n_i = 1 - \delta$, where

$$\delta = 2\pi\rho_e \frac{r_0}{k^2} \quad (2.11)$$

$$= 2\pi 0.70[\text{\AA}^{-3}] \frac{2.82 \times 10^{-5}[\text{\AA}]}{(2\pi[\text{\AA}^{-1}])^2} = 3.14 \times 10^{-6}. \quad (2.12)$$

Here $\rho_e = 0.70 \text{ \AA}^{-3}$ is the electron density of silicon and $k = 2\pi\text{\AA}^{-1}$ is the wavenumber of X-rays with 1 \AA wavelength. The refraction angle is then

$$\alpha_r \approx \alpha_i(n_i - 1) \quad (2.13)$$

$$= -\alpha_i\delta \quad (2.14)$$

$$= -3.14 \times 10^{-6}[\text{ }^\circ] = -54.8 \times 10^{-9}[\text{rad}], \quad (2.15)$$

i.e. five orders of magnitude smaller for X-rays than for light. Note that the refraction angle for X-rays is negative due to the index of refraction being less than one. A refraction angle of 0.5° is easy to detect, but refraction angles in the nano-radian range make more of a challenge. X-rays with a 1 \AA wavelength will not penetrate much tissue, so higher energies (shorter wavelengths) is needed to do X-ray imaging of tissue samples thicker than 10 mm. At higher energies the refraction angles become even smaller, as δ scales inversely with the energy squared.

All methods to detect refraction angles from soft tissue rely on the wave properties of the X-rays. This is also the case for the grating interferometer, where the position of an interference pattern is used to get information on the refraction in an object.

2.2 Wave-front propagation

The idea of an X-ray image can be described shortly like this: "You shine X-rays onto a sample, and then you record what comes out on the other side". As described above, the wavefront will change inside the sample due to the interaction with matter. But the wavefront also changes during propagation through free space. To be able to get quantitative information about the sample measured, we need to know what happened to the X-ray wavefront as it propagated from the sample to the detector. In the case of standard X-ray imaging, the detector or image plate is positioned immediately behind the sample, and it is safe to assume that nothing happened to the X-ray wavefront during the free space propagation from sample to detector. But for phase-contrast imaging, the free space propagation is important. In the

near-field regime (Fresnel regime), a propagated wave-front may be calculated using Huygens-Fresnel principle, stating that a wavefront may at any given moment be considered as the sum of spherical wavelets distributed on the wave-front. As a consequence, one can calculate the wave-front at a later point, as the integrated contribution of all these wavelets. This is known as the Fresnel diffraction integral:

$$\Psi(x, y, z) = \frac{e^{ikz}}{i\lambda z} \iint \Psi(x_0, y_0, 0) e^{\frac{ik}{2z}[(x-x_0)^2 + (y-y_0)^2]} dx_0 dy_0 \quad (2.16)$$

where x_0 and y_0 are the x and y values in the plane $z = 0$. An intuitive way to propagate a wave-front in the Fresnel regime, is to consider the Fresnel diffraction integral as convolution between the wave-function Ψ in the plane $z = z_0$, and a propagator function $h_d(x, y) = (e^{ikd}/i\lambda d) e^{ik(x^2+y^2)/2d}$. We may then make use of the convolution theorem, stating that the Fourier transform of the convolution of two functions, is equal to the product of each functions Fourier transform:

$$\mathcal{FT}\{f(x, y) \otimes g(x, y)\} = \mathcal{FT}\{f(x, y)\} \mathcal{FT}\{g(x, y)\} \quad (2.17)$$

where \otimes is the convolution operator.

In other words, we may propagate the wave-front a given distance by simple multiplication in Fourier space. The Fourier space propagator function is simply the Fourier transform $\tilde{h}_d(u, v)$ of the real-space propagator function $h_d(x, y)$, but it can also be deduced from simple physical considerations.

In the following text, a Fourier space propagator function $\tilde{P}_d(k_x, k_y)$ will be deduced, and it will be shown that it is in fact the Fourier transform of $h_d(x, y)$.

To illustrate wave propagation in Fourier space, let us consider the following example: First consider a plane wave propagating in vacuum in the positive z -direction. See the incident wave on figure 2.4. Without loss of generality, we may assume the wave to be monochromatic. In this case the wave can be described by:

$$\Psi(\bar{r}) = E_0 e^{i\bar{k} \cdot \bar{r}} = E_0 e^{i\frac{2\pi z}{\lambda}} \quad (2.18)$$

In a certain plane, $z = z_0$, perpendicular to the direction of propagation, the phase is constant $\Phi = 2\pi z/\lambda$.

If we then consider the wave after it has passed through a sample (see the outgoing wave on figure 2.4), the wave is no longer a single plane-wave, but must be considered as superposition of plane waves travelling in different directions. For simplicity, let's assume that the sample is a pure phase object,

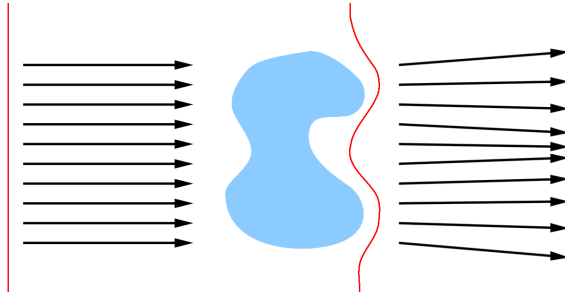


Figure 2.4. Illustration of X-rays penetrating a phase object. The incoming wave has a plane wavefront described by a single wave vector. The outgoing wave is a superposition of wave vectors pointing in different directions.

i.e. there is no absorption and no incoherent scattering. If the wavefront in the plane $z = z_0$ is Ψ_0 , then the Fourier transform pair of the wavefront is:

$$\tilde{\Psi}_0(k_x, k_y) = \iint \Psi_0(x, y) e^{-i(k_x x + k_y y)} dx dy \quad (2.19)$$

and

$$\Psi_0(x, y) = \frac{1}{(2\pi)^2} \iint \tilde{\Psi}_0(k_x, k_y) e^{i(k_x x + k_y y)} dk_x dk_y. \quad (2.20)$$

It directly shows, that the wavefront Ψ_0 at $z = z_0$ can be considered as a superposition of plane waves with x and y components k_x and k_y . As the wave is assumed to be monochromatic, we know the magnitude of the wavevector $k = 2\pi/\lambda$, and we can calculate the z component:

$$k_z = \sqrt{k^2 - k_x^2 - k_y^2}. \quad (2.21)$$

We can now propagate the wavefront a distance $\bar{r}_d = (0, 0, d)$ in the z-direction. This is simply done by propagating each plane wave from the superposition above, which is done by adding the phase factor $\exp(i\bar{k} \cdot \bar{r}_d) = \exp(ik_z d)$ from equation 2.18:

$$\Psi_d(x, y) = \frac{1}{(2\pi)^2} \iint \tilde{\Psi}_0(k_x, k_y) e^{ik_z d} e^{i(k_x x + k_y y)} dk_x dk_y. \quad (2.22)$$

In the case where all plane waves are traveling at small angles to the optical axis, we may approximate the expression for k_z by the Taylor series of the square root:

$$k_z = k \sqrt{1 - \frac{k_x^2}{k^2} - \frac{k_y^2}{k^2}} \approx k - \frac{k_x^2 + k_y^2}{2k}. \quad (2.23)$$

This is known as the paraxial approximation and is valid when $k_x^2 + k_y^2 \ll k^2$, *i.e.* when the refraction angles are small, which is true in the current case of X-ray refraction. The paraxial approximation is also assumed to hold in the Fresnel diffraction integral.

Substituting the approximate expression of k_z into equation 2.22, we get the following expression for Ψ_d :

$$\Psi_d(x, y) = \frac{1}{(2\pi)^2} \iint \tilde{\Psi}_0(k_x, k_y) e^{ikd} e^{-id(k_x^2 + k_y^2)/2k} e^{i(k_x x + k_y y)} dk_x dk_y, \quad (2.24)$$

and we can now define the Fourier space propagator function $\tilde{P}_d(k_x, k_y)$ as

$$\tilde{P}_d(k_x, k_y) \equiv e^{ikd} e^{-id(k_x^2 + k_y^2)/2k} = e^{ikd} e^{-i\pi\lambda d(\lambda_x^{-2} + \lambda_y^{-2})}, \quad (2.25)$$

where λ_x and λ_y are the spatial frequencies corresponding to k_x and k_y . That this is in fact the Fourier transform of the real-space propagator function $h_d(x, y)$ can easily be seen:

$$\begin{aligned} P_d(x, y) &= \frac{1}{(2\pi)^2} \iint \tilde{P}_d(k_x, k_y) e^{i(k_x x + k_y y)} dk_x dk_y \\ &= \frac{1}{(2\pi)^2} \iint e^{ikd} e^{-id(k_x^2 + k_y^2)/2k} e^{i(k_x x + k_y y)} dk_x dk_y \\ &= \frac{1}{i\lambda d} e^{ikd} e^{ik(x^2 + y^2)/2d} \\ &= h_d(x, y) \end{aligned} \quad (2.26)$$

where the integration is simply evaluated as a the Fourier transform of a Gaussian shape.

2.2.1 The Talbot effect

With the Fourier space propagator function $\tilde{P}_d(k_x, k_y)$ at hand, it is easy to evaluate the wavefront after any given propagation distance. In particular when operating with simple wave functions, such as periodic functions, general expressions can be made about the resulting propagation.

Henry Fox Talbot discovered in 1836 (Talbot 1836) that a periodic wave-front will repeat itself after a certain propagation distance, known as the Talbot distance. This periodic revival of a wave-function in time and space was explained by Lord Rayleigh in 1881 (Rayleigh 1881), and has later also been known as quantum revivals due to the similar behaviour of quantum mechanical wave functions in periodic potentials (Mack et al. 2002). As can be read from the citation below, Talbot used a grating and visible light to produce a periodic wave-front.

About ten or twenty feet from the radiant point, I placed in the path of the ray an equidistant grating made by Fraunhofer, with its lines vertical. I then viewed the light which had passed through this grating with a lens of considerable magnifying power. The appearance was very curious, being a regular alternation of numerous lines or bands of red and green colour, having their direction parallel to the lines of the grating. On removing the lens a little further from the grating, the bands gradually changed their colours, and became alternately blue and yellow. When the lens was a little more removed, the bands again became red and green. And this change continued to take place for an indefinite number of times, as the distance between the lens and grating increased. In all cases the bands exhibited two complementary colours. It was very curious to observe that though the grating was greatly out of the focus of the lens, yet the appearance of the bands was perfectly distinct and well defined.

Henry Fox Talbot, Philosophical Magazine, 1836

When we apply the Fourier transformation to the periodic wave in order to propagate it, we can calculate the Talbot distance d_T where the wavefront is reconstructed. The Fourier transform of a periodic function with period p is discrete, as only the Fourier components at $k_x = 2\pi m/p$ are non-zero. It can thus be described as a sum rather than an integral. For simplicity, let us consider the one-dimensional case:

$$\begin{aligned}\Psi_0(x) &= \frac{1}{2\pi} \int \tilde{\Psi}_0(k_x) e^{ik_x x} dk_x \\ &= \frac{1}{2\pi} \sum_m \tilde{\Psi}_0(2\pi m/p) e^{i2\pi xm/p} \Delta k_x,\end{aligned}$$

where $\Delta k_x = 2\pi/p$. The discrete nature of the Fourier series also has an effect on the Fourier space propagator function $\tilde{P}_d(k_x, k_y)$ in the following way:

$$\begin{aligned}\tilde{P}_d(k_x = 2\pi m/p) &= e^{ikd} e^{-idk_x^2/2k} \\ &= e^{ikd} e^{-i\frac{\lambda d}{4\pi} \left(\frac{2\pi m}{p}\right)^2},\end{aligned}$$

and we can see that at the distance $d_T = 2p^2/\lambda$, apart from a constant phase

factor the wavefront repeats itself:

$$\begin{aligned}\tilde{P}_{d_T}(2\pi m/p) &= e^{ikd_T} e^{-i\frac{\lambda}{4\pi} \frac{2p^2}{\lambda} \left(\frac{2\pi m}{p}\right)^2} \\ &= e^{ikd_T} e^{-i2\pi m^2} \\ &= e^{ikd_T}.\end{aligned}$$

It is important to note, that this expression for the Talbot distance has been calculated without any knowledge about the wave-front except that it is periodic with period p . In the case of a well known wave-function, such as a step-function induced by a grating, we may find patterns at fractional Talbot distances.

2.2.2 Fractional Talbot effects

Simulations of wave propagation after different kinds of gratings show that intensity patterns will arise at certain fractional Talbot distances. Figure 2.5 show the intensity pattern after a phase grating where 30% of the grating gives a phase shift of π and 70% of the grating gives no phase shift. From the figure it is obvious that there is a revival of the wave function at the Talbot distance $d_T = 2p^2/\lambda$, but one also notes that an exact copy of the wave-front appears at half the Talbot distance $d = p^2/\lambda$ except for a transverse shift of half the grating period. As the grating in the current example is a pure phase grating, the intensity distribution across the grating is constant, and consequently the intensity is constant at any Talbot distance or half Talbot distance $d = mp^2/\lambda$. However, at other fractional talbot distances one can observe areas of high and low intensity. A complete list of fractional Talbot distances produced by binary phase gratings is given by Suleski (1997). The exact position of the intensity maxima may be measured, and this is the basic idea behind the grating interferometer for phase contrast imaging.

2.3 Grating interferometer

The concept of phase contrast imaging is to measure the refractive index of the sample. In order to measure the index of refraction of a sample, we need to measure the angle of refraction of a transmitted X-ray wave. The idea of using a grating interferometer to measure refraction angles, is that a slight angular change to an incoming wave-front will lead to a transverse displacement of the interference pattern produced by the grating. The following section will introduce how the grating interferometer is practically used to

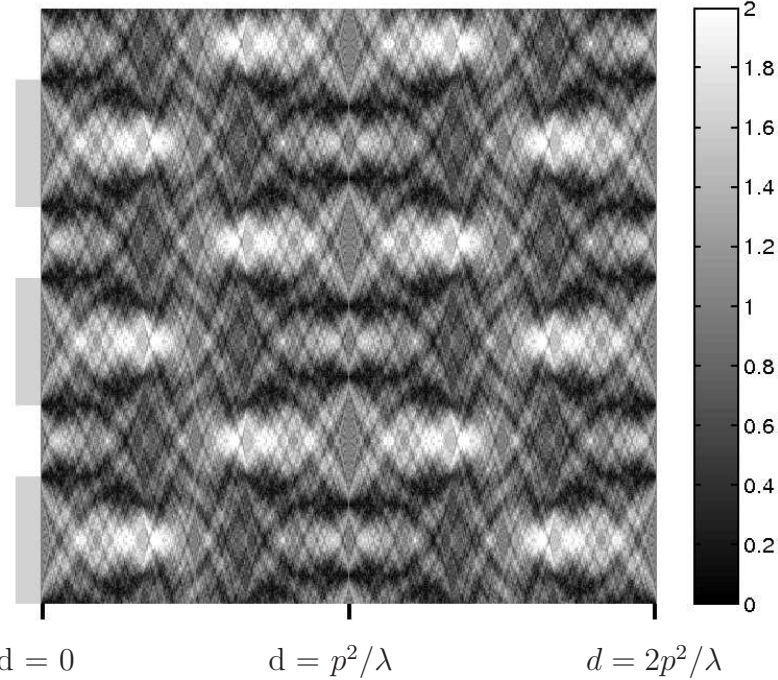


Figure 2.5. Intensity pattern of a wave travelling from left to right. After passing through the phase grating at the left edge of the figure with 0.3 duty cycle and π phase shift, an intensity pattern arise. Note the revival of the wavefront at half the Talbot distance $d = p^2/\lambda$ and at the full Talbot distance $d_T = 2p^2/\lambda$.

measure refraction angles. Both in the theoretical case of a plane wave X-ray source, and in the actual case of a curved wave-front.

2.3.1 Plane wave

Figure 2.6 show the intensity pattern after an ideal phase grating. The phase grating has a duty cycle of 0.5, *i.e.* half of the grating introduces a phase shift and half of the grating does nothing. The grating depth is matched to the wavelength of the incoming monochromatic wave such that the shift is exactly half a wavelength, corresponding to π phase shift. The simulated intensity pattern in figure 2.6 reveals binary intensity modulations at distances $d = mp^2/8\lambda$, where m is an odd integer. Note that the intensity modulations have half the period of the phase grating. This is the type of grating used for the experiments described later in this thesis.

With this kind of phase grating, our aim is to measure the exact transverse position of the intensity pattern. To get a feeling with the physical sizes of

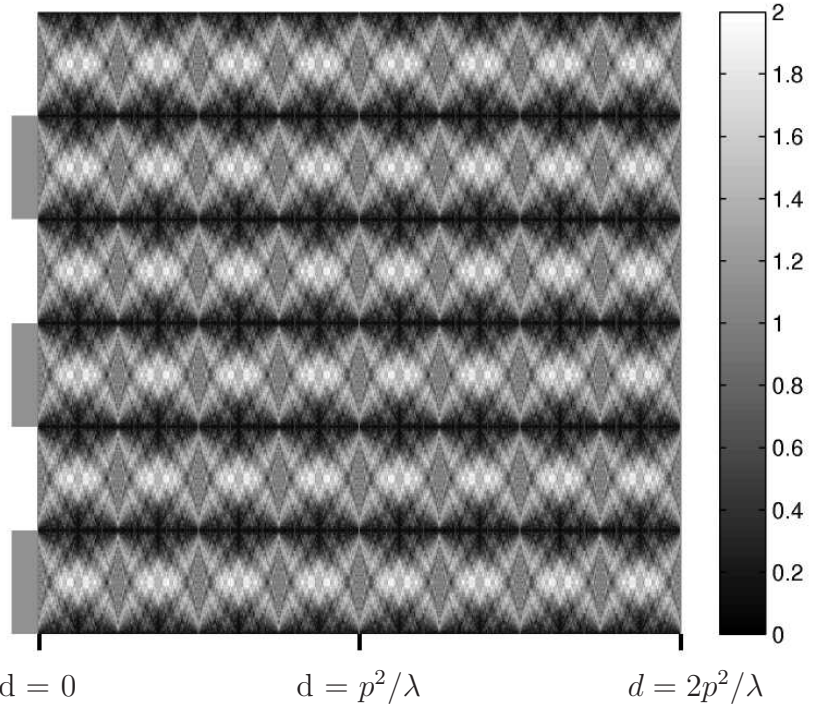


Figure 2.6. Intensity pattern after a phase grating with 0.5 duty cycle and π phase shift. The wave travels from left to right. Note the revival of a binary intensity pattern at odd fractional Talbot distances $d = mp^2/8\lambda$.

distances and angles involved in the experiment, we need to introduce some numbers at this point. With an X-ray energy of 24.8 keV, the corresponding wavelength is $\lambda = 0.5 \text{ \AA}$. With a grating period of $4 \mu\text{m}$, this gives intensity modulations at the distance $d = p^2/8\lambda = 4 \text{ cm}$. As the intensity pattern will have half the period of the grating, we will see intensity fringes with $2 \mu\text{m}$ period.

As we want to measure the exact position of the intensity pattern, we need either a detector with very high resolution (pixel size less than one third of the interference pattern period), or we need to introduce a second grating to the interferometer.*

A sketch of an interferometer with two gratings is displayed in figure 2.7, where a non-absorbing object has introduced a phase shift to the wave-front. The refraction in the wedge shaped part of the object has caused a slight

*One may comment that a larger grating period would relax the demand for a high-resolution detector to measure the intensity pattern. However, this would also increase the distance from the grating to the pattern, which would again require a higher transverse coherence of the beam. More about this in section 2.4.

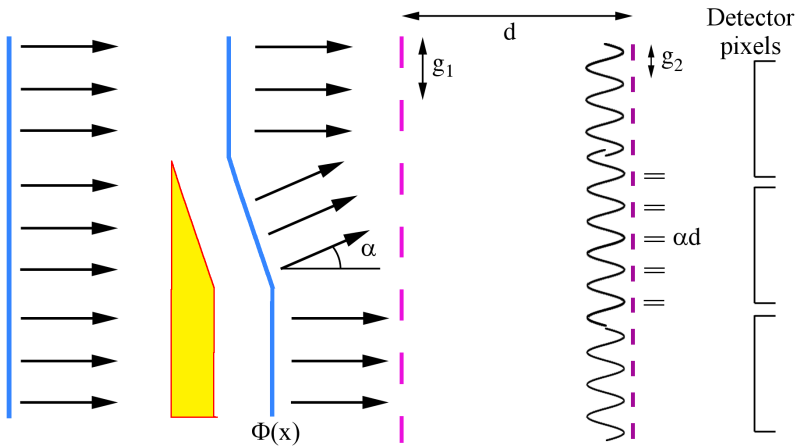


Figure 2.7. Transverse shift of interference pattern caused by beam refraction.

A plane wave coming from the left passes through a phase object, where a phase shift is introduced. The first grating, with period g_1 , produces an interference pattern at a distance d , where the second grating is located. The second grating is an absorption grating, with the same period as the interference pattern $g_2 = g_1/2$, that will transmit only part of the intensity. Behind the second grating is a detector with large pixels compared to the grating period.

deviation in the propagation direction of the local part of the wave-front. This angular deviation, α , results in a transverse shift of the interference pattern by the amount αd , where d is the distance between the gratings. The shift of the interference pattern is recorded by combining the detector with an absorbing grating, with same period as the interference pattern. If the first grating is a phase grating with π phase shift as illustrated in figure 2.6 with period $p = g_1$, then the second grating must be an absorption grating with period $g_2 = g_1/2$. The presence of the second grating ensures that the intensity recorded in the detector pixels will not be the same for the center pixel on figure 2.7 where refraction has occurred, as for the top-most pixel where no refraction has occurred. By recording a number of images with different transverse position of the second grating, the precise position of the interference pattern can be deduced.

Note that the intensity measured in the bottom-most pixel in figure 2.7 will be the same as the intensity recorded in the top-most pixel, though the phase shift is not the same. We will only see a transverse shift of the interference pattern when the *differential phase shift* is non-zero. If the phase of a plane wave at a given moment in a given plane is $\Phi(x)$, then the angular

deviation is given by

$$\alpha(x) = \tan\left(\frac{\lambda}{2\pi}\frac{\partial\Phi(x)}{\partial x}\right) \quad (2.27)$$

$$\approx \frac{\lambda}{2\pi}\frac{\partial\Phi(x)}{\partial x}, \quad (2.28)$$

introducing a transverse shift, $S(x)$, of the interference pattern of

$$S(x) = \frac{\lambda}{2\pi}\frac{\partial\Phi(x)}{\partial x}d. \quad (2.29)$$

If the total shift in a given pixel is equal to the period of the second grating, we are unable to distinguish the shifted pattern from a non-shifted pattern, and the detector signal is said to be phase wrapped. If we assume the signal to be small enough that no phase wrapping occurs (or at least no multiple phase wrapping), we can estimate the angular range of the interferometer to be of the order g_2/d . With the numbers given above, $g_2 = 2 \mu\text{m}$ and $d = 4 \text{ cm}$, the angular range is $50 \mu\text{rad}$. At these small angles, the approximation in equation 2.28 is valid.

To calculate the position of the interference fringes, a minimum of three images are needed with equidistant transverse shift of the G_2 grating between each image. If we denote the transverse shift of G_2 by x_g , the four grating positions of a four step scan would be $x_g = 0$, $x_g = g_2/4$, $x_g = g_2/2$ and $x_g = 3g_2/4$, as illustrated in the left column of figure 2.8. At $x_g = 0$, the fringes with positive interference are transmitted through the G_2 grating and a high intensity is measured in the detector. As the G_2 grating is shifted, less intensity is transmitted, until $x_g = g_2/2$ where all intensity is absorbed in the grating and nothing is measured in the detector.

The right row of figure 2.8 display four images recorded at the four different transverse positions of the second grating illustrated in the left column of the figure. The background intensity at $x_g = 0$ is high, as the position of the second grating is such that the full intensity is transmitted. At $x_g = g_2/2$ the grating has been shifted half a period, such that the interference lines with high intensity are exactly absorbed, and no intensity is transmitted leaving a dark background. At $x_g = g_2/4$ and $x_g = 3g_2/4$, half of the intensity is absorbed, leaving a grey background. Note that at $x_g = g_2/4$ the objects have a bright left edge and a dark right edge. At $x_g = 3g_2/4$ this has changed; the left edge is now dark and the right edge is bright. This illustrates the differential nature of the signal.

The procedure of how to process the recorded images in order to get the phase contrast and dark-field images we are looking for, is described in chapter 3.

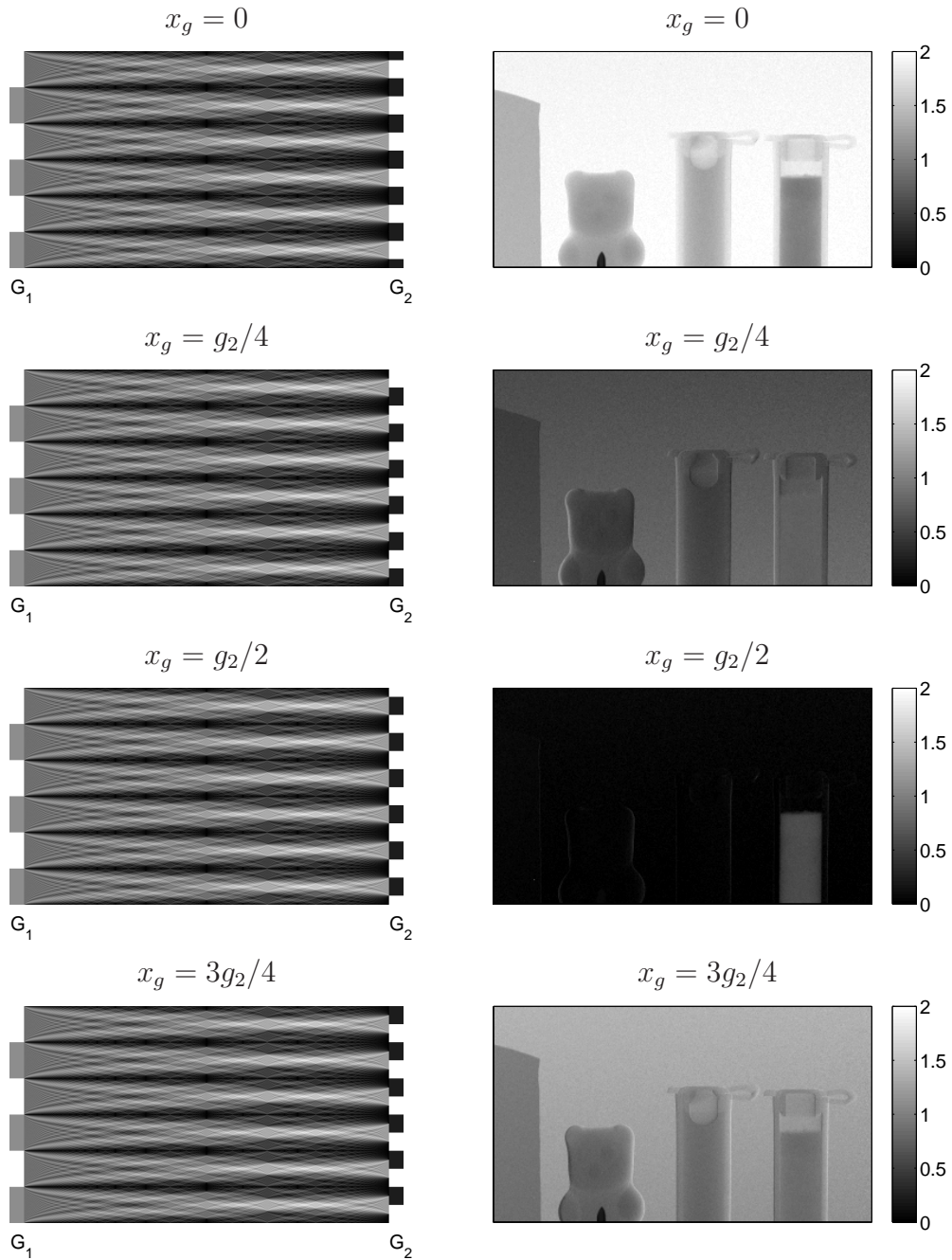


Figure 2.8. *Left column: Positions of grating g_2 during a four step phase stepping scan. Right column: Images of a test sample at corresponding transverse positions of the gratings.*

2.3.2 Magnification in curved wave setup

So far, we have assumed that the incoming wave is a perfect plane wave, which is off course never the case in real life. If we consider the source to be point like, the finite distance between the gratings introduces a magnification factor $M = (L+d)/L$, where L is the distance from the source to G_1 and d is the distance from G_1 to G_2 . In X-ray laboratories where the interferometer is located a few meters from the source, the magnification is significant. Even at synchrotrons where the interferometer can be located more than 100 meters from the X-ray source, the magnification is still not negligible. In effect, the period of the interference fringes is not exactly $g_1/2$, but rather $Mg_1/2$. This problem is easily solved by producing gratings with periods made to compensate for the magnification. If the magnification is not accounted for in the grating production, the mismatch between the fringe period and the g_2 grating period will result in Moire fringes on the detector, disturbing the signal. A magnification factor of $M = 1.01$ will produce a Moire fringe per 100 grating lines, and with a grating period of $2 \mu\text{m}$ we end up with five Moire fringes per millimeter. The magnification of the interference pattern is thus not negligible.

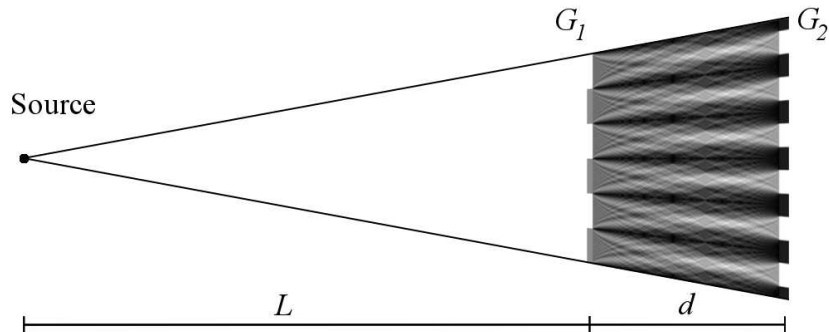


Figure 2.9. Geometric magnification of interference pattern.

One could argue that the gratings should be made to curve, to fit the curvature of the wave-front. In cases where the distance L to the source is much larger than the inter grating distance d the effect of curvature is however so small that it can be safely ignored. In figure 2.9, the intensity patterns in a grating interferometer, where the magnification has been accounted for, is simulated. The period of G_2 is not exactly half the period of G_1 , and equally important: the fractional Talbot distance defining the grating to grating distance is not exactly $g_1^2/8\lambda$. Due to the magnification, the fractional Talbot distance is now increased by the magnification factor M . If we define

the fractional Talbot distances in a parallel beam setup to be

$$a = m \frac{g_1^2}{8\lambda} \quad (2.30)$$

then the fractional Talbot distance in a magnifying setup is rescaled to

$$d = m \frac{g_1^2}{8\lambda} \frac{L + d}{L} \quad (2.31)$$

which can be rearranged to read

$$d = a \frac{L}{L - a}. \quad (2.32)$$

The consequence of a magnification factor is that the geometry of the setup must be taken into account in the grating design, and hence the same two gratings can not necessarily be used at both an X-ray tube with short setup geometry and at a synchrotron beamline with a long setup geometry.

2.3.3 Working with incoherent sources

For the interferometer to work at all, a certain amount of transverse beam coherence is needed. As the interferometer rely on the Talbot effect, which is an interference effect, the wave-front must have a large enough transverse coherence length for the wave revival to occur. However, as the gratings are only periodic in one direction, we only require coherence in this direction. There is no requirements to the coherence in the direction along the grating lines.

A simple approach to the problem of transverse coherence is to consider the source as a large number of thin line sources located side by side. One such line source will introduce an interference pattern at the distance d from G_1 . The next line source which is located a distance ϵ from the first line, will introduce an interference pattern which is shifted a distance $\epsilon d/L$ from the first interference pattern. If $\epsilon d/L \ll g_2$, the two interference patterns will overlap to increase the signal, but if $\epsilon d/L = g_2/2$, the two interference patterns will cancel out each other and diminish the signal. From these arguments, we can conclude that the width of the source should be no larger than

$$s = \frac{g_2 L}{2d} \quad (2.33)$$

as the contribution from each side of the source would then start to cancel out. Some typical numbers of an X-ray tube setup could be $g_2 = 2 \mu\text{m}$,

$L = 2 \text{ m}$ and $d = 4 \text{ cm}$, and we then need the source slit to be a maximum of $s = 50 \mu\text{m}$ wide. At a synchrotron the numbers could be $g_2 = 2 \mu\text{m}$, $L = 40 \text{ m}$ and $d = 4 \text{ cm}$, resulting in a source size requirement of $s = 1 \text{ mm}$. At the synchrotron the native source size is small enough to meet the requirement, but at a standard X-ray tube the requirement is not met. One solution is to use a thin slit or a micro-focus X-ray source, with a significant loss of beam intensity as a result. Another solution is to introduce a grating G_0 at the source, acting as an array of slits. The period g_0 of this grating should be

$$g_0 = g_2 \frac{L}{d}, \quad (2.34)$$

such that the interference pattern from neighboring source slits will overlap, increasing the total signal intensity.

2.3.4 The gratings

Our setup now consists of three gratings: a source grating G_0 with a period matched to the distances L and d , a phase grating G_1 with a period matched to L and d and a depth matched to the X-ray energy to give a phase shift of π , and finally an absorption grating G_2 with a period equal to half the magnified size of g_1 .

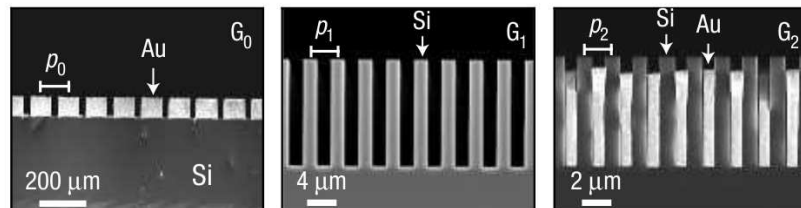


Figure 2.10. Scanning electron micrographs of G_0 , G_1 and G_2 gratings. This figure is adapted from (Pfeiffer et al. 2006).

The gratings used for the experiments presented in this thesis, are all produced by the *Laboratory for Micro- and Nanotechnology* (LMN) at the Paul Scherrer Institute in Switzerland. Grating G_1 is a pure Si grating, whereas gratings G_0 and G_2 are Si/Au absorption gratings made by etching into a Si-wafer and subsequent electro-plating of Au. A detailed description of the grating fabrication procedure is given by David et al. (2007a). Figure 2.10 show scanning electron micrographs of three gratings made at the LMN.

The height of the structures in each grating is made to fulfil the requirements that the gold structure is high enough to absorb close to 100% of the

beam, and the silicon structure of G_1 induces a phase shift of exactly π at the design energy. The phase shift is given by

$$\Delta\phi = \delta kh \quad (2.35)$$

where δ is the real part of the refractive index $n = 1 - \delta + i\beta$, k is the wavenumber $k = 2\pi/\lambda$, and h is the grating structure height. To get a phase shift of π , we need a structure height

$$h = \frac{\pi}{\delta k} \quad (2.36)$$

$$= \frac{\pi}{\lambda \rho r_0} \quad (2.37)$$

$$= 1.28[\mu\text{m}/\text{keV}] \times E[\text{keV}] \quad (2.38)$$

where $r_0 = 2.82 \times 10^{-5}\text{\AA}$ is the Thomson scattering length and ρ is the electron density. The electron density for silicon ($\rho_{Si} = 0.70\text{\AA}^{-3}$) has been inserted to get the last two equations where the photon energy E in keV gives a grating height in microns. *I.e.* with an X-ray energy of 28 keV, the height of grating G_1 must be 36 μm to produce a π phase shift.

2.4 Visibility

As previously described, transverse beam coherence is of vital importance to the grating interferometer. The transverse coherence length is given by (Fowles 1975)

$$l_t = \lambda \frac{r}{s} \quad (2.39)$$

where s is the source size r is the distance to the source and λ is the wavelength. For any interference phenomenon to occur, at certain amount of spatial beam coherence is needed. If the source size is too large, the coherence is reduced and it may be necessary to decrease the source size by introducing a source grating G_0 to 'slice' the actual source into an array of thin line-sources. In any case, whether the source itself is small or it is large and need to be sliced, there will be an effective source size which will determine the transverse coherence length.

In this section the visibility pattern produced from a source of finite size will be estimated.

2.4.1 Shape of interference pattern

In the case of a distant point-like monochromatic X-ray source, the wave front at the interferometer is plane and the interference pattern produced at

the fractional Talbot distance is a periodic top-hat as illustrated in figure 2.11.

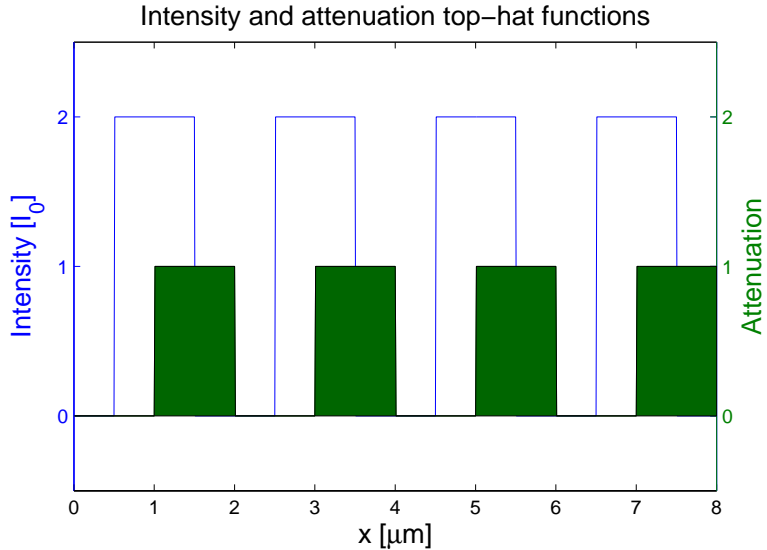


Figure 2.11. Top-hat functions. Blue line: Intensity of interference pattern at the fractional Talbot distance. Solid green: Attenuation of the analyzer grating G_2 . The grating has been shifted $0.5 \mu\text{m}$ in the x -direction with respect to the interference pattern.

During the phase stepping, where the analyzer grating G_2 is scanned over one grating period g_2 , the intensity recorded is the convolution of the two top-hat functions (as illustrated in figures 2.8 and 2.11). The recorded intensity as a function of grating position x is thus triangular and periodic with the period g_2 (see figure 2.12).

The periodic triangular function $f(x)$ can be constructed as an infinite sum of single triangular functions $f'(x)$ with unit area centered on $x = p'$

$$f'(x, p') = \begin{cases} \frac{2I_0}{p} \left(1 - \frac{|x|}{p/2}\right) & \text{if } |x - p'| \leq p/2 \\ 0 & \text{if } |x - p'| > p/2 \end{cases}$$

where the width p of the triangle is equal to the grating period g_2 . The periodic intensity pattern is then

$$f(x) = \sum_{p'=np} f'(x, p') \quad (2.40)$$

where $n \in \mathbb{Z}$.

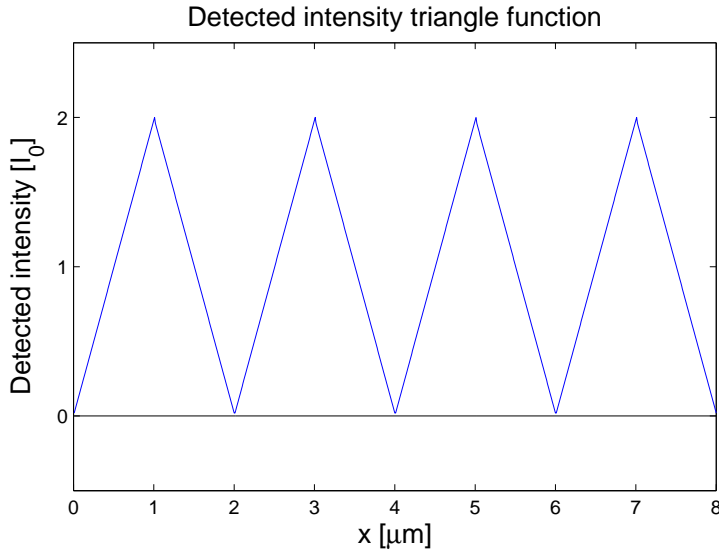


Figure 2.12. Triangle function. The recorded intensity I as a function of grating translation x is a triangular function.

Now consider a finite source size. Let us assume that the source has a Gaussian shape $g(x)$ with the root mean square width s :

$$g(x) = \frac{1}{s\sqrt{2\pi}} \exp\left(\frac{-x^2}{2s^2}\right). \quad (2.41)$$

If the distance from the source to G_1 is L and the distance from G_1 to G_2 is d , the size of the source projected onto G_2 is demagnified by a factor d/L , and the smearing due to the source size will then be

$$h(x) = \frac{1}{w\sqrt{2\pi}} \exp\left(\frac{-x^2}{2w^2}\right), \quad (2.42)$$

where $w = sd/L$ is the demagnified source size. The recorded intensity $I(x)$ will then be a convolution of the triangular shape produced by a point-like source with the Gaussian shape of the demagnified source*.

$$I(x) = f(x) \otimes h(x) \quad (2.43)$$

*As the triangular function is itself a convolution between two top-hat functions, the intensity $I(x)$ in equation 2.43 is really a convolution of three functions. The convolution operator is associative, and we may perform the two convolutions in arbitrary order — or at once in Fourier space.

To perform this convolution, first consider the Fourier transforms \tilde{f} and \tilde{h} of f and h , respectively*.

$$\tilde{f}(q) = I_0 \sum_n \text{sinc}^2\left(\frac{p}{2}q\right) e^{-2\pi ipqn} \quad (2.44)$$

$$= I_0 \text{sinc}^2\left(\frac{p}{2}q\right) \sum_m \delta\left(q - \frac{m}{p}\right) \quad (2.45)$$

where the *sinc* function is defined as $\text{sinc}(q) = \sin(\pi q)/(\pi q)$.

The Fourier transform of the Gaussian function $h(x)$ is

$$\tilde{h}(q) = e^{-\pi^2 2w^2 q^2},$$

giving the product

$$\tilde{f}(q)\tilde{h}(q) = I_0 \text{sinc}^2\left(\frac{p}{2}q\right) \sum_m \delta\left(q - \frac{m}{p}\right) e^{-\pi^2 2w^2 q^2} \quad (2.46)$$

and the convolution

$$\begin{aligned} I(x) &= f(x) \otimes h(x) \\ &= \int \tilde{f}(q)\tilde{h}(q) e^{2\pi iqx} dq \end{aligned} \quad (2.47)$$

$$= I_0 \sum_{m=-\infty}^{\infty} \text{sinc}^2\left(\frac{m}{2}\right) e^{-\pi^2 2(w/p)^2 m^2} e^{2\pi ixm/p}. \quad (2.48)$$

The last exponential term of equation 2.48 is transformed into a cosine function by redefining the sum over m , and the *sinc* function is evaluated as

$$\text{sinc}(m/2) = \frac{\sin(\pi m/2)}{\pi m/2} = \begin{cases} 1 & \text{if } m = 0 \\ 0 & \text{if } m \text{ even } \neq 0 \\ 2/(m\pi) & \text{if } m \text{ odd} \end{cases}$$

such that

$$\frac{I(x)}{I_0} = 1 + \sum_{m=1}^{\infty} \text{sinc}^2\left(\frac{m}{2}\right) e^{-\pi^2 2(w/p)^2 m^2} 2 \cos\left(\frac{2\pi x}{p}m\right) \quad (2.49)$$

$$= 1 + \sum_{m \text{ odd}} \left(\frac{2}{m\pi}\right)^2 e^{-\pi^2 2(w/p)^2 m^2} 2 \cos\left(\frac{2\pi x}{p}m\right) \quad (2.50)$$

$$= 1 + \sum_{n=1}^{\infty} \frac{8}{(2n-1)^2 \pi^2} e^{-\pi^2 2(w/p)^2 (2n-1)^2} \cos\left(\frac{2\pi x}{p}(2n-1)\right) \quad (2.51)$$

*The Fourier transform of a top-hat is the sinc function. As the triangular function is a convolution of two top-hat functions, it follows directly that the Fourier transform of the triangle is sinc².

where the sum over all positive odd integers m has been substituted by a sum over all positive (even and odd) integers n .

From equation 2.51 we see that the average intensity during a phase stepping scan is the intensity of the direct beam I_0 as expected, and the intensity modulation is given as a sum of cosines. The first few terms of the sum are

$$\begin{aligned} \frac{I(x)}{I_0} = & 1 + \frac{8}{\pi^2} e^{-\pi^2 2(w/p)^2} \cos\left(\frac{2\pi}{p}x\right) \\ & + \frac{8}{9\pi^2} e^{-\pi^2 18(w/p)^2} \cos\left(\frac{2\pi}{p}3x\right) \\ & + \frac{8}{25\pi^2} e^{-\pi^2 50(w/p)^2} \cos\left(\frac{2\pi}{p}5x\right) \\ & + \dots \end{aligned} \quad (2.52)$$

and we see that the higher order terms decay very fast. In the case of a point-like source size, *i.e.* $w = 0$, the higher order terms decay as $1/m^2$. At non-zero source size, the higher order terms decay as e^{-m^2}/m^2 . The visibility defined as $V = (I_{max} - I_{min})/(I_{max} + I_{min})$ is then

$$\begin{aligned} V(w/p) &= \frac{I(x=0) - I(x=p/2)}{I(x=0) + I(x=p/2)} \\ &= \sum_{m \text{ odd}} \frac{8}{m^2 \pi^2} e^{-\pi^2 2(w/p)^2 m^2} \\ &= \frac{8}{\pi^2} e^{-\pi^2 2(w/p)^2} \sum_{n=1}^{\infty} \frac{1}{(2n-1)^2} e^{-\pi^2 2(w/p)^2 (4n^2 - 4n)} \end{aligned} \quad (2.53)$$

and is plotted in figure 2.13.

From equation 2.53 and from figure 2.13 it is evident that the visibility decays as $\exp(-\pi^2 2(w/p)^2)$ at large values of w/p , but for small values of w/p the visibility decays linearly. The exact expression in equation 2.53 can be approximated by

$$V(w/p) = \begin{cases} 1 + \alpha \frac{w}{p} & \text{if } \frac{w}{p} \leq \frac{1}{2\pi} \\ \frac{8}{\pi^2} \exp(-2\pi^2 (\frac{w}{p})^2) & \text{if } \frac{w}{p} > \frac{1}{2\pi} \end{cases} \quad (2.54)$$

where the value $\alpha = 2\pi(8/(\pi^2 e^{1/2}) - 1) \approx -3.19$ is chosen such that the function is continuous in $w/p = 1/(2\pi)$.

The higher order terms are only significant when $w/p \leq 1/(2\pi)$. At source sizes larger than this, the contribution from higher order terms is less than

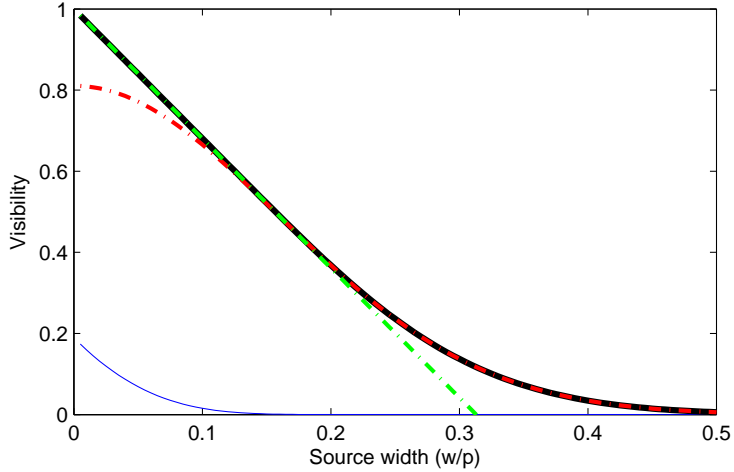


Figure 2.13. Visibility as a function of demagnified source size of a Gaussian shaped X-ray source. Black solid line: Visibility as calculated in equation 2.53. Red dash-dotted line: First order term, $(8/\pi^2) \exp(-\pi^2 2(w/p)^2)$. Blue solid line: Higher order terms. Green dash-dotted line: Linear approximation for small (w/p) values.

0.1 % and can be safely ignored. The calculated visibility at large source sizes ($w/p > 1/(2\pi)$) is consistent with the result published by Weitkamp et al. (2006) besides from the constant $8/\pi^2$.

2.4.2 Sampling rate

From figure 2.13 it is evident that higher order terms are significant at small source sizes, and hence need to be taken into consideration when analyzing the data.

To decouple the first order term in equation 2.52 from higher orders, a sufficient amount of steps (Momose et al. 2006) is needed from the phase stepping procedure described in section 2.3 above. From a mathematical point of view, one should always perform an odd number of steps; no additional information is gained by adding an extra point as all higher orders are odd. The lowest number of phase steps to possibly determine the first harmonic is three, and this is good enough at large source sizes *i.e.* when the measured visibility is below 50%. If however, the visibility is better than this, five, seven, nine or more phase steps are needed in turn as the third, fifth, seventh or higher harmonic becomes significant.

If too few phase steps are recorded, *e.g.* if three steps are recorded where five are needed, the amplitude and phase of the first harmonic as calculated

from the three phase steps measured will deviate from true values, as they are coupled to the amplitude and phase of the third harmonic.

If a sufficient amount of phase steps are measured, the important parameters for image production are:

- Amplitude of the zeroth order term (average value)
- Phase of the first order term (shift of pattern)
- Amplitude of first and higher order terms (visibility)

as will be explained below. Note that the phase of higher order terms are equal to the phase of the first order term under the given conditions.

All this said in a mathematical approach to interference visibility, it should be noted here that conclusions should not be taken too literally. When performing experiments in the laboratory, ideal condition in the mathematical sense are seldom available and as a consequence the measured visibility will be affected by factors not taken into consideration above. In particular grating imperfections, such as variations in the grating height or thickness causing the phase shift of G_1 to be different from π , thus introduce a non-perfect interference pattern at the fractional Talbot distances.

The condition of a monochromatic beam is fulfilled at synchrotron sources with a monochromator and at the Compact Light Source, and the conditions for the calculated visibility are valid.

At the X-ray tube with a large source size, a source grating G_0 is introduced to improve the transverse beam coherence in order to produce interference patterns. In this case the source shape is square, not Gaussian, and the above calculations are invalid. The interference pattern should then be calculated by convoluting the triangular shape in figure 2.12 with the top-hat shape of the source. The condition of a monochromatic beam is also invalid, and the broad spectral width of the X-ray tube will degrade the visibility and produce a cosine shaped interference pattern where higher order terms are negligible. At spectral widths of the order $\Delta\lambda/\lambda \approx 1/m$ or broader, where m is the fractional Talbot distance, the visibility will be significantly reduced Weitkamp et al. (2005). In this case, the measured intensity modulation is a linear combination of wavelengths producing interference patterns with high visibility, and wavelengths where the visibility is zero. However, the interference pattern will not be washed out completely by the broad spectrum. A narrow spectral width of $\Delta\lambda/\lambda \ll 1/m$ will have little effect on the visibility. The effect of a broad spectral width on the interference pattern is described in detail by Engelhardt et al. (2008).

In a strict mathematical description, it makes sense only to measure an odd number of phase steps. However, in the real experiment it does make

sense to measure an even number of points to improve statistics and thus obtain more precise measures of phase shift and visibility with reduced noise.

Chapter 3

Data analysis

The purpose of the grating interferometer is to create an interference pattern that changes its shape due to the interaction between X-ray and sample. Our aim is now to use the images recorded during the phase stepping scan of grating G_2 (illustrated in figure 2.8), to reconstruct the interference pattern. By comparing the interference pattern with the sample in place to the interference pattern of the empty beam, we can calculate the refraction angles introduced by the sample.

Subsequently we can use the processed images for three dimensional tomographic reconstruction. The basic mathematics behind the filtered back-projection algorithm commonly used for fast reconstruction is reviewed here, and the necessary modifications to use the reconstruction algorithm with differential phase data is derived. As no quantitative description of dark-field images has previously been published, a theory for the dark-field signal is given, introducing a linear diffusion coefficient ϵ which can be used for tomographic purposes.

3.1 Image processing

From the mathematical analysis in section 2.4, we know that the intensity of the interference pattern can be written as (equation 2.52)

$$I_{p_x, p_y}(x_g) = a_0(p_x, p_y) + \sum_{m=1}^{\infty} a_m(p_x, p_y) \cos\left(\frac{2\pi m x_g}{g_2} + \phi_m(p_x, p_y)\right). \quad (3.1)$$

Instead of fitting the obtained intensity curves $I_{p_x, p_y}(x_g)$ to one or more cosine functions, the same information can be obtained as the components of the Fourier transform. We can consider equation 3.1 as a Fourier series, and extract the parameters through Fourier analysis. The time required to

calculate the a_m and ϕ_m parameters from a discrete set of I values can be greatly reduced by using a *Fast Fourier Transform* (FFT) algorithm developed and optimized for discrete Fourier analysis, rather than least square fit to cosine functions.

To make the principles of the grating interferometer clear, the data presented in chapter 2 are simulated data, as they would look if produced by a fully coherent parallel beam illuminating a set of perfect gratings. In practice however, there will be imperfections in the gratings, the illumination will not be perfectly flat, and the finite beam coherence will reduce visibility. In order to determine the absorption, refraction and scattering is caused by the object, it is necessary to include in the image processing a set of reference images recorded with an empty beam. The reference images are recorded during a phase stepping scan as described above under conditions identical to those recorded of the sample.

The reference images are processed by Fourier analysis in the same way as the images of the sample, and we get a set of parameters a_0 , a_m and ϕ_m for the reference images as we get for the sample. We will denote the parameters obtained from the reference beam with a superscript r and those from the sample with a superscript s . As the average value a_0^s corresponds to the intensity transmitted through the sample, we can define the relative absorption as $a_0 = a_0^s/a_0^r$. The transverse shift of the interference pattern is given by the phase of the first Fourier component ϕ_1 , and we can define the relative phase shift as $\phi_1 = \phi_1^s - \phi_1^r$. Finally, the visibility is given by sum of the higher order amplitudes a_m relative to the mean value a_0 as defined in equation 2.53, *i.e.* $V = \sum_m a_m/a_0$. Depending on shape of the recorded intensity pattern (depending on the source size, energy spectrum, grating quality, *etc.*) it may be necessary to include one or more higher order terms besides the first order term a_1 . We can thus define the relative absorption, phase shift and visibility as

$$a_0 \equiv \frac{a_0^s}{a_0^r} \quad (3.2)$$

$$\phi_1 \equiv \phi_1^s - \phi_1^r \quad (3.3)$$

$$V \equiv \frac{V^s}{V^r} = \frac{a_0^r}{a_0^s} \sum_{m \text{ odd}} \frac{a_m^s}{a_m^r}. \quad (3.4)$$

3.1.1 Three image signals

Figure 3.1 show four images recorded with an empty beam (left column) and the corresponding four images recorded with a sample in the beam. From

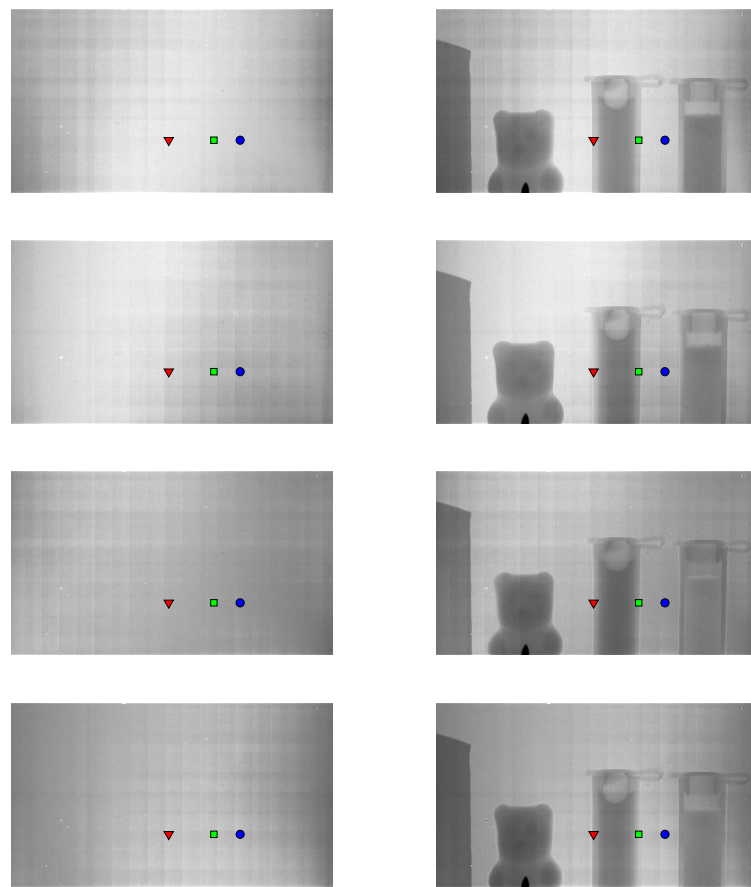


Figure 3.1. *Images recorded by the detector during a phase stepping scan. Left column shows images of the empty reference beam, and right column show images with the sample in place. The intensities in the three marked points are plotted in figure 3.2.*

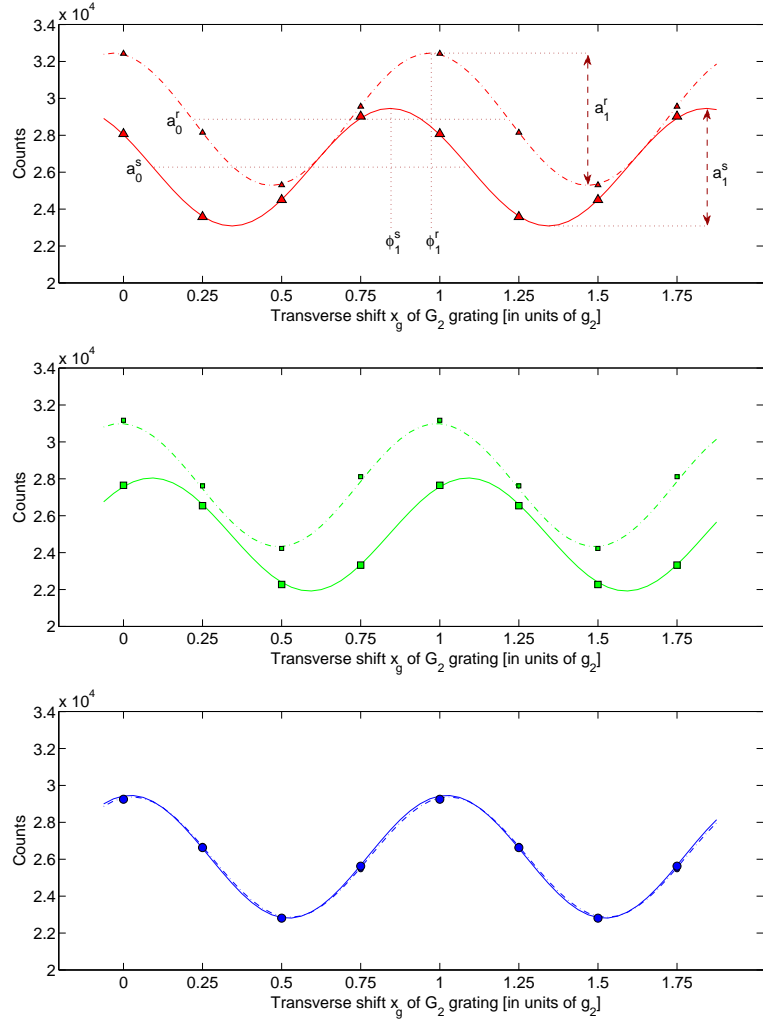


Figure 3.2. Intensity curves of the three pixels marked in figure 3.1. The measured intensities of reference beam are marked with small markers, measured intensities with sample in the beam have large markers. Blue circles indicate the intensity of the direct beam. Red triangles indicate the intensity at the left edge of a cylindrical object, and green squares indicate the intensity at the right edge. The data have been fitted with a cosine function, shown as dash-dot or solid lines. The average value a_0 , shift ϕ_1 and amplitude a_1 of the first order cosines are indicated in the figure.

the left, the four samples in the beam are a silicon wafer, a gummi bear, a plastic cylinder with water and a plastic cylinder with powdered sugar. For each pixel, an intensity curve $I(p_x, p_y, x_g)$ can be plotted, where (p_x, p_y) is the pixel coordinate and x_g is the transverse shift of G_2 . The intensity curves for the three pixels marked in figure 3.1 are plotted in figure 3.2. The first order cosine in equation 3.4 is

$$I_{p_x, p_y}(x_g) = a_0(p_x, p_y) + a_1(p_x, p_y) \cos\left(\frac{2\pi}{g_2}x_g + \phi_1(p_x, p_y)\right) \quad (3.5)$$

with is a good description of the data displayed in 3.2. The intensity curves thus yield the parameters a_0^r , a_1^r and ϕ_1^r for each pixel (p_x, p_y) in the reference image and a_0^s , a_1^s and ϕ_1^s for each pixel in the image of the sample. The cosine curves given by the fit parameters are also plotted in the figure.

The average value a_0 corresponds to the transmitted intensity one would measure on a standard X-ray image without the interferometer. Hence, we shall refer to the image obtained from a_0 as *the standard absorption image*. The transverse shift of the interference pattern is fitted by the parameter $\phi_1 \in]-\pi, \pi]$. The transverse shift in a given pixel is then

$$S(p_x, p_y) = \phi_1(p_x, p_y) \frac{g_2}{2\pi}, \quad (3.6)$$

corresponding to an angular refraction of

$$\alpha(p_x, p_y) = \frac{g_2}{2\pi} \frac{\phi_1(p_x, p_y)}{d}. \quad (3.7)$$

By use of equation 2.28, the differential phase shift of the wave-front after passing through the sample can be expressed as

$$\frac{\partial \Phi(p_x, p_y)}{\partial x} = \frac{2\pi}{\lambda} \alpha(p_x, p_y) = \frac{g_2}{\lambda} \frac{\phi_1(p_x, p_y)}{d}, \quad (3.8)$$

and the actual phase shift can be found by integration. When ϕ_1 is used directly to form an image, as in figures 3.3 and 3.4, we will refer to it as *the differential phase contrast image*.

Figure 3.3 displays an example of the interference pattern shift recorded of the reference beam and of a sample at a standard X-ray tube as described in chapter 4 below. The shift recorded across the detector area is non-uniform, but the relative shift introduced by the sample is extracted by subtracting the reference shift ϕ_1^r from ϕ_1^s . The resulting image has a nice flat background as no relative shift has occurred between the measurements of ϕ_1^r and ϕ_1^s .

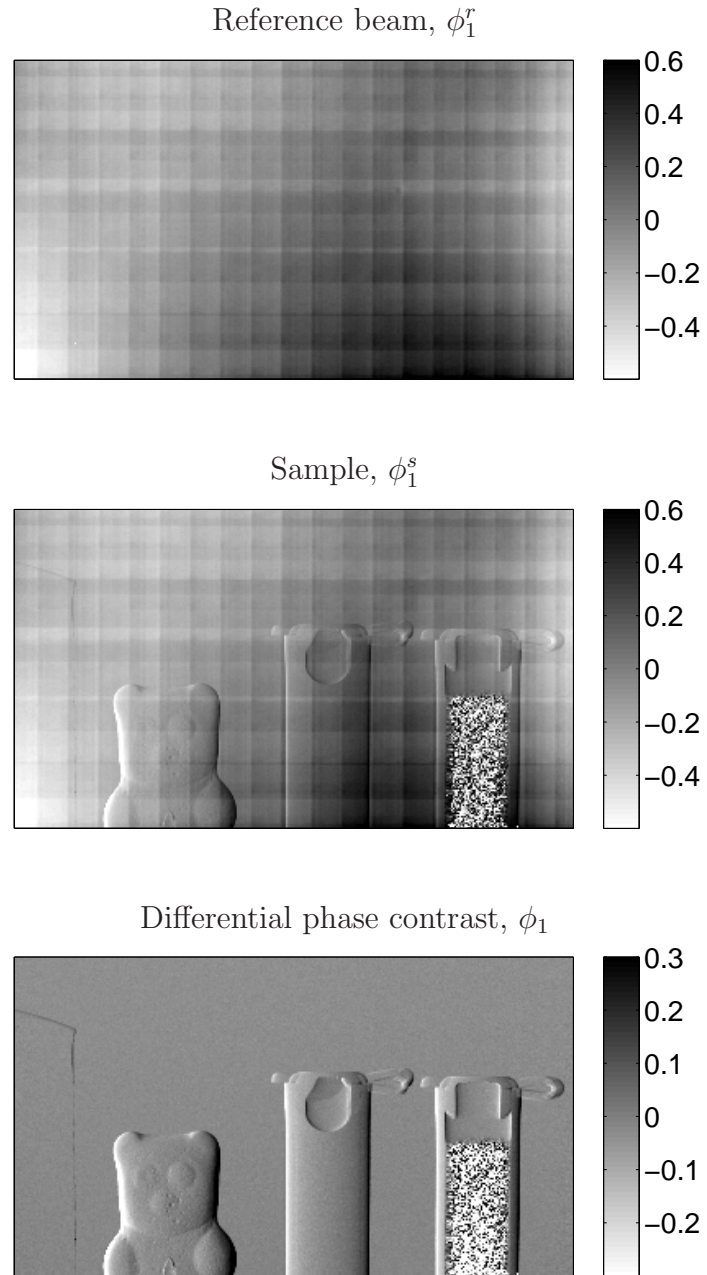


Figure 3.3. Recorded transverse shift of the intensity modulation ϕ_1 at X-ray tube. Left: Empty reference beam, ϕ_1^r . Center: Sample in beam, ϕ_1^s . Right: Differential phase image, $\phi_1 = \phi_1^s - \phi_1^r$.

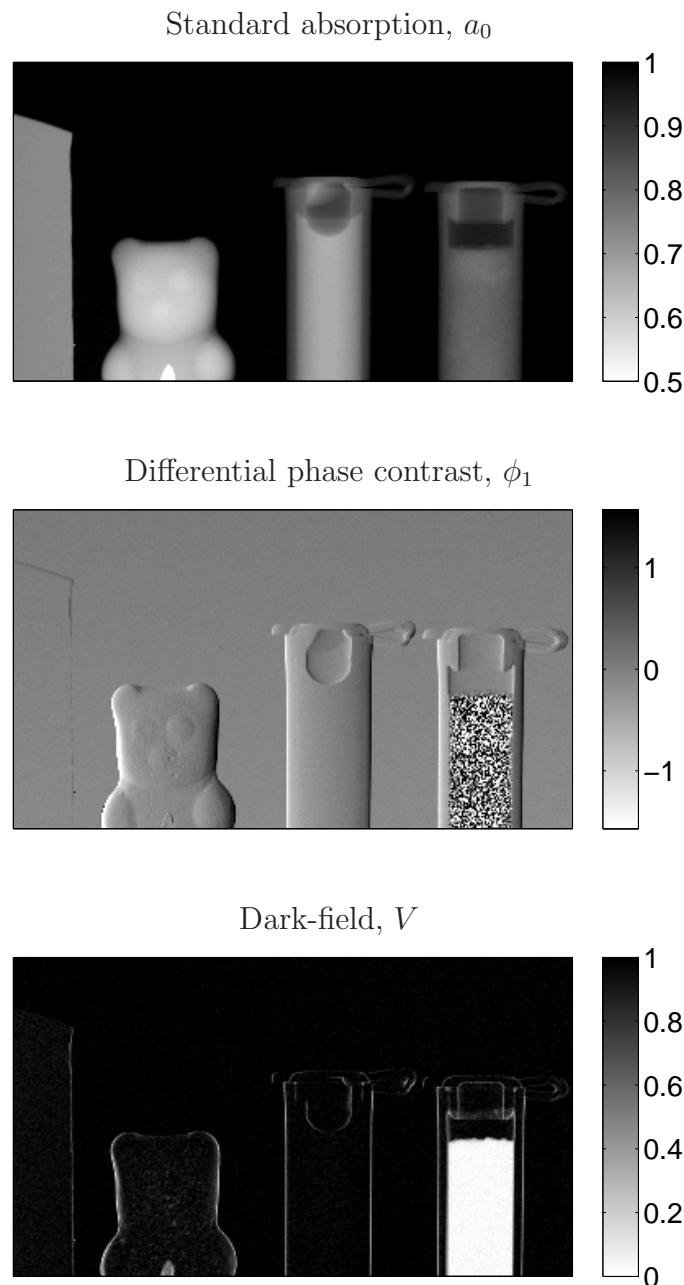


Figure 3.4. Images constructed from the three fitting parameters. Standard absorption image from a_0 , differential phase contrast from ϕ_1 and dark-field image from V . The single crystal silicon to the left is visible only in the absorption signal. The sugar sample to the right gives a strong dark-field signal due to scattering. The gummi bear and water sample in the center of the images act as refracting objects and are hence visible in the differential phase signal.

The fitting parameters a_m for $m \geq 1$ can also be used as an image signal. The visibility V^s is the amplitude of the intensity curve in equation 3.1. Incoherent scattering in the sample will reduce the beam coherence and consequently diminish the interference visibility, and $V = V^s/V^r$ can thus be considered as a measure of incoherent scattering. We will refer to this signal as *the dark-field image* due to the resemblance to dark-field imaging in visible light microscopy (Murphy 2001). The concept of dark-field imaging with a grating interferometer was first introduced in publication II (Pfeiffer et al. 2008a). As discussed above in section 2.4, we note that higher order terms from the Taylor series of cosines can be important at experimental setups where the interferometer is illuminated with a beam of high coherence. In many cases however, only the first order term is of significant magnitude, and higher order terms can be ignored. In particular at the experiments performed at the X-ray tube source described in this thesis, coherence is low and higher order Fourier terms are not taken into account.

In figure 3.4 the three image modalities, a_0 , ϕ_1 and V , are illustrated. The grey scale on panel (a) has been inverted such that pixels with high intensity are dark like the blackening of an old-fashioned X-ray sensitive film. The scale on panel (c) is inverted to look like a dark-field image in the visible light microscope where scattered light is focused in the image plane and the background is dark (hence the name). The contrast mechanism behind the dark-field image will be explained in section 3.1.2 below.

The difference between absorption a_0 , phase contrast ϕ_1 , and dark-field image V , is well illustrated by the different samples in figure 3.4. The silicon wafer to the left is a crystalline object with flat parallel surfaces. Such an object is absorbing, but introduces no scattering and no angular refraction, and as a consequence it is only visible in the standard absorption image (except for the edges). The gummi bear and plastic cylinder with water are both homogeneous objects with a curved surface, refracting the X-ray beam acting as a diverging lens. These two objects are visible both in the absorption image and in the differential phase contrast image, but the scattering is weak and they remain dark in the dark-field image. Finally, the cylinder with powdered sugar to the right, scatters strongly and therefore gives a strong dark-field signal. The texture of this sample greatly reduces the coherence of the X-ray beam, thus destroying the interference pattern. As there is no visibility, the phase signal becomes random and the pattern amplitude is zero.

3.1.2 Linear diffusion coefficient

For a quantitative description of the dark-field signal, it is necessary to introduce a material dependent *linear diffusion coefficient* analogue to the linear

absorption coefficient used in attenuation based imaging.

As the dark-field image contrast is a reduced visibility in the interference pattern at the analyzer grating, several different physical phenomena can contribute to this signal. In this section we shall consider the beam spread caused by small angle scattering and multiple refraction.

Consider a thin slice of thickness y_1 of material that does not absorb. The X-ray beam penetrates the thin slice and is scattered in an angular distribution as a result.

We assume that the angular probability distribution $A_1(\theta)$ of the scattered intensity is Gaussian:

$$A_1(\theta) = \frac{1}{\sigma_1 \sqrt{2\pi}} \exp\left(-\frac{\theta^2}{2\sigma_1^2}\right) \quad (3.9)$$

where σ_1 is the width (root mean square) of the Gaussian scattering distribution. If we stack several slices, the scattering distribution from the first slice will be further broadened by the second slice, and the resulting distribution will be further broadened by the third slice, and so forth.

In the general case, multiple scattering of some — but not all — photons may change the shape of the angular distribution, as the photons scattered in the first slice may or may not be scattered in the following slices. However, to keep the calculations simple, we shall assume that all slices affect the beam in similar way, namely by a Gaussian angular broadening.

After penetrating one slice of scattering material, the angular distribution will be that of equation 3.9, and after penetrating N slices, the angular distribution will be

$$A(\theta) = A_1(\theta) \otimes A_2(\theta) \otimes \dots \otimes A_N(\theta) \quad (3.10)$$

$$= \frac{1}{\sigma \sqrt{2\pi}} \exp\left(-\frac{\theta^2}{2\sigma^2}\right) \quad (3.11)$$

where \otimes is the convolution operator and the total scattering width σ is

$$\sigma = \sqrt{\sigma_1^2 + \sigma_2^2 + \dots + \sigma_N^2}. \quad (3.12)$$

The intensity recorded in the detector will then be a convolution

$$I^s(x) = I^r(x) \otimes A(x) \quad (3.13)$$

where the spatial smearing

$$A(x) = \frac{1}{\sigma d \sqrt{2\pi}} \exp\left(-\frac{x^2}{2\sigma^2 d^2}\right) \quad (3.14)$$

is the angular distribution propagated the distance d from the sample to the analyzer grating G_2 .

If the intensity modulation of the reference beam is well described by a cosine as in equation 3.5, we can perform the convolution to get the result:

$$\begin{aligned} I^s(x) &= \left\{ a_0^r + a_1^r \cos \left(\frac{2\pi}{p}x - \phi_1 \right) \right\} \otimes A(x) \\ &= a_0^r + a_1^r \exp \left(\frac{-2\pi^2}{p^2} \sigma^2 d^2 \right) \cos \left(\frac{2\pi}{p}x - \phi_1 \right), \end{aligned} \quad (3.15)$$

and we see that the visibility as given by equations 3.4 and 3.15 is

$$\begin{aligned} V &= \frac{V^s}{V^r} \\ &= \frac{a_1^s a_0^r}{a_1^r a_0^s} \\ &= \exp \left(\frac{-2\pi^2}{p^2} \sigma^2 d^2 \right). \end{aligned} \quad (3.16)$$

Scattering dependence on sample thickness

The width σ of the distribution function $A(\theta)$ is a function of the slice thickness y_1 and of the scattering width σ_n of each layer. We now introduce a *linear diffusion coefficient*, ϵ , expressed in terms of σ and thickness Δy as

$$\epsilon = \frac{\sigma^2}{\Delta y}, \quad (3.17)$$

that is a material dependent variable describing the specific scattering width per unit length. In general, the scattering width along a beam path can be found by integration:

$$\sigma^2 = \int \epsilon(y) dy, \quad (3.18)$$

and we get

$$V(x) = \exp \left(\frac{-2\pi^2 d^2}{p^2} \int \epsilon(x, y) dy \right) \quad (3.19)$$

as a final expression for the visibility.

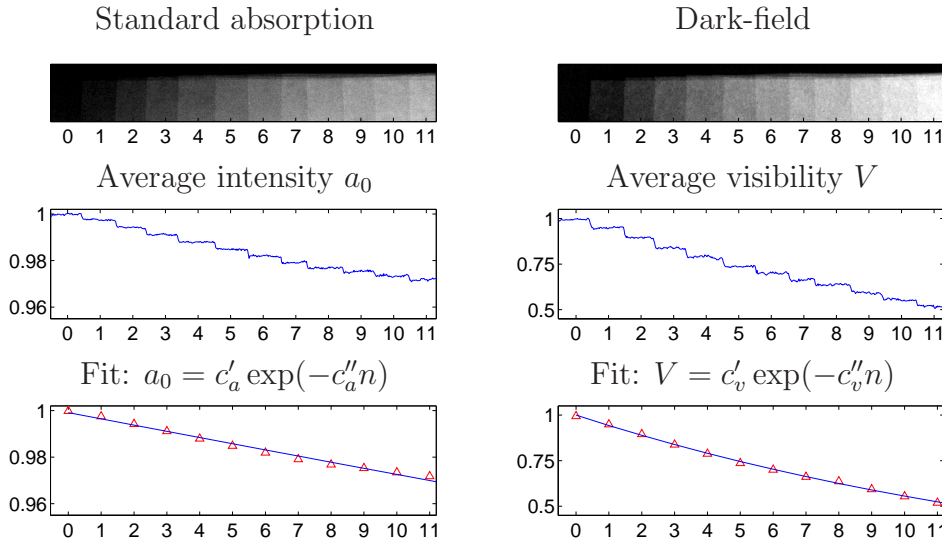


Figure 3.5. Standard absorption and dark-field images of paper stack, recorded at a standard X-ray tube. The distance between the gratings corresponds to the fifth fractional Talbot distance at 28 keV. For more experimental details see chapter 4. The stack thickness increases with the number of sheets $n = 0-11$. The transmission is only lowered by a few percent, whereas the visibility is reduced to 0.5 at 11 sheets. Intensity and visibility fit parameters are $c'_a = c'_v = 1$, $c''_a = 0.00270$ and $c''_v = 0.0588$. Note the different y-axes.

3.1.3 Dark-field images

To test the validity of equation 3.19, consider the experimental data presented in figure 3.5. A stack of paper sheets has been measured with the grating interferometer. The paper sheets are shifted such that the beam penetrates an increasing number of sheets.

From the visibility as a function of stack thickness, $V(n)$, we see that the decay of the visibility is in good agreement with the exponential fit. The fit to the average intensity as a function of stack thickness gives a small value to the exponent, reflected in an almost linear dependence. The exponential expression in equations 2.7 and 3.19 can be rearranged to give the integrated linear attenuation coefficient μ and the integrated linear diffusion coefficient ϵ

$$\int \mu(x, y) dy = -\ln a_0(x) \quad (3.20)$$

$$\int \epsilon(x, y) dy = \frac{-p^2}{2\pi^2 d^2} \ln V(x). \quad (3.21)$$

The exponential fit

$$a_0(n) = c'_a \exp(-c''_a n) \quad (3.22)$$

$$V(n) = c'_v \exp(-c''_v n) \quad (3.23)$$

shown in figure 3.5 give the fit parameters $c'_a = c'_v = 1.00$, $c''_a = 0.0027$ and $c''_v = 0.059$. From these parameters we can calculate the linear absorption coefficient μ_1 and the linear diffusion coefficient ϵ_1 for a single piece of paper. The expressions are

$$\mu_1 y_1 = c''_a \quad (3.24)$$

$$\epsilon_1 y_1 = \frac{p^2}{2\pi^2 d^2} c''_v \quad (3.25)$$

where $p = 2 \text{ } \mu\text{m}$ and $d = 20 \text{ cm}$, and we get the values

$$\mu_1 = \frac{2.7 \times 10^{-3}}{y_1} \quad (3.26)$$

$$\epsilon_1 = \frac{9.4 \times 10^{-13}}{y_1} \quad (3.27)$$

where y_1 is the thickness of one paper sheet.

To conclude the full validity of equation 3.19 based on this experimental result, is to jump to conclusions. We would need to measure a vast variety of samples with different SAXS profiles to see if the exponential expression is a good general description. Expectedly, there will be samples where the approximation of a Gaussian scattering distribution fail and where the above description of the dark-field signal is poor.

For the moment we will conclude that the expression in equation 3.19 is not bad for our purpose, and this expression is used as a basis for tomographic reconstructions of the dark-field signal.

3.2 Tomography

Implementation of computed tomographic reconstructions in X-ray scanners have lead to a revolution in medical diagnosis. Godfrey Hounsfield (Hounsfield 1973) and Allan McLeod Cormack (Cormack 1963) received the Nobel price in medicine in 1979 for the invention of the CT scanner. Later, the tomographic reconstruction has been improved by implementation of the Radon transform which was published in 1917 by Johann Radon. Tomography means to take X-ray images of a sample from different directions, and

then use the values of individual picture cells (pixels) to reconstruct the absorption of individual volume cells (voxels) inside the sample.

Though there are many practical considerations (such as element dependent absorption, different energy response leading to beam hardening and geometrical effects such as cone beam geometry) that in turn makes a precise quantitative reconstruction very difficult, the mathematical concept of reconstructing a density distribution from its projections is very simple. There are many textbooks describing the mathematics of tomography, one of them is the *Principles of Computerized Tomographic Imaging* by Kak & Slaney (2001). Some figures from this book are reproduced here to explain the basics of tomography, but the full book can be found online in a free version. The two-dimensional Radon transform takes a real two-dimensional function, $f(x, y)$, such as a density distribution, and transforms it into its angular projections, $\mathcal{P}_\theta(x')$, by integration:

$$\mathcal{P}_\theta(x') = \iint f(x, y) \delta(x \cos \theta + y \sin \theta - t) dx dy \quad (3.28)$$

where δ is the Dirac delta function, see figure 3.6. The inverse Radon transform is an exact mathematical transformation based on the *projection-slice theorem*, stating that the Fourier transform of the projection in equation 3.28 is equal to the slice tilted by an angle θ through the origin of the two-dimensional Fourier transform of $f(x, y)$. The validity of the Fourier slice theorem can easily be verified by calculating the Fourier coefficients along the line u' in figure 3.6 that is tilted by an angle θ . The values along this line $\tilde{f}(u', \theta)$, can be calculated as

$$\begin{aligned} \tilde{f}_\theta(u') &= \iint f(x', y') e^{-i2\pi(x', y') \cdot (u', v')} dx' dy' \\ &= \iint f(x', y') e^{-i2\pi(x' u')} dx' dy' \\ &= \iint f(x', y') dy' e^{-i2\pi(x' u')} dx' \\ &= \int \mathcal{P}_\theta(x') e^{-i2\pi(x' u')} dx' \end{aligned} \quad (3.29)$$

where a new rotated coordinate system (x', y') is introduced. In real space $(x', y') = (x \cos \theta + y \sin \theta, -x \sin \theta + y \cos \theta)$ and in reciprocal space $(u', v') = (u \cos \theta + v \sin \theta, -u \sin \theta + v \cos \theta)$. In the rotated frame the line has $v' = 0$, and we can perform the integration over y' separately from the Fourier transformation. This now corresponds to a one-dimensional Fourier transform of the projection $\mathcal{P}_\theta(x')$.

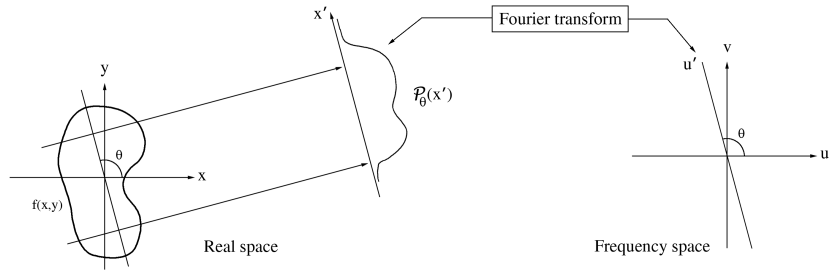


Figure 3.6. Projection of density distribution onto the line tilted by an angle θ , and illustration of the projection-slice theorem. The Fourier transform of a projection at the angle θ is equal to a slice at angle θ through the Fourier frequency space.

In the following, the application of the projection-slice theorem to tomography will be described, and the use for 3-D X-ray image reconstruction will be explained.

3.2.1 Tomographic reconstruction of absorption data

In the theoretical case of a continuous density function, the function can be fully calculated from its projections by the inverse Radon transform. However, in the physical experiment we only have a finite set of projection angles and a finite set of ray paths (detector pixels), and as a result we will only get a discrete representation of the Fourier transform in polar coordinates (see figure 3.7). To transform the set of discrete Fourier components in polar coordinates into a function in real space in cartesian coordinates, some kind of interpolation is needed. There are several ways to deal with the missing information lost in the discrete data set.

Interpolation from polar to cartesian coordinates in frequency space, followed by an inverse Fourier transformation is the most obvious way to do it. But this interpolation is cumbersome and slow for large data sets.

Algebraic Reconstruction Techniques (ART) exist, where iterative methods can be implemented to optimize the solution function $f(x,y)$ to the measured data. These methods work well in theory, but for large data sets they are very slow to work with due to the iterative procedure. For small data sets, or for data sets where some angles are missing or where the angular distribution of the projections is irregular, it may be necessary to use an iterative reconstruction algorithm. But in a data set recorded over 180 or 360 degrees, with regularly spaced projections, the reconstruction can be done with the filtered backprojection which is much faster.

The common way to describe the filtered backprojection approach, is that the projection data are *backprojected* by smearing each projection out over the entire field of view. To compensate for the fact that the pixels near the rotation axis are much closer sampled than those at the edge (see figure 3.7), the Fourier transform is normalized by a linear ramp filter.

The mathematical description of the filtered backprojection, is found by using polar coordinates in the inverse Fourier transform equation. The inverse Fourier transform

$$f(x, y) = \iint \tilde{f}(u, v) e^{i2\pi(ux+vy)} du dv, \quad (3.30)$$

is rewritten in polar coordinates as

$$f(x, y) = \int_0^\pi \int_{-\infty}^\infty \tilde{f}(r, \theta) e^{i2\pi(x \cos \theta + y \sin \theta)r} |r| dr d\theta, \quad (3.31)$$

where the polar coordinates r, θ are defined such that $(u, v) = (r \cos \theta, r \sin \theta)$, $r \in]-\infty, \infty[$, $\theta \in [0, \pi[$. *I.e.* there is a linear ramp $|r|$ introduced by the change of coordinates. The double integration in equation 3.31 can be split into two; the integration over r

$$\mathcal{G}(x' = x \cos \theta + y \sin \theta, \theta) = \int_{-\infty}^\infty \tilde{f}(r, \theta) e^{i2\pi x' r} |r| dr \quad (3.32)$$

which is referred to as filtering, and the θ integration

$$f(x, y) = \int_0^\pi \mathcal{G}(x \cos \theta + y \sin \theta, \theta) d\theta \quad (3.33)$$

which is referred to as backprojection.

To use equation 3.31 to reconstruct a tomographic slice from a discrete dataset, the computational steps are as follows:

1. Calculate the Fourier space slices from the projection data (equation 3.29).
2. Perform the filtering by calculating $\mathcal{G}(x', \theta)$ (equation 3.32).
3. Backproject filtered data (equation 3.33).

All three steps are computationally simple operations that are easily implemented in a computer. Fourier transforms of a discrete n -dimensional data set computed with a FFT algorithm, will produce an n -dimensional vector in frequency space. Data recorded with a detector n pixels wide at m different

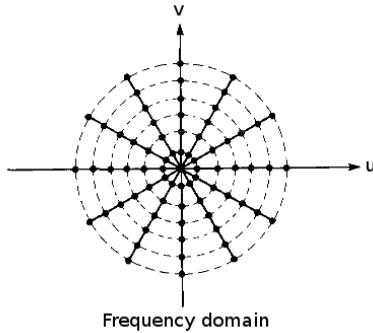


Figure 3.7. The discrete nature of the measured data leaves us with discrete representation of the Fourier transform. Due to rotational symmetry of the experiment, the sampling density in Fourier space is inverse proportional to frequency. Figure adapted from Kak & Slaney (2001).

angular projections, then comprise a $(n \times m)$ -dimensional data set — a so called sinogram. Step (1) is a one-dimensional Fourier transform along the n detector pixels, and step (2) is an inverse Fourier transform with a filter along the n detector pixels. These operation do not change the length of the data, and leaves a $(n \times m)$ -dimensional data set. But step (3) is a sum over θ for each pair of (x, y) in the $(n \times n)$ -dimensional slice we want to reconstruct, as a consequence the values of $x' = x \cos \theta + y \sin \theta$ do not necessarily exist in the data set, and an interpolation of the data is required.

There are a number of different ways to interpolate, such as *nearest neighbor*, *linear interpolation* or *cubic interpolation*. Further, the linear ramp filter, also known as *Ram-Lak filter*, in equation 3.31 may be modified by a different filter function, such as the *Shepp-Logan* (sinc function), a *cosine* filter, or the *Hamming* filter (raised cosine), to suppress high frequency noise. In the experimental section of this thesis, the tomographic reconstructions are made using filtered backprojection with a linear (Ram-Lak) filter and linear interpolation.

The greatest advantage for filtered backprojection is that it is fast. Implementation of a filtered backprojection algorithm on a modern computer makes the tomographic reconstruction in a matter of seconds, even for large data sets. A major disadvantage is that areas with high contrast in the sample may produce streak artifacts in the reconstruction due to the backprojection procedure.

The absorption coefficient

As stated in equation 2.4, the amplitude of a plane wave travelling in the x direction in a medium with index of refraction $n = 1 - \delta + i\beta$ is

$$|\Psi(\bar{r})| = E_0 e^{-\beta kx} \quad (3.34)$$

leading to the intensity I that can be measured in the detector

$$I(x) = |\Psi(\bar{r})|^2 = I_0 e^{-2\beta kx} \quad (3.35)$$

where $I_0 = E_0^2$. By definition (Als-Nielsen & McMorrow 2001), the attenuation in an infinitesimal sheet of thickness dx is μdx , where μ is the *linear absorption coefficient*. From the attenuation in an infinitesimal thin sheet $-dI = I(x)\mu dx$, the attenuation of a sheet of finite thickness is given by solving the differential equation

$$I(x) = I_0 e^{-\mu x}, \quad (3.36)$$

and by comparing equation 3.35 to equation 3.36 we immediately see that $\mu = 2\beta k$. Equation 3.36 is known as the Beer-Lambert law. In a non-homogeneous sample where the linear attenuation coefficient is a function of space $\mu(x, y)$, the transmitted intensity is simply given by

$$I_{out}(x, y) = I_0 e^{-\int_{sample} \mu(x, y) dx}. \quad (3.37)$$

From these equations we see that the intensity drops exponentially, but the integrated attenuation $\int \mu(x, y) dz$ is linear, as required in equation 3.28. In order to reconstruct an image slice through our sample, we may thus consider the logarithm of the normalized intensity

$$\begin{aligned} \mathcal{P}_\theta(x') &= -\log \left(\frac{I_{out,\theta}(x')}{I_0} \right) \\ &= \int \mu(x', y') dy' \end{aligned} \quad (3.38)$$

at each projection as the input data to our tomographic reconstruction. Again, (x', y') denotes coordinates in the rotated frame that is rotated by the angle θ such that the projection is along the y' axis. What we reconstruct is then the attenuation coefficient of each voxel: $\mu(x, y)p_v$, where p_v is the width of a voxel (which is usually made equal to the width of a detector pixel).

Figure 3.8 shows an example of a recorded data set, where a single row of pixels in the detector is extracted and displayed as a sinogram. The

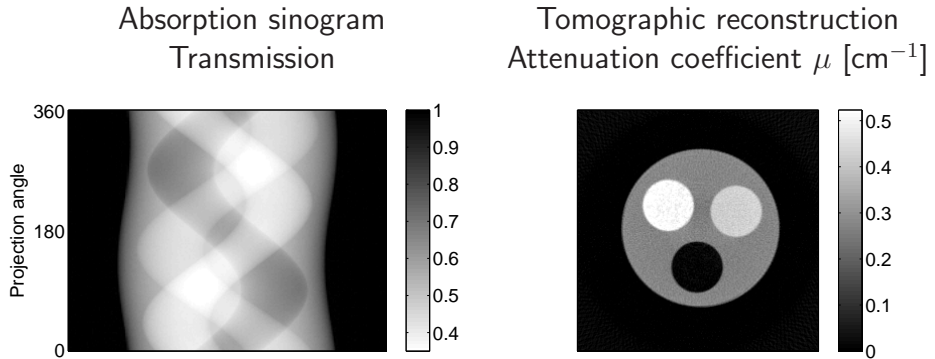


Figure 3.8. *Sinogram and tomographic reconstruction of a phantom with three circles of different density. The reconstructed slice is produced by filtered backprojection of the sinogram.*

projections for all angles recorded in this row of pixels are stacked to form the sinogram. As a result, each point in the object draws a sine shape, hence the name sinogram. Each point of the sinogram thus corresponds to a projection value $\mathcal{P}_\theta(x')$ where θ is the line number and x' is the row number of the point in the sinogram.

So far we have assumed that the data to be reconstructed are recorded at a parallel beam setup, *i.e.* that the incoming beam is not diverging. This is a good approximation for the experimental data treated in this thesis, where the angles are sufficiently small that the X-rays may be considered as parallel to the optical axis. But it should be mentioned here that fan-beam or cone-beam effects should be taken into considerations when dealing with a very short setup, such as that in a medical CT scanner.

3.2.2 Tomographic reconstruction of phase data

With the attenuation coefficient μ reconstructed from absorption data, we can calculate the imaginary part of the complex index of refraction $n = 1 - \delta + i\beta$. But the real part δ must be reconstructed from the phase contrast data.

Reconstruction of the phase shift in each voxel $\delta(x, y)p_v$ is straight forward to calculate from projected phase shifts, using standard tomographic reconstruction algorithms as described above. But with the grating based interferometer, we do not measure the projected phase shift. What we do measure, is the projected *differential* phase shift.

One way to solve the tomographic reconstruction is then to simply integrate the measured signal, and then apply the reconstruction as described

above. But this turns out not to be the best solution. The constant of integration makes a simple integration of the differential data ambiguous, and there is a risk of introducing artifacts in the reconstruction. In particular in the case of local reconstruction, where the projection data is truncated to a size smaller than the sample, the missing constant of integration give significant artifacts.

Another solution to the problem of reconstructing differential phase data, is to introduce an imaginary filter in the filtered backprojection algorithm, rather than the Ram-Lak ramp filter used above (in equation 3.31). The Fourier transform theorem for derivatives

$$\mathcal{FT} \left(\frac{df(x)}{dx} \right) = 2\pi ir\tilde{f}(r) \quad (3.39)$$

states that the Fourier transform, \mathcal{FT} , of the derivative of a function, $f(x)$, is equal to the Fourier transform of that function, $\tilde{f}(r)$, multiplied by the linear function $2\pi ir$. In other words, we can introduce a new filter function

$$\tilde{h}(r) = \frac{|r|}{2\pi ir} \quad (3.40)$$

that takes the differential phase signal as input for the tomographic reconstruction. By using this new filter, the differential phase data is integrated in Fourier space.

The projection function $\mathcal{P}_\theta(x')$ that is the logarithm of the normalized intensity in the case of absorption tomography above, is now substituted by the refraction angle $\alpha_\theta(x')$

$$\alpha_\theta(x') = \frac{\lambda}{2\pi} \frac{\partial\Phi(x')}{\partial x'}, \quad (3.41)$$

as known from equation 2.28. The measured quantity, the transverse shift $S_\theta(x')$ of the interference pattern in each pixel, is related to α_θ by

$$\alpha_\theta(x') = \frac{S_\theta(x')}{d} \quad (3.42)$$

and as d is a known quantity we thus have a direct measure of α . Relative to a wave propagating in vacuum, the total phase shift Φ of a plane wave traveling in the y direction through a homogeneous plate of thickness d , is derived from equation 2.4 as

$$\Psi(x) = E_0 e^{i(-\delta)kd} e^{-\beta kd} \quad (3.43)$$

$$\Phi(x) = -\delta kd. \quad (3.44)$$

Note that the relative index of refraction has been used, $n_{rel} = n_{sample} - n_{vacuum} = -\delta + i\beta$, to get a relative phase shift. By definition $n_{vacuum} = 1$, and as $n_{sample} < 1$ the relative phase shift is negative corresponding to a phase velocity greater than the vacuum speed of light.* In the case of an inhomogeneous sample where the index of refraction is a function of space, the total phase shift is given by integration along the beam path

$$\Phi(x, y) = \int_{sample} -\delta(x, y) k dy. \quad (3.45)$$

Combining this with equation 3.41 we can now derive the angular shift as

$$\alpha_\theta(x') = \frac{\lambda}{2\pi} \frac{\partial \Phi(x')}{\partial x'} \quad (3.46)$$

$$= -\frac{\lambda}{2\pi} \frac{\partial}{\partial x'} \int \delta(x', y') k dy' \quad (3.47)$$

$$= -\frac{\partial}{\partial x'} \int \delta(x', y') dy', \quad (3.48)$$

equivalent to equation 3.38, and this can be used as input for the filtered backprojection algorithm.

The procedure for tomographic reconstruction of phase data is the same as the procedure to reconstruct absorption data, except for the imaginary filter $\tilde{h}(r)$ replacing the Ram-Lak filter $|r|$. Equivalent to the filtering function \mathcal{G} introduced in equation 3.32 we now introduce a filtering function \mathcal{H} for differential data (equation 3.50). This changes the reconstruction equations to

$$\delta(x, y) = \int_0^\pi -\mathcal{H}(x \cos \theta + y \sin \theta, \theta) d\theta \quad (3.49)$$

$$\begin{aligned} \mathcal{H}(x', \theta) &= \int_{-\infty}^{\infty} \tilde{\alpha}(r, \theta) \tilde{h}(r) e^{i2\pi x' r} dr \\ &= \int_{-\infty}^{\infty} -2\pi i r \tilde{\delta}(r, \theta) \frac{|r|}{2\pi i r} e^{i2\pi x' r} dr \end{aligned} \quad (3.50)$$

$$\tilde{\alpha}_\theta(u') = \int \alpha_\theta(x') e^{-i2\pi(x' u')} dx', \quad (3.51)$$

where equation 3.49 is the backprojection corresponding to equation 3.33.

*Einstein's Special Theory of Relativity states that the speed of light in vacuum is absolute. This means that the group velocity $v_g = d\omega/dk$ must be less than c , which it is indeed. A phase velocity $v = \omega/k$ greater than the speed of light is not a violation of the Special Theory of Relativity, as the phase carries no energy.

Tomographic reconstruction of the real part δ of the refractive index from differential phase contrast images has now been established with the following procedure:

1. Calculate the Fourier space slices from the differential projection data (equation 3.51).
2. Perform the filtering by calculating $\mathcal{H}(u', \theta)$ with the new filter $\tilde{h}(r)$ (equation 3.50).
3. Backproject filtered data (equation 3.49).

3.2.3 Dark-field tomography

Due to the resemblance between the linear absorption coefficient μ and the linear diffusion coefficient ϵ , the tomographic reconstruction of the dark-field signal is completely analogue to the reconstruction of the standard absorption signal.

A tomographic reconstruction of ϵ may be calculated by setting the projection function equal to the logarithm of the measured visibility, analogue to equation 3.38

$$\mathcal{P}_\theta(x') = -\log \frac{p^2}{2\pi^2 d^2} V_\theta(x') \quad (3.52)$$

$$= \int \epsilon(x', y') dy', \quad (3.53)$$

and then using the filtered backprojection algorithm with the standard filter function.

Chapter 4

Results

Grating based phase contrast imaging has been realized at many occasions at different facilities during the work for this thesis. The experimental work presented here is divided into three categories after the type of X-ray source used in the experiment. As previously discussed, the properties of the X-ray source play a crucial role in the phase contrast and dark-field signals.

Most of my work has been done at the *Paul Scherrer Institut* (PSI) in Switzerland at a standard X-ray tube in a small setup on a table measuring 1.5 x 2.5 meters. Though the visibility of the interference pattern is low at an X-ray tube, due to a very broad energy spectrum and low transverse beam coherence, phase contrast images can be achieved at a tube. Opposed to synchrotrons where the beam is very small, the field of view at an X-ray tube can be several centimeters, allowing for larger samples to be imaged. At this setup different conditions for phase contrast imaging have been tested, and a selection of the results from these experiments is given in section 4.1 '*X-ray tube*' below.

Additionally, experiments have been conducted at the *Compact Light Source* (CLS), which is a new miniature synchrotron produced by *Lyncean Technologies Inc.* in Palo Alto, California USA. The CLS has a 4 x 2 meters electron storage ring running at 25 MeV, and an insertion device consisting of a laser cavity with a laser pulse counter propagating the electron bunch (Loewen 2003). X-rays are generated at head-on collisions between laser pulse and electron bunch. The generation of X-rays can be described as inverse compton scattering of the laser photons, or as synchrotron radiation where the field of the laser pulse is considered as an undulator field (Huang & Ruth 1998). The advantages of a CLS is that the source size is so small, that 10 meters from the source the transverse coherence length is long enough that the beam can be used for grating interferometry without the source grating G_0 that is necessary at X-ray tubes. Further, the energy bandwidth of the

X-ray beam is a few percent, which can easily be handled by the grating interferometer such that the visibility does not suffer like at sources with a broad spectrum. The angular beam divergence is much larger at the CLS than at other synchrotrons where the electron energy is in the GeV range. This is ideal for the grating interferometer that can utilize the larger divergence to achieve a larger field of view than is possible at other synchrotrons. The result presented here were obtained at the CLS prototype currently in development at Lyncean Technologies Inc. The images presented are the result of the very first imaging experiments at the CLS, see publication V.

Finally, a number of experiments have been performed at the synchrotrons in France at the *European Synchrotron Radiation Facility* (ESRF), and in Switzerland at the *Swiss Light Source* (SLS). At an imaging beamline at a synchrotron, the source size is very small and the distance from the source to the experiment station large, resulting in a very good transverse beam coherence. The monochromator is typically a silicon single crystal, with a bandwidth of 10^{-4} . The result is a maximal visibility of the interference pattern. At the very long beamline ID-19 at ESRF, the beam is as big as $14 \times 40 \text{ mm}^2$ (vert. x horiz.) at the experimental station, allowing for high resolution images of animal organs such as the rat brain published in publication I Pfeiffer et al. (2007), or a small animal such as the frog presented in the '*Synchrotron data*' section 4.3 below.

4.1 X-ray tube

4.1.1 Setup

The experiments described in this section were conducted at PSI in Switzerland. The X-ray source used is a Seifert ID 3000 X-ray generator with a fixed tungsten anode, operated at an acceleration voltage of 40 kV and a current of 30 mA. The focus spot of the electron beam on the tungsten target is 8 mm horizontally and 0.4 mm vertically, but the effective source size as seen from the detector is 0.8 mm x 0.4 mm due to a 6 degree inclination of the X-ray beam direction with respect to the target plane.

The source grating G_0 should be mounted as close to the source as possible. In this case, it is mounted directly on the tube, just on top of the beryllium window separating the vacuum in the tube from the ambient air. The grating interferometer, consisting of a phase grating G_1 and an analyzer grating G_2 , is located 1.4–1.6 meters from the source, and the detector is located immediately behind the interferometer, see figure 4.1. As described in the *Theory* chapter, the distances d and L must be matched to fit with

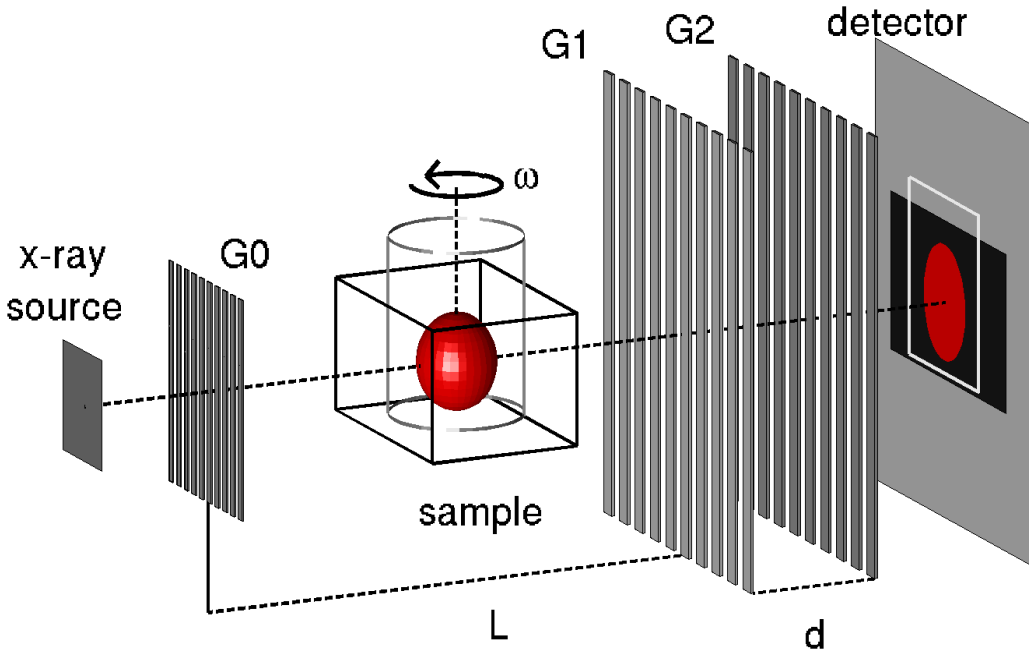


Figure 4.1. Sketch of the experimental setup. Not to scale. The source grating G_0 , acting as a slit array, is mounted directly on the X-ray tube. The interferometer consisting of gratings G_1 and G_2 is placed $L \approx 1.5$ meters from the source. The sample is placed immediately in front of the interferometer, and the detector is placed immediately after.

the grating design and the X-ray energy.

In the experiments at the X-ray tube, two different sets of gratings were used. One set of gratings was designed for the first fractional Talbot distance, and the other set of gratings was designed for the fifth fractional Talbot distance. Both sets were designed for an X-ray energy of 28 keV.

The grating specifications for the first and fifth fractional Talbot distance are listed in table 4.1. The analyzer grating G_2 is more challenging to produce than the other gratings because it needs to have gold deposited with a very fine period. For this reason the same grating is used in both configurations, and G_0 and G_1 are designed to comply with it. All gratings are designed and produced at PSI by C. David and C. Gruenzweig as described in (David et al. 2007a).

At an X-ray energy of 28 keV ($\lambda = 0.44 \text{ \AA}$), the first fractional Talbot distance of a $4.0 \mu\text{m}$ grating period in a parallel beam experiment is

$$a = \frac{g_1^2}{8\lambda} = \frac{16 \times 10^{-12} \text{ m}^2}{8 \times 0.44 \times 10^{-10} \text{ m}} = 45 \text{ mm} \quad (4.1)$$

| Grating parameters | 1st Talbot | | 5th Talbot | | Both |
|----------------------------|------------|-------|------------|-------|-------|
| Grating | G_0 | G_1 | G_0 | G_1 | G_2 |
| Period g (μm) | 73.0 | 3.89 | 14.1 | 3.50 | 2.00 |
| Dimension [h] (mm) | 10 | 64 | 10 | 64 | 64 |
| Dimension [v] (mm) | 4 | 64 | 4 | 64 | 64 |
| Material | Au/Si | Si | Au/Si | Si | Au/Si |
| Height (μm) | 50 | 36 | 50 | 36 | 22 |
| Duty cycle | 0.3 | 0.5 | 0.3 | 0.5 | 0.5 |

Table 4.1. Grating parameters for interferometer setup at X-ray tube. The gratings G_0 and G_1 are designed to give an interference pattern with a period of $2 \mu\text{m}$ such that the same G_2 grating can be used in either configuration. The inter-grating distances are $L = 160 \text{ cm}$, $d = 4.4 \text{ cm}$ for the first fractional Talbot distance and $L = 140 \text{ cm}$, $d = 20 \text{ cm}$ for the fifth fractional Talbot distance.

by use of equation 2.30. In a parallel beam experiment a $4.0 \mu\text{m}$ phase grating produces a $2.0 \mu\text{m}$ interference pattern, but due to the magnification factor $M = (L + d)/L$ the grating period and inter-grating distances must be corrected.

In section 2.3 about the *Grating Interferometer*, the equations on page 25 assume that the periods of the gratings are known, and then the distances are calculated. But when preparing an experiment, this is not always the case. We rather have the analyzer grating G_2 and a confined space for the setup, determining a restriction on the total length $l + d$ of the experiment. If we settle on a distance L from the source grating to the interferometer, we can calculate d , g_1 and g_0 from the equations

$$d = m \frac{g_1^2}{8\lambda} \frac{L + d}{L} \quad (4.2)$$

$$\frac{L + d}{L} = \frac{2g_2}{g_1} \quad (4.3)$$

$$\frac{g_2}{g_0} = \frac{d}{L}, \quad (4.4)$$

which can be solved to give

$$d = -L \frac{1 - \sqrt{1 + 2mg_2^2/(L\lambda)} + mg_2^2/(L\lambda)}{1 - \sqrt{1 + 2mg_2^2/(L\lambda)}} \quad (4.5)$$

$$g_1 = -2g_2 \frac{1 - \sqrt{1 + 2mg_2^2/(L\lambda)}}{mg_2^2/(L\lambda)} \quad (4.6)$$

$$g_0 = g_2 \frac{L}{d} = -g_2 \frac{1 - \sqrt{1 + 2mg_2^2/(L\lambda)}}{1 - \sqrt{1 + 2mg_2^2/(L\lambda)} + mg_2^2/(L\lambda)}. \quad (4.7)$$

In this case the distance L for the first fractional Talbot setup is chosen to be 160 cm, yielding the three values:

$$\begin{aligned} d &= 44 \text{ mm}, \\ g_1 &= 3.89 \mu\text{m}, \\ g_0 &= 73 \mu\text{m}, \end{aligned}$$

to make the interference patterns from the individual line sources of G_0 overlap with the period of G_2 , $g_2 = 2.0 \mu\text{m}$. The duty cycle of G_0 of 0.3 means that the width of each line source is $s = 0.3 \times g_0 = 22 \mu\text{m}$, giving a reduced source size of $w = 0.3 \times g_2 = 0.6 \mu\text{m}$ such that $w < g_2/2$. The period of the interference pattern is half the period of G_1 multiplied by the magnification factor M , $g_1 M/2 = 2.0 \mu\text{m}$.

Similarly for the fifth Talbot distance, the distance L is chosen to be $L = 140$ cm, giving $d = 197$ mm and $g_1 = 3.5 \mu\text{m}$. The source grating has period $g_0 = 14.1 \mu\text{m}$ with a source size $s = 4.2 \mu\text{m}$ and a reduced source size $w = 0.6 \mu\text{m}$. The period of the interference pattern is still $g_1 M/2 = 2.0 \mu\text{m}$.

The grating interferometer is very robust in the sense that small deviations from the calculated values do not have a large effect on the final interference result. If the period of G_1 is slightly wrong, the distance d can be adjusted to obtain the correct magnification factor M . A slight variation in d does not change the interference visibility much. Likewise, a deviation in g_0 from the calculated value can be compensated for by adjusting the distance L .

If the distances in the setup are not correct, they can be optimized while observing the visibility of the interference pattern and occurrence of Moiré fringes. A wrong magnification factor will produce Moiré fringes parallel to the grating lines, while an angular misalignment around the optical axis give Moiré fringes perpendicular to the grating lines, and one grating must be rotated slightly to correct for this.

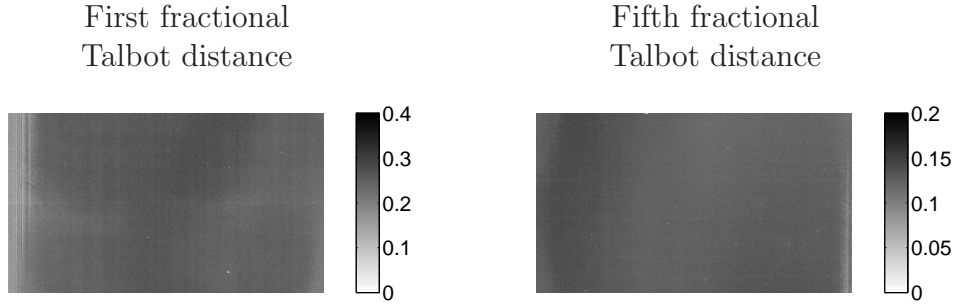


Figure 4.2. Visibility of the recorded intensity modulation. Note the different scale bars by the images. At the fifth fractional Talbot distance, the visibility is reduced to half the value.

Pilatus detector

The detector used in this experimental setup is a single photon counting pixelated solid state detector, the Pilatus 100k (Brönnimann et al. 2006). The properties of this detector differ from those of scintillator based CCD detectors in a number of ways. A threshold can be set for the photon energy, such that only photons above this energy threshold are detected. With this threshold set to 20 keV, a lower end of the energy spectrum is set. The upper end of the spectrum is given by the acceleration voltage in the X-ray tube which is 40 kV.

Each photon in each pixel is counted, the dynamic range is 20 bit, and the readout is very fast. The point spread function is a one-pixel wide top-hat, meaning that virtually no blurring occurs in the recorded image. The single pixel point spread function is a great advantage in imaging of sharp edges, and in particular tomographic reconstructions gain from the improved point spread and high dynamical range. A comparison of the Pilatus 100k detector with a scintillator based CCD detector system is given in publication III (Bech et al. 2008).

4.1.2 Visibility and sensitivity

The problem of reduced visibility of the interference pattern when performing interferometry at an incoherent source, such as an X-ray tube, has been discussed in sections 2.3 and 2.4. The visibility obtained in the current setup at the fifth fractional Talbot distance is illustrated in figure 4.2. As expected, the visibility of the reference beam is fairly low at the X-ray tube. Due to the poor beam coherence and a broad spectral width, the average visibility at the

first fractional Talbot distance is $\sim 24\%$, and at the fifth fractional Talbot distance only $\sim 12\%$. Even though the visibility is this low, and though the phase shift of the reference beam is quite noisy as illustrated in figure 3.3, the X-ray tube is very stable and a usable signal can be extracted from the data. Further examples of phase contrast images and dark-field images recorded at the X-ray tube are given in the sections below.

The sensitivity of refraction and scattering in the differential phase shift and dark-field signals can be changed by adjusting the parameters of the setup.

One parameter to vary, is the distance d between grating G_1 and grating G_2 in the interferometer. With the two sets of gratings at hand, this distance can be either $d = 4.4$ cm (first fractional Talbot distance) or $d = 20$ cm (fifth fractional Talbot distance). Figure 4.3 displays images recorded at each fractional Talbot distance.

At both distances, the absorption is the same. Hence, the two absorption images look very similar, with the only exception that the sample appears slightly larger at the fifth fractional Talbot distance, where the distance from sample to detector is larger. The differential phase contrast and the dark-field signal, that are derived from the position and visibility of the interference pattern, are very different at the two distances.

Refraction in the sample causes an angular deviation independent of Talbot distance, but the lateral shift of the interference pattern is linear with the propagation distance, and hence the differential phase contrast signal is *enhanced* by a factor five at the fifth fractional Talbot distance. However, the maximal transverse shift we can measure is $\pm 1 \mu\text{m}$, corresponding to $\alpha = \pm g_2/(2d) = \pm 23 \mu\text{rad}$ at the first fractional Talbot distance, but only $\alpha = \pm 5 \mu\text{rad}$ at the fifth fractional Talbot distance. *I.e.* the accepted angular range is *decreased* by a factor of five. On figure 4.3 the enhanced sensitivity in the phase contrast is clearly visible. The reduced angular range accepted can be recognized at the edges of the sample, where dark pixels can be seen along the bright left edge, and bright pixels along the dark right edge. In these pixels the angular deviation is larger than $\alpha = \pm 5 \mu\text{rad}$, causing a jump in the signal. This is referred to as phase clipping.

The dark-field signal is measured as reduced visibility. Incoherent scattering in small angles can be considered as a disturbance signal, and similar to the phase contrast signal, this scattering signal is enhanced by a larger propagation distance. On figure 4.3 this is clearly seen at the fifth fractional Talbot distance where the visibility is affected more than at the first fractional Talbot distance. As expected from the calculations in section 3.1.2, the dark-field signal is not linear in distance like the phase signal is.

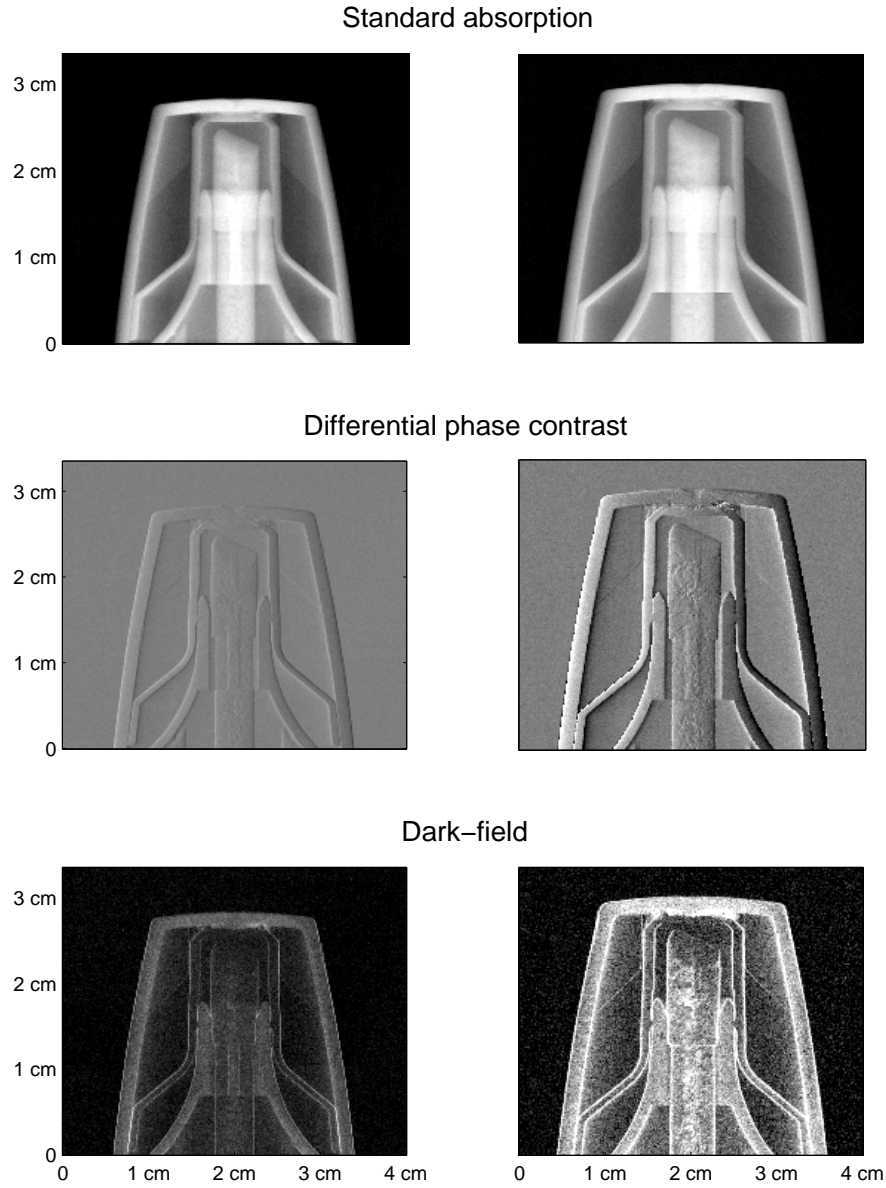


Figure 4.3. Images of a filter marker pen, recorded at the first fractional Talbot distance (left column) and fifth fractional Talbot distance (right column). All images have a linear grey scale. On the standard absorption images, black means no absorption and white is 30% absorption. On the differential phase contrast images, black means a transverse shift of the interference pattern of $0.5 \mu\text{m}$ and white is a transverse shift of the interference pattern of $-0.5 \mu\text{m}$. On the dark-field images, black means 100% visibility and white is 40% visibility. Note that the sample appears larger at the fifth fractional Talbot distance, due to the larger distance from sample to detector.

The described variation in measured signal at different Talbot distances can also be illustrated at a single Talbot distance, by placing the sample between G_1 and G_2 and varying the distance from sample to detector (see figure 4.4). There is nothing in the theory or in the assumptions that require the sample to be placed outside the interferometer. The distance d_s between the sample and the analyzer grating G_2 can be varied from 0 to 20 cm, which is the distance between the interferometer gratings G_1 and G_2 at the fifth fractional Talbot distance. Near the phase grating (at $d_s = 18.5$ cm) the dark-field signal and the differential phase signals are strong. The dark-field signal from the powdered sugar is saturated, as the beam coherence is completely destroyed and there is no visibility. Approximately halfway between G_1 and G_2 (at $d_s = 10.5$ cm) the phase signal has decreased proportionally, but the powdered sugar still leaves no visibility. Close to the analyzer grating (at $d_s = 3.0$ cm) the phase signal is almost gone, and the visibility of the interference pattern is no longer completely washed out by incoherent scattering in the powdered sugar.

There is no difference in the standard absorption image at different distances, except for a slight magnification. The silicon wafer (to the left in the images of figure 4.4) has a 73% transmission, and is clearly visible in the standard absorption image. But the homogeneous Si crystal and the parallel surfaces introduce no scattering or differential phase shift, and only the edge can be seen at the dark-field and differential phase contrast images. The gummi bear, water, and powdered sugar samples transmit approximately 65%, 70% and 80%, respectively, but the phase contrast and dark-field signals are very different. Small inhomogeneities in the gummi bear produces a pattern of bright spots in the dark-field image at $d_s = 18.5$ cm that reveals a structural difference between the gummi bear and the water. At the short propagation distance $d_s = 3.0$ cm the scattering signal is too weak to show a difference between gummi bear and water in the dark-field image. The structural difference between powdered sugar and the homogeneous samples is evident in the dark-field image at all distances, though the absorption is similar.

From equation 3.42 we expect the transverse shift $S(x)$ of the interference pattern to scale linearly with the sample to detector distance $S(x) = \alpha(x)d_s$, which is indeed what we see in figure 4.4. The visibility is expected to increase with decreasing sample to detector distance, equation 3.19, in agreement with the observed.

These four samples nicely illustrate the three different contrast modalities. Each of the three image signals show different properties of the samples. It is however evident that *e.g.* the scattering from the powdered sugar is too strong to provide useful quantitative information in dark-field and differential

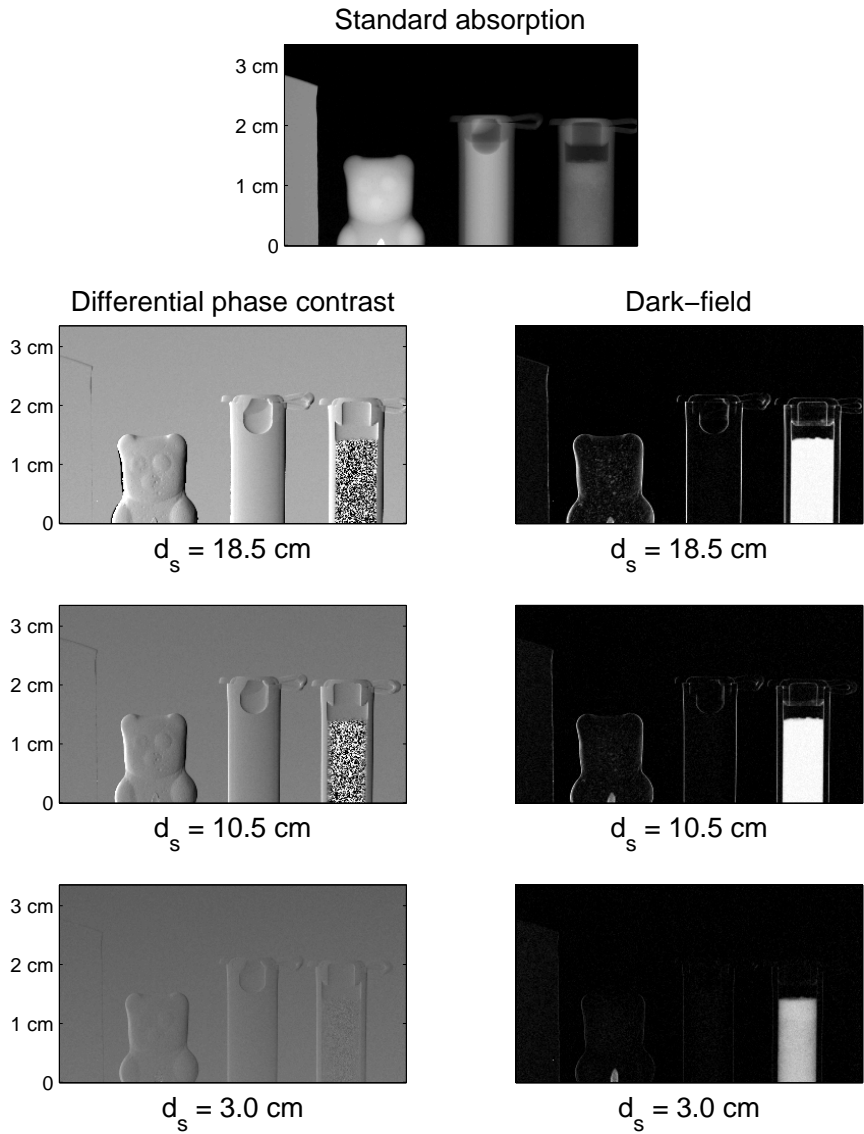


Figure 4.4. *Images of silicon wafer, gummi bear and plastic cylinders with water and powdered sugar. The images were recorded at the fifth fractional Talbot distance at decreasing sample to detector distance. All images have a linear grey scale. On the standard absorption image, black means no absorption and white is 50% absorption. On the differential phase contrast images, black means a transverse shift of the interference pattern of $0.5\text{ }\mu\text{m}$ and white is a transverse shift of the interference pattern of $-0.5\text{ }\mu\text{m}$. On the dark-field images, black means 100% visibility and white is zero visibility.*

phase contrast images. Hence, a tomographic reconstruction of these signals would not be possible and only the standard absorption tomography of this sample would make sense. Other samples may have very weak absorption and be best suited for phase contrast tomography, and yet other samples may prove to reveal valuable information in dark-field tomography. The following sections give examples of samples where each of the three contrast signals provide better quantitative information on the sample.

4.1.3 Sample for absorption images

Samples that are strongly scattering give a strong dark-field signal, which means that the beam coherence is strongly degraded. If the scattering is so strong that all visibility of the interference pattern is gone, the analysis of the grating interferometer data give random phase shift values and the dark-field signal is saturated.

An example of such a sample is wood. Due to the size of the fibers in the wood, the scattering will be very strong and even very thin samples will saturate the dark-field signal. Images of a wooden wedge are displayed in figure 4.5. The wedge is placed in front of the phase grating G_1 , at a setup for the fifth fractional Talbot distance. The wedge thickness goes from zero at the top to three millimeters at the bottom. Already at half a millimeter thickness, the visibility is gone and there is no dark-field or phase contrast. Note that the absorption is quite low, and that more than 95% of the intensity is transmitted at this point. It would be no problem to make standard absorption tomography of this sample (or even much thicker wood samples) at this setup.

4.1.4 Sample for phase contrast imaging

Soft tissue is difficult to image, as the density variations are low and provide little absorption contrast. Hence, good contrast in medical CT scanners is difficult to obtain in soft tissue regions such *e.g.* the abdomen.

Soft tissue imaging has been the subject of many recent publications on phase contrast X-ray imaging as discussed in the review of phase contrast imaging section 1.3. Common to the different techniques to achieve X-ray phase contrast is that soft tissue contrast is very challenging at X-ray tubes.

Increased image contrast of soft tissue has been achieved with grating based imaging at an X-ray tube, and the results presented here have been published recently in publication VI (Bech et al. 2009b).

Differential phase contrast images were made of a chicken heart submerged in formalin. The formalin fixated heart was contained in a cylindrical

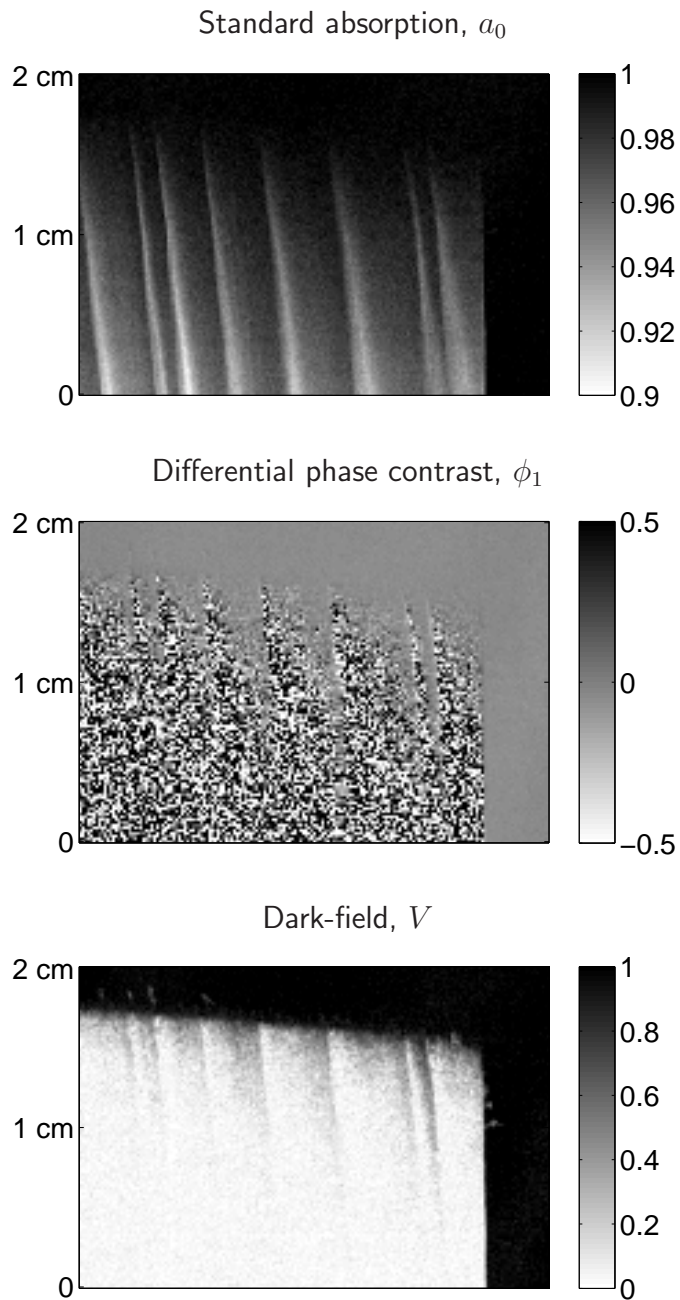


Figure 4.5. Images of wooden wedge. The images were recorded at the fifth fractional Talbot distance. All images have a linear grey scale. On the standard absorption image, black means no absorption and white is 10% absorption (90% transmission). On the differential phase contrast image, black means a transverse shift of the interference pattern of $0.5 \mu\text{m}$ and white is a transverse shift of the interference pattern of $-0.5 \mu\text{m}$. On the dark-field image, black means 100% visibility and white is zero visibility.

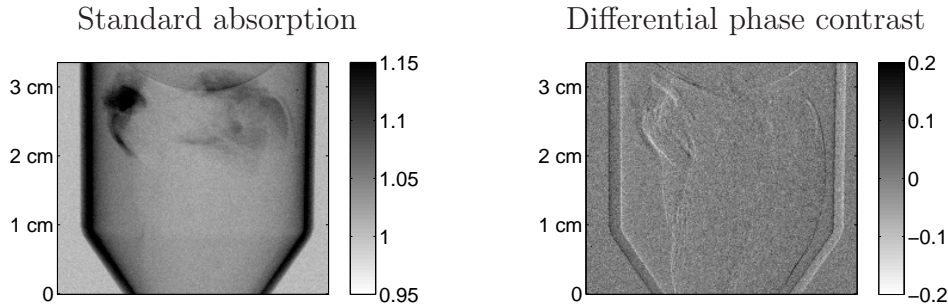


Figure 4.6. Standard absorption contrast (a) and differential phase contrast (b) images of chicken heart. The grey scale is linear on both images. On the standard absorption image, the transmission is given relative to water. On the differential phase contrast image, the range of the grey scale corresponds to a transverse shift of $\pm 0.2 \mu\text{m}$.

plastic tube, which again was submerged in a water bath with plane surfaces. The water bath ensures that the entire X-ray beam propagates through approximately 4 cm of material (water, formalin or sample) and that the beam is not too disturbed by the curved surface of the plastic cylinder containing the sample.

The experiments were conducted at the fifth fractional Talbot distance at the setup described above in section 4.1.1. Absorption and phase contrast signal were extracted from a phase stepping scan with 16 frames recorded while stepping the analyzer grating G_2 a total of 2 microns. Each frame was recorded with a 10 second exposure time, giving a total exposure time of 160 seconds. The standard absorption contrast and differential phase contrast images are displayed in figure 4.6, where the difficulty of soft tissue imaging is obvious; in the standard absorption image only the adipose tissue attached to the sample is distinguishable, and in the differential phase contrast image only the contour of the sample is visible. In both images the plastic container provides a stronger signal than the soft tissue sample.

As the sample container is submerged in a water bath, the images with an empty reference beam also contained a water bath. Consequently, the calculated X-ray transmission and phase shift will be values relative to water.

Despite the relatively poor contrast of the images, a considerable contrast enhancement can be obtained by tomography.

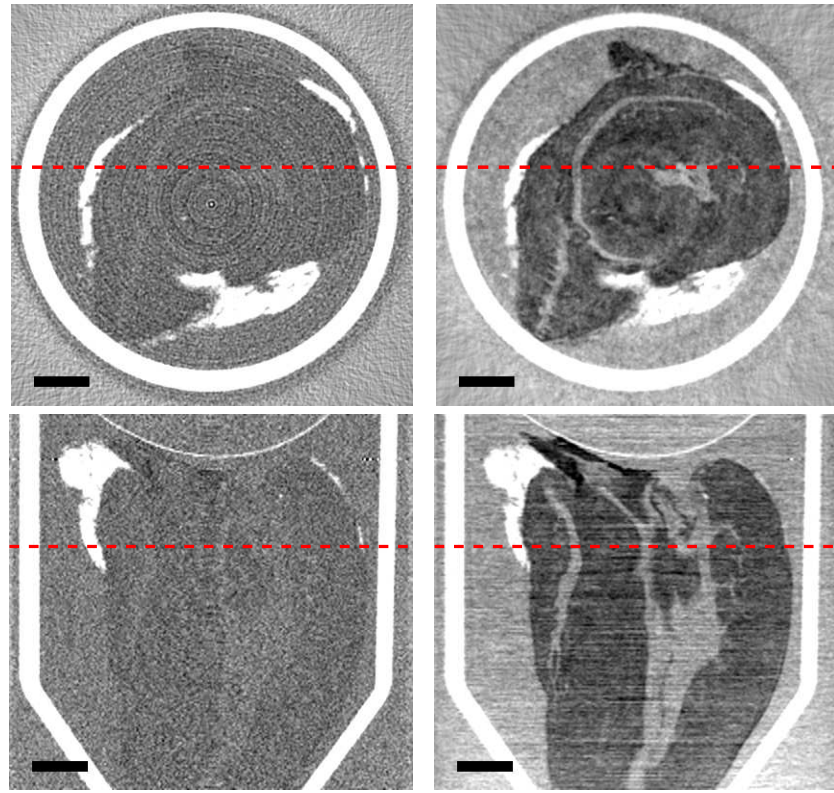


Figure 4.7. Computed tomography of chicken heart. Axial and frontal slices through the reconstructed tomography volume. Left column: standard absorption tomography. Right column: phase contrast tomography. Top: axial slices. Bottom: frontal slices. The dashed red lines indicate the intersection line of axial and frontal slices. The images are displayed on a linear grey scale. Voxel values along the red dashed lines are plotted in figure 4.8(left panel). The black scale bar corresponds to 5 mm.

4.1.5 Phase contrast tomography

The large number of images included in a tomographic reconstruction, will improve contrast due to the increased statistics.

Tomographic reconstruction of both standard absorption and differential phase contrast are computed from images recorded at 375 projections distributed evenly on the full 360° . An axial and a frontal slice through both tomograms are displayed in figure 4.7 for direct comparison.

Calculated values of absorption coefficient μ and of the real part δ of the index of refraction are plotted as linear grey scale values in the images. For a quantitative comparison, the values of μ and δ along the dashed red line

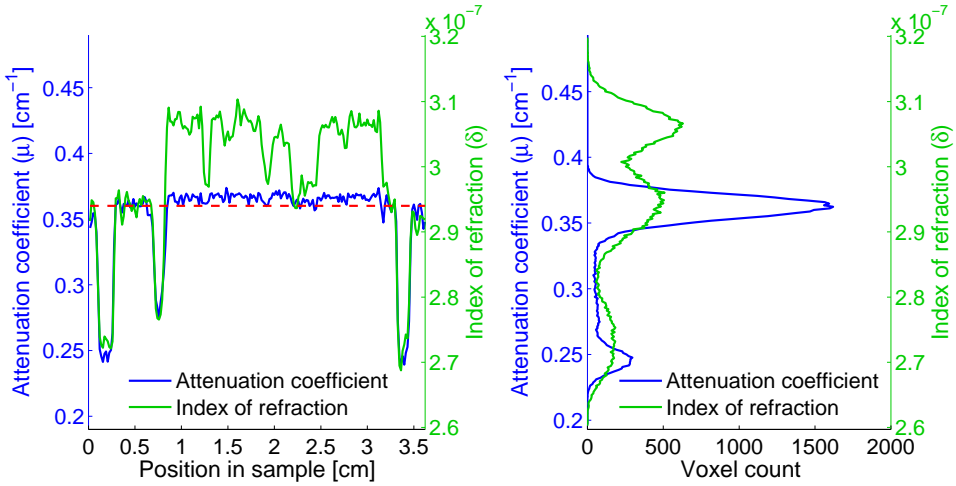


Figure 4.8. Left panel: Plot of attenuation coefficient μ and real part of refractive index δ along the red dashed line in figure 4.7. Right panel: Histogram of the voxels in the entire axial slice in figure 4.7.

in figure 4.7 are plotted in figure 4.8. We observe that the differences in the attenuation values (μ) between the muscle tissue and water are buried in the noise level, whereas they are well resolved in the corresponding phase-contrast signals (δ). The improved contrast is further exposed in the right panel of figure 4.8, which shows a histogram representation of all pixels in the axial slices in figure 4.7. In the phase contrast histogram two distinct peaks are seen at $\delta = 2.94 \cdot 10^{-7}$ and $\delta = 3.07 \cdot 10^{-7}$, corresponding to water and muscle tissue, respectively. The absorption histogram has only one peak at $\mu = 0.36 \text{ cm}^{-1}$ corresponding to both water and muscle tissue.

As previously mentioned the sample container is submerged in a water bath, and the images with an empty reference beam also contained a water bath. The projection images displayed in figure 4.6 show attenuation values relative to the absorption in water, and the refraction from the edges of the cylinder is less strong. The reconstructed values of μ and δ are hence normalized to the water values, and to get the true quantitative values of the sample the table values of water $\mu_{\text{water}} = 0.36 \text{ cm}^{-1}$ and $\delta_{\text{water}} = 2.94 \cdot 10^{-7}$ (Henke et al. 1993) are added to the reconstructed values.

To give an impression of the entire reconstructed volume, a selection of the reconstructed slices are displayed in figure 4.9. Four axial slices and four frontal slices through the volume all illustrate the fact that much higher contrast is obtained by reconstructing the real part of the refraction index from the differential phase contrast data compared to the standard absorption based tomographic reconstruction in this soft material sample.

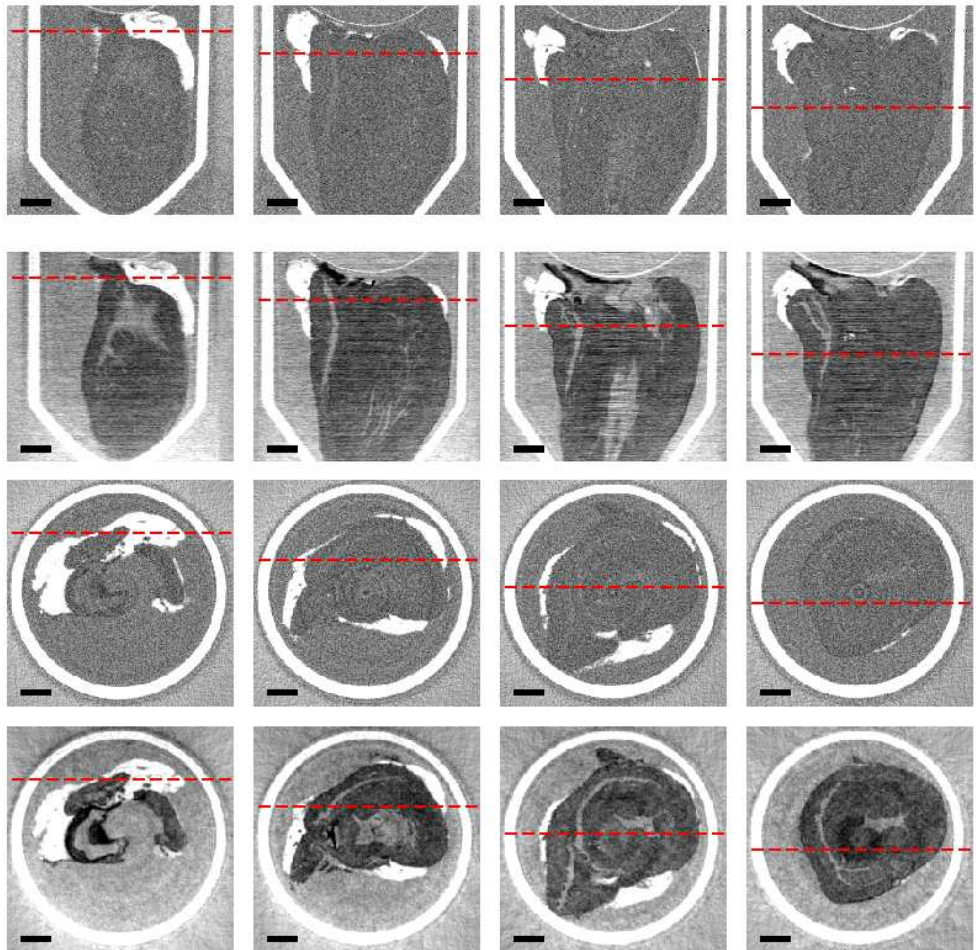


Figure 4.9. A collection of axial and frontal slices similar to the slices shown in figure 4.7. First and third row are absorption coefficient μ reconstructed from standard absorption data. Second and fourth row are real path δ of the refractive index reconstructed from differential phase data. For each row the red dashed lines indicate where the slices intersect. The black scale bar corresponds to 5 mm.

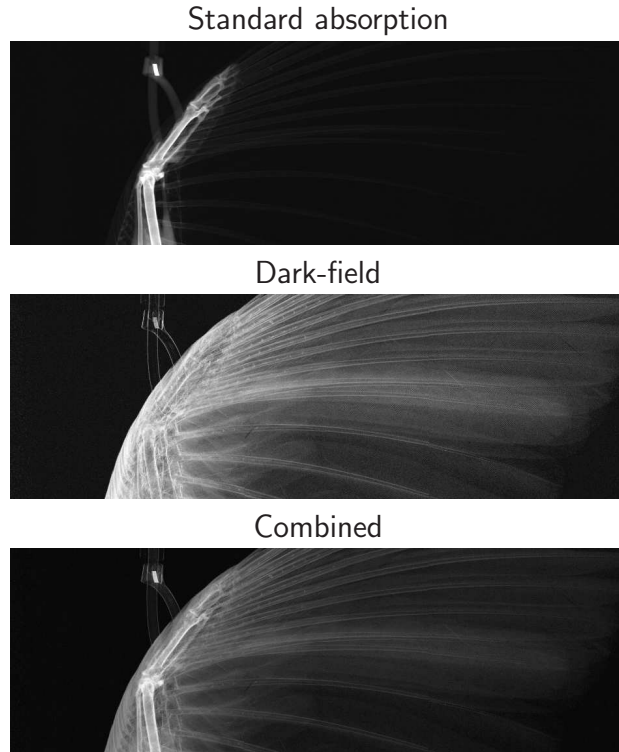


Figure 4.10. Wing of a blackbird. Topmost image is standard absorption and center image is dark-field image. The bones absorb much more than the feathers, and show up nicely in the standard absorption image. Feathers do not absorb much, but they do scatter, and show up nicely in the dark-field image. In the bottommost image the two signals are linearly combined to give an image with both bones and feathers visible. Each image is $16.3 \times 5.4 \text{ cm}^2$ and is stitched together from six individual images.

4.1.6 Sample for dark-field imaging

Where both absorption contrast and phase contrast images are related to the electron density in the sample, the dark field signal is generated from the internal structure of the sample, and can thus provide a signal fundamentally different from the others. In terms of biological tissue, it is well known that bones introduce a great amount of scattering.

Figure 4.10 displays three images of a blackbirds wing. The first image is a standard absorption image, the second one is the dark-field image, and the third image is a combination of the first two. In the combined image, both feathers and bones are clearly distinguished. The dimensions of each image is $16.3 \times 5.4 \text{ cm}^2$; much larger than gratings and detector. Due to the large size of the sample each of the images presented are stitched together from six

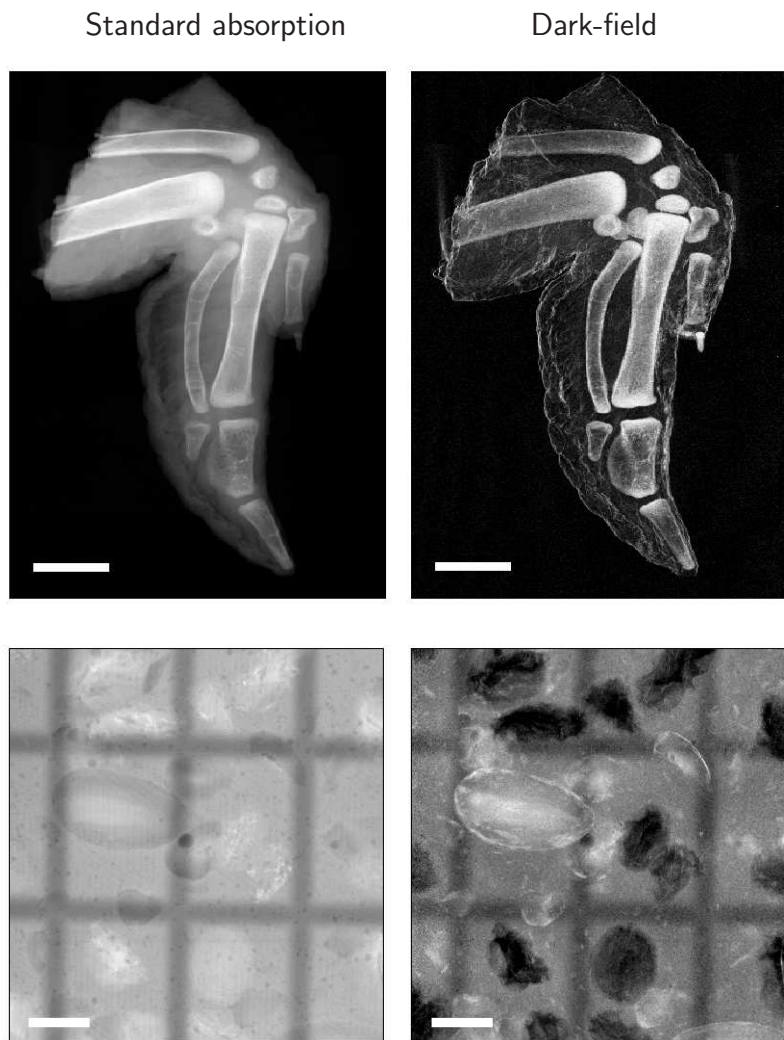


Figure 4.11. Standard absorption and dark-field images of chicken wing and swiss chocolate. Top, inverted grey scale: Plucked wing of a chicken as bought from the grocery. Each image is $5 \times 7 \text{ cm}^2$ and is stitched together from three individual images. Bottom: Plate of chocolate containing almonds and raisins. Each image is $6.2 \times 6.5 \text{ cm}^2$ and is stitched together from two individual images. The scale bars correspond to 10 mm.

individual images. The feathered wing is a very good example of a sample where the dark-field and absorption images complement each other well.

Another set of examples on samples well suited for dark-field imaging is displayed in figure 4.11. These images were recorded at the first fractional Talbot distance. The chicken wing displays the improved contrast of the dark-field image where bones are clearly distinguished from the soft tissue. Compared to the standard absorption image, the dark-field image enhance the soft tissue to bone contrast, and in particular the small bones in the joint are set off.

The plate of chocolate with almonds and raisins in figure 4.11 illustrate the fundamental difference between absorption and dark-field images well, as the fiber structure inside the almonds scatters the X-rays to make the almond appear bright in the dark-field image, whereas the soft raisins scatter less than the surrounding chocolate and hence appear dark.

The chicken wing and further results on dark-field imaging at the X-ray tube are available in publication II (Pfeiffer et al. 2008a).

4.1.7 Dark-field tomography

Strongly scattering samples may completely wash out the interference pattern and destroy the phase contrast and dark-field signals, as illustrated with the wood sample above. Tomographic reconstruction of the phase contrast and dark-field signals is only possible when the dark-field signal is not saturated, *i.e.* when some visibility remains. Figure 4.12 displays the recorded sinograms and the corresponding reconstructions of standard absorption, phase contrast and dark-field data of a phantom.

The phantom consists of a 22 mm polystyrol cylinder (mass density 0.6 g/cm³) with three 7 mm cylindrical holes. One hole is filled with a water/sugar solution, another with water and sugar crystals, and the third hole contains some cotton wool. In the absorption image the three holes are easily distinguished due to the different attenuation coefficient of the three substances. The reconstructed value of the absorption coefficient of the polystyrol cylinder is $\mu_{poly} = 0.28 \text{ cm}^{-1}$. For the water/sugar solution, $\mu_{solution} = 0.43 \text{ cm}^{-1}$, for the sugar crystals in water $\mu_{sugar} = 0.52 \text{ cm}^{-1}$, and the hole with cotton wool contains mostly air with no absorption. The absorption in the cotton itself is too low to be observed.

In the phase contrast image, the signal from the cotton wool is still too weak to be observed. The reconstructed values of the real part of the index of refraction deviation from 1, give $\delta_{poly} = 3.8 \times 10^{-7}$ for the cylinder, $\delta_{solution} = 3.9 \times 10^{-7}$ for the water/sugar solution and $\delta_{sugar} = 5.2 \times 10^{-7}$ for the sugar crystals in water. It is interesting to note that the real index of refraction

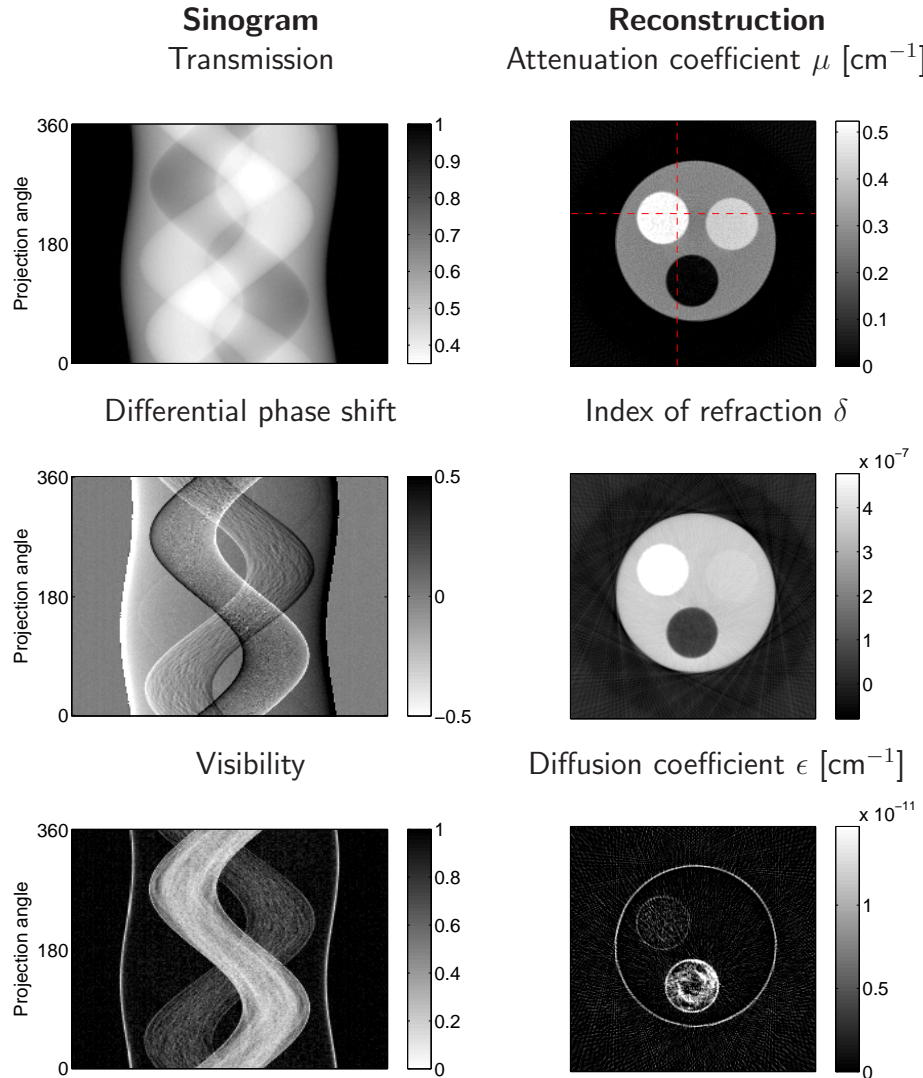


Figure 4.12. Absorption, phase contrast and dark-field sinograms and tomographic reconstructions of a phantom. The reconstructed slices display absolute values of linear attenuation coefficient μ , real part of refractive index δ , and linear diffusion coefficient ϵ . In the reconstruction of the attenuation coefficient the cylinder with sugar crystals is bright white ($\mu_{\text{sugar}} = 0.52 \text{ cm}^{-1}$), water/sugar solution is grey ($\mu_{\text{solution}} = 0.43 \text{ cm}^{-1}$) and cotton wool is black ($\mu_{\text{cotton}} \approx 0 \text{ cm}^{-1}$). The red dashed lines indicate the positions of the slices shown in figure 4.13.

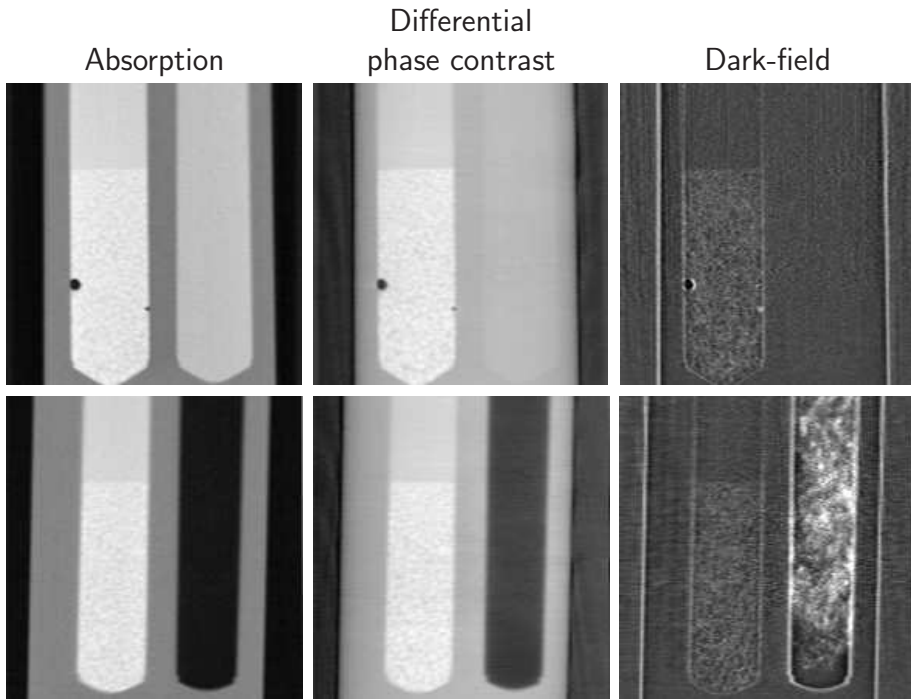


Figure 4.13. Slice through absorption, phase contrast and dark-field tomographic reconstructions. Top row: sugar crystals in water and a water/sugar solution. Bottom row: sugar crystals in water and cotton wool. The position of these slices are indicated by red dashed lines in figure 4.12.

of the polymer cylinder is almost exactly equal to that of the water/sugar solution, indicating that the electron densities are the same. The absorption of the polymer is however different from that of the sugar solution, due to the different chemical composition of the polymer. Polystyrol (with chemical composition $C_5H_8O_2$) has a fairly high amount of carbon, while the sugar ($C_{12}H_{22}O_{11}$) and water (H_2O) solution has a lower concentration of carbon. The different chemical compositions lead to different δ/β ratios, allowing the two compounds to have identical δ values but different β values or *vice versa*.

Finally, in the dark-field image we do see the cotton wool, and we can reconstruct a quantitative value ϵ for how much the sample scatters. The water sample is completely homogeneous and does not scatter at all. The sugar crystals show a little scattering from the edges of the crystallites, but as they are dissolving in water the edges are not very sharp and the scattering is weak. Cotton is a fiber crop with strong inhomogeneities that scatters. From the reconstruction we get values of the linear diffusion coefficient ranging from 8×10^{-12} to $2 \times 10^{-11} \text{ cm}^{-1}$. Though we do not have anything to compare this

number to currently, it is worth to note that we get a quantitative number from the dark-field reconstruction. In a future study, a table of linear diffusion coefficients could be made from experimental studies of different materials, and these values could be compared to the small angle scattering profiles of the materials.

Figure 4.13 displays two different slices from the reconstruction. These slices are perpendicular to the axial slices presented in figure 4.12, and intersect the cylindrical holes such that water and sugar is presented in the first row, while the second row presents sugar and cotton filled cylinders. Note in particular the lower right image, where the cotton wool is revealed by the dark-field signal.

4.2 Compact Light Source

The small size of the CLS makes it a synchrotron radiation source within reach for the conventional laboratory use. The insertion device in a CLS is a laser cavity rather than an array of permanent magnets as is the case at other synchrotrons, and hence the beam characteristics at the CLS are slightly different from the usual undulator beam.

The results presented here are also available in publication V (Bech et al. 2009a).

4.2.1 Source

The characteristic parameters for undulator radiation are γ (electron energy in units of rest mass) and λ_u (spatial period of undulator). The fundamental wavelength of X-rays emitted from a magnetic undulator is $\lambda_u/2\gamma^2$ (Als-Nielsen & McMorrow 2001), and for magnetic undulators λ_u is typically a few centimeters, so γ needs to be in the order of 10^4 to reach a fundamental wavelength in the range of an Ångström. The fundamental wavelength for a laser undulator is $\lambda_u/4\gamma^2$ (Loewen 2003), and as the laser undulator at the CLS has a wavelength of $\approx 1 \mu\text{m}$, we only need $\gamma \approx 50$ to get a fundamental wavelength in the Ångström range. For this reason the electron energy is two orders of magnitude lower than at large-scale synchrotron facilities. This allows the storage ring of the CLS to be scaled down to a few meters in circumference.

The beam divergence $\alpha \approx 1/\gamma$ of the CLS is much larger than at normal synchrotrons (Loewen 2003). This is an advantage in imaging, as a larger field of view can be obtained at shorter source to sample distances. At the current setup the CLS is operated at an electron energy of 25 MeV, *i.e.*,

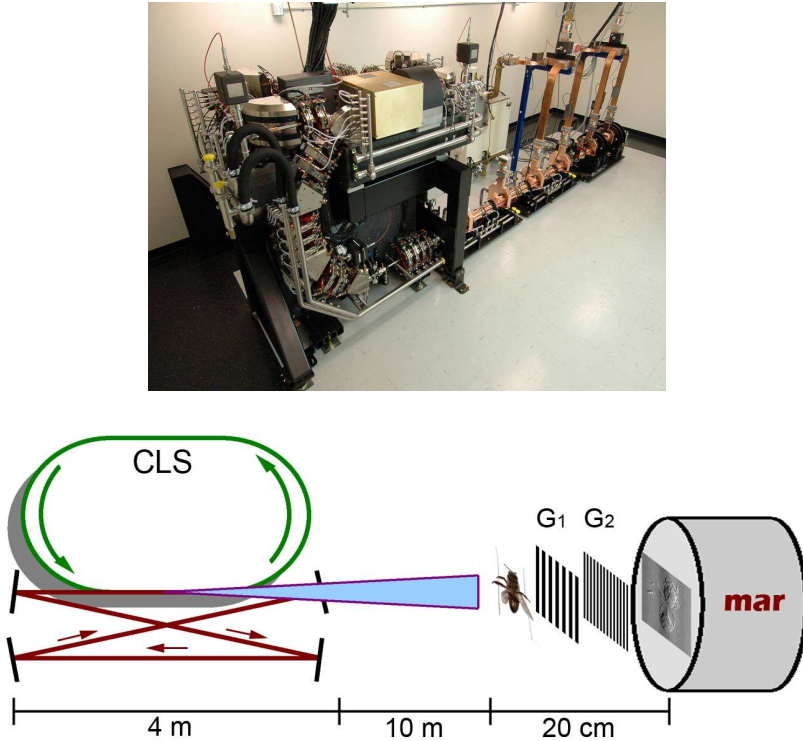


Figure 4.14. Top: Photograph of Compact Light Source. Bottom: Sketch of Compact Light Source and grating interferometer, not to scale. To the left is the Compact Light Source with an electron storage ring and a laser cavity. A cone X-ray beam is produced in the electron-laser intersection point, shining onto the sample. The grating interferometer to the right consists of two gratings, G_1 and G_2 and a MAR CCD detector.

at $\gamma = 50$ and with the beam collimated to $\alpha = 4$ mrad by a cylindrical aperture, giving a roughly circular beamsize of 4 cm in diameter ten meters from the source. The X-ray aperture can be opened to increase the beamsize by trading-off bandwidth, up to a maximum $\alpha \approx 1/\gamma$. For large apertures, the angular energy distribution is such that the X-ray energy is high in the forward direction, and falls off with increasing angle, giving a lower E_{peak} at the edges than in the center of the detector. For grating based imaging, an energy distribution width of a few percent will have little effect on the image quality, as discussed in section 2.4.2.

The CLS was operated at an X-ray energy of $E_{peak} = 13.5$ keV ($\lambda_{peak} = 0.92$ Å), with a full energy spread of $\Delta E/E_{peak} = 3\%$. The effective X-ray source size was estimated by recording the resolution of a sharp edge placed halfway between source and detector. The detected step function is smeared

by the source size and by the point spread function of the detection system. With an assumed point spread function of $78 \mu\text{m}$ (one pixel), we estimate the source size to $70 \mu\text{m}$ RMS.

4.2.2 Grating interferometer

This experiment was performed at the first fractional Talbot distance, using a grating system consisting of a phase grating G_1 with $3.99 \mu\text{m}$ pitch, and an absorption grating G_2 with $2.00 \mu\text{m}$ pitch. The two gratings have an area of $15 \times 15 \text{ mm}^2$, thus limiting the field of view to this area. The distance between the two gratings was $d_T = 22 \text{ mm}$, according to equation 2.32 with $m = 1$, $L = 8.65 \text{ m}$ and $\lambda = 0.92 \text{ \AA}$.

For each data set, nine phasesteps were recorded over two grating periods, yielding nine images from which the absorption, differential phase and dark-field signals were calculated. All images were recorded on a MAR CCD detector with square pixels of $78 \times 78 \mu\text{m}^2$.

4.2.3 Visibility

The graph in figure 4.15 displays the intensity in a pixel during a phase stepping scan, and the cosine fit (equation 3.5)

$$I(x_g) = a_0 + a_1 \cos\left(\frac{2\pi}{g_2}x_g + \phi_1\right), \quad (4.8)$$

calculated by Fourier analysis in the signal processing. Red markers indicate the intensity variation of the reference beam at different transverse positions of the analyzer grating G_2 . The average value a_0^r , the shift ϕ_1^r and the visibility a_0^r are indicated.

The visibility for each pixel is displayed in figure 4.15 as an image.

As can be seen, the visibility is fairly high. The average visibility of the reference beam is 80 % which means that the higher orders of the Fourier transform are non-negligible (but small) and should be included when calculating the visibility. In the present case nine phase steps were recorded over two grating periods, and we thus have access to the first and third order terms

$$I(x_g) = a_0 + a_1 \cos\left(\frac{2\pi}{g_2}x_g + \phi_1\right) + a_3 \cos\left(\frac{6\pi}{g_2}x_g + \phi_3\right). \quad (4.9)$$

The visibility $V = (a_1 + a_3)/a_0 = 0.80$ can be used to determine the projected source size w of

$$w = \frac{V - 1}{-3.19} g_2 = 0.125 \mu\text{m} \quad (4.10)$$

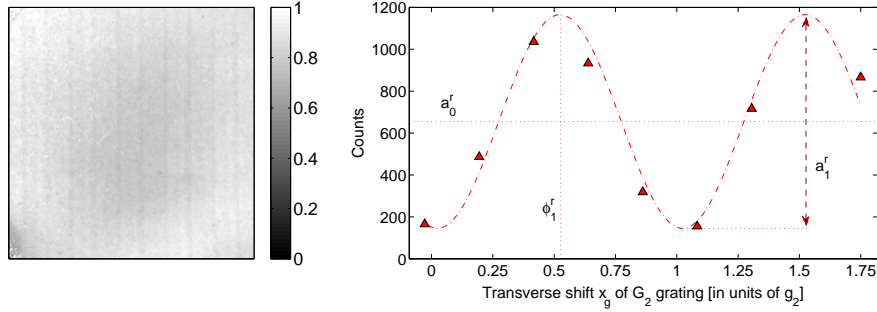


Figure 4.15. Visibility of the recorded intensity modulation. Left: Visibility of the empty reference beam, V^r . Right: Intensity variation in the center pixel as a function of grating position. Red markers indicate the measured phase steps. The average visibility of the reference beam is $\sim 80\%$.

by use of equation 2.54. In the present geometry this corresponds to a source size of $s = wL/d = 50\text{ }\mu\text{m}$. This is somewhat smaller than the $70\text{ }\mu\text{m}$ estimated, and we must conclude that either the point spread function of the detection system is more than one pixel, or the source is not Gaussian shaped as assumed.

4.2.4 Projection images

A number of different samples have been imaged with differential phase-contrast at the Compact Light Source. Figure 4.16 shows three images of a moth. The arrows point to two regions where phase contrast and dark-field images reveal details that are very difficult to see on the standard absorption image. One arrow points to a fishing wire (differential phase contrast) used for suspending the moth, the other arrow points to the leg of the moth (dark-field). Obviously the wings of the moth do not absorb much, but they do scatter and show up nicely in the dark-field image.

Though these images are not revolutionary and in principle could have been made at a standard X-ray tube, they serve to prove that the CLS can be used for X-ray imaging, and that the source size is small enough that a grating interferometer can produce phase contrast and dark-field images without a source grating G_0 . Once the CLS prototype has been optimized to produce an X-ray beam energy above 20 keV at increased flux, it may be used for high resolution, high contrast, X-ray tomography of medium sized samples with a quality previously only attainable at large scale synchrotron facilities.

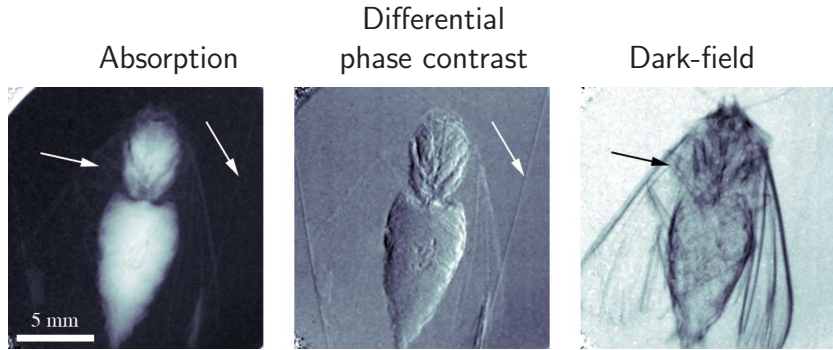


Figure 4.16. Images of a moth, recorded at a Compact Light Source. Left: Standard absorption contrast image. Center: Differential phase contrast image. Right: Dark-field image. Arrows indicate regions where phase contrast and dark-field images reveal details not visible on the standard X-ray image.

Further results from the Compact Light Source are available in publication V (Bech et al. 2009a).

4.3 Synchrotron data

A number of experiments have been performed at the third generation synchrotron radiation sources at ESRF in Grenoble, France. The experimental data presented here are from the beamline ID-19. The X-ray source at ID-19 is a wiggler, the storage ring energy is 6.03 GeV and the ring current is 200-400 mA.

4.3.1 Source

At ID-19 the experimental station is located $L = 140$ m from the X-ray source point, and hence the transverse beam coherence length is very good, providing excellent conditions for interferometry. It is thus possible to use large inter-grating distances of up to 0.5 meters.

4.3.2 Gratings

The experiment was performed at 24.9 keV with an inter-grating distance $d = 36.1$ cm corresponding to the ninth fractional Talbot distance *cf.* equation 2.32. The phase grating period was $3.99 \mu\text{m}$ and the absorption grating

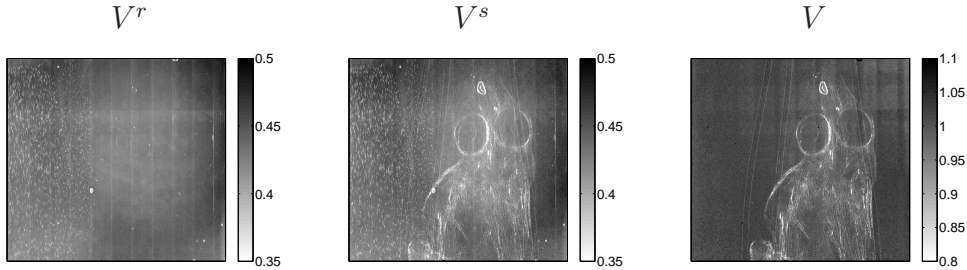


Figure 4.17. Visibility of the intensity modulation. Left: Empty reference beam, V^r . Center: Sample in beam, V^s . Right: Dark-field image obtained as the ratio between the first two images, $V = V^s/V^r$.

period was $2.00 \mu\text{m}$. Due to the long geometry of the beamline, the magnification factor is very close to one, and hence the period of the phase grating is close to $4 \mu\text{m}$ which would be the case in a parallel beam setup.

The accepted angular deviation caused by refraction in the sample is very narrow, and limited to $\alpha = \pm g_2/(2d) = \pm 2.8 \mu\text{rad}$ at the ninth fractional Talbot distance. While this is much less than the angular range accepted at the X-ray tube, the angular sensitivity at ID-19 is correspondingly higher, and the narrow bandwidth of the monochromator greatly improves the signal to noise ratio.

4.3.3 Visibility

The X-ray source at ID-19 is $30 \mu\text{m}$ vertical x $120 \mu\text{m}$ horizontal RMS (ESRF 2007), and we can estimate the beam coherence length at the interferometer.* With the grating lines mounted vertically, we are interested in the horizontal coherence length, which is characterized by

$$s = 120 \mu\text{m}$$

$$l_c = \lambda \frac{L}{s} = 58 \mu\text{m},$$

*From a source size point of view, the gratings should be mounted with the grating lines horizontally to exploit the higher coherence in the vertical direction. However, vertical instabilities in the electron beam give angular fluctuations in the range of micro radians, to which the interferometer is sensitive.

and we can calculate the projected source size and estimated visibility obtained at the interferometer from equation 2.54

$$\begin{aligned} w &= s \frac{d}{L} = 0.31 \mu m \\ V &= 1 - 3.19 \cdot \frac{w}{g_2} \\ &= 1 - 3.19 \cdot \frac{0.31 \mu m}{2 \mu m} \\ &= 0.51. \end{aligned}$$

This value can be compared to the measured visibility. Figure 4.17 displays the visibility in the empty reference beam and the visibility and dark-field image obtained with the sample in the beam. The average visibility of the reference beam is $V = 0.43$, *i.e.* slightly lower than the estimated value of $V = 0.51$. The visibility displayed in figure 4.17 is characterized by a noise pattern, probably originating from imperfections in gratings and beamline optics. It is thus not surprising that the visibility is lowered.

4.3.4 Projection images

Analogues to the visibility images displayed in figure 4.17 the absorption and phase shift images obtained for the empty reference beam and for the sample are displayed in figure 4.18. The sample is a decalcified frog of the Atelopus flavescens species (also known as Harlequin frogs), from the tropical rain forests in French Guyana. The frog is submerged into a water bath during the experiment. The reference images were recorded without the sample, but with the water bath, in the beam.

It is evident that the absorption in the frog is very similar to that of water, and it is impossible to distinguish the frog without subtracting the reference beam. The signals from refraction (phase contrast) and scattering (dark-field contrast) are somewhat stronger and the sample can be distinguished in the center images of figure 4.17 and figure 4.18 (bottom row). Though the images are noisy, a good result is achieved when the reference beam is used for corrections. Each of the corrected images from figures 4.17 and 4.18 are displayed again in figure 4.19 where the contrast signal of a line from each image is plotted together to illustrate the relative signal to noise ratio of the three contrast signals.

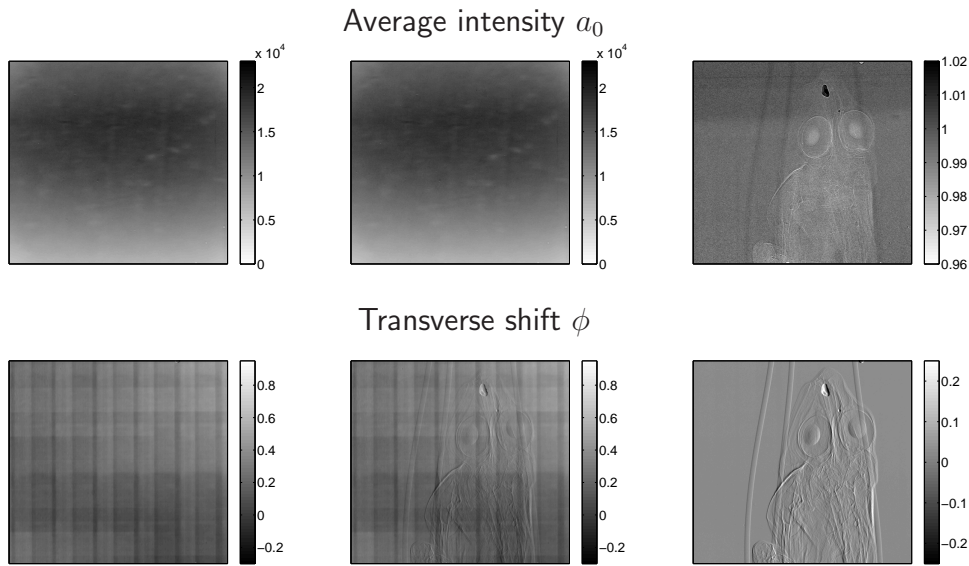


Figure 4.18. Recorded average intensity a_0 and transverse shift of the intensity modulation ϕ . Left: Empty reference beam, a_0^r , ϕ^r . Center: Sample in beam, a_0^s , ϕ^s . Right: Absorption in sample, $a_0 = a_0^s/a_0^r$ and differential phase image, $\phi = \phi^s - \phi^r$.

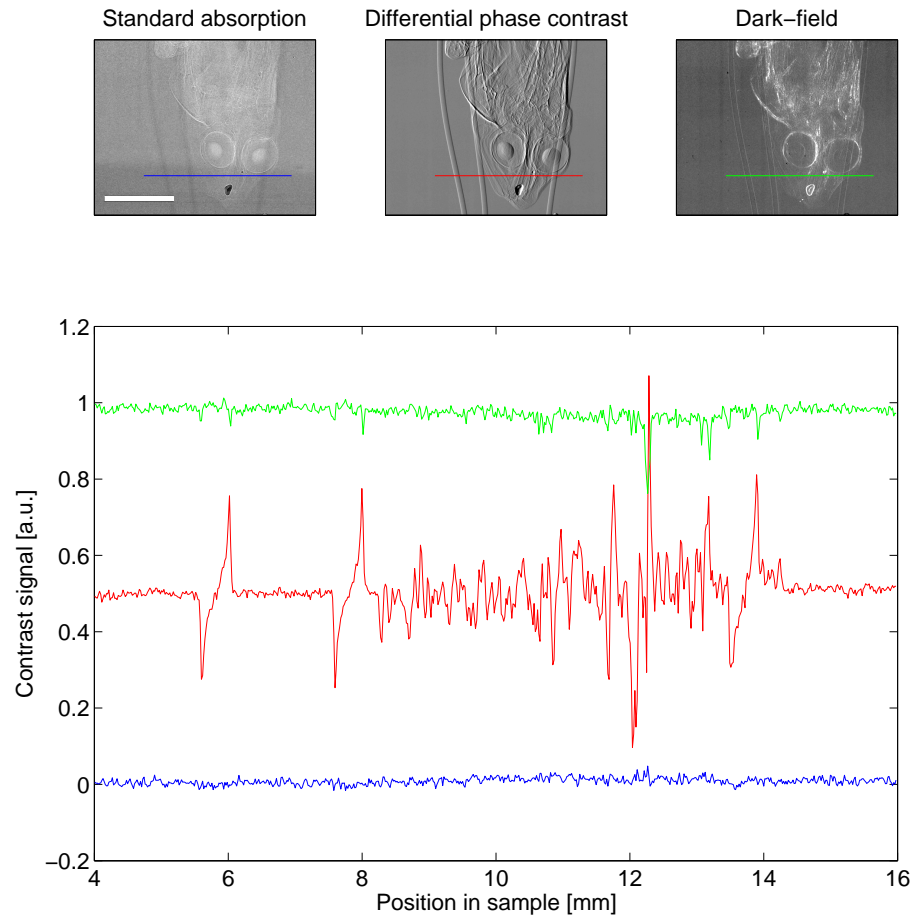


Figure 4.19. Projection images of Harlequin frog. Absorption and dark-field signals show little contrast, whereas the differential phase contrast is significant. The white scalebar is 5 mm. Intensity plots of absorption (blue), phase contrast (red) and dark-field (green) along the indicated lines are displayed in the graph. The contrast signals are plotted in an arbitrary unit with an offset to provide background noise oscillations of comparable levels. The signal magnitudes then differ significantly.

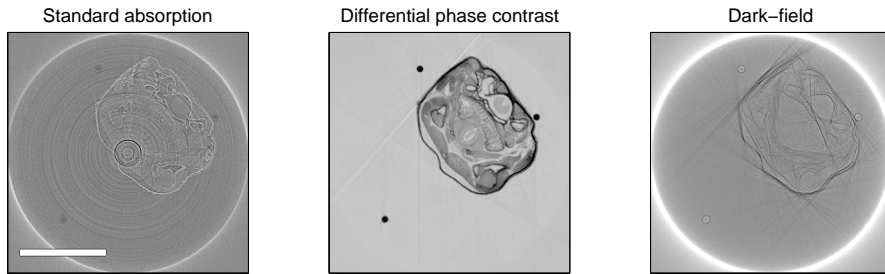


Figure 4.20. Reconstructed axial slices. The ring artifacts are in the noise level, but they appear dominant in the absorption contrast image due to the weak signal. The white scalebar corresponds to 5 mm.

The signal to noise ratio in figure 4.19 of the standard absorption image (blue line) is very poor, and the dark-field contrast (green line) is only slightly better. From this soft decalcified frog, the phase contrast signal (red line) is by far dominant compared to the other two signals.

4.3.5 Tomography images

In section 4.1 it was illustrated that a weak signal in a single projection can still produce a good result in the tomographic reconstruction. However, in the case of the frog recorded at the synchrotron, the absorption is so weak that the tomographic reconstruction is still very noisy, as displayed in figure 4.20.

The reconstructed dark-field signal reveals that most of the scattering originates from the edges (internal as well as external) and the signal to noise ratio of the reconstructed slice is poor.

The improved contrast from the phase signal is further improved by the tomographic reconstruction, and many details in the soft tissue are revealed. A three-dimensional rendering and a selection of four (frontal, sagittal and two axial) slices are displayed in figure 4.21, where the high dynamic range of different grey levels underline the contrast obtainable with this method.

Further results from phase contrast tomography at ID-19 are available in publication I (Pfeiffer et al. 2007) and publication VII (Pfeiffer et al. 2009).

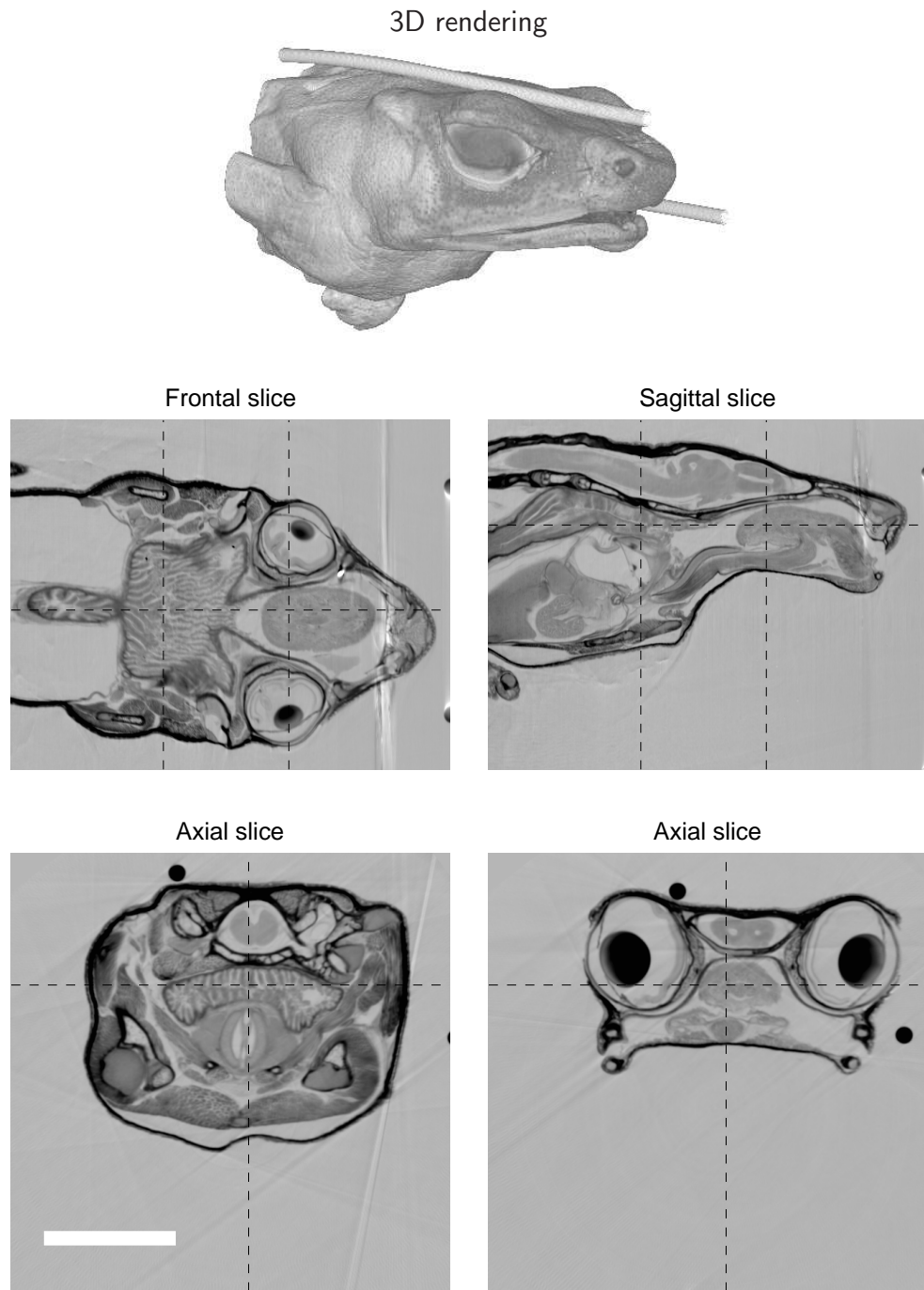


Figure 4.21. Phase contrast tomography of decalcified Harlequin frog reconstructed from the differential phase contrast data. A 3D rendering shows the surface of the frog. Internal features are shown in four slices through the volume. Black dashed lines indicate where the four slices intersect. The white scalebar corresponds to 3 mm. The fishing wires visible in rendering and slices are used for suspending the frog during the experiment.

4.4 Comparison of grating interferometry at different sources

From the results presented in this chapter, it is evident that the grating interferometer can provide phase contrast and dark-field images from any of the X-ray sources. In general, a higher beam coherence will produce better interference visibility and hence improved sensitivity.

Table 4.2 displays some of the parameters describing the grating interferometers used in this thesis. To compare the electron density sensitivity of the different experiments, an electron density range ρ_e is calculated from Snells law (equation 2.8) and the size of δ (equation 2.11) as

$$\rho_e = \frac{k^2 \delta}{2\pi r_0} \quad (4.11)$$

$$= \frac{k^2}{2\pi r_0} \left(1 - \frac{\sin(\alpha_i - \alpha_r/2)}{\sin(\alpha_i)} \right) \quad (4.12)$$

where α_r is the angular range of the setup and α_i is 45° . The sensitivity range is thus normalized by the square of the wavenumber k , and the calculated ρ_e is the density required in a 45° wedge to get the maximal accepted angular refraction. Comparing these numbers, we see that the highest sensitivity is achieved at the 9th fractional Talbot order at ID-19, followed by the 5th order at the X-ray tube, the 1st order at the Compact Light Source and finally the 1st order at the X-ray tube.

The synchrotron source has the best beam coherence in terms of both spatial coherence and spectral width. As a result, very large fractional Talbot distances can be used, giving extreme sensitivity to small refraction angles and small angle scattering. The presented phase contrast images of a Harlequin frog show a very high signal to noise ratio, producing contrast in the soft tissue with low density variation.

At the synchrotron one has the full freedom to choose a high fractional Talbot distance with high sensitivity, or a short distance with low sensitivity. But the field of view is limited to one or two centimeters. This means that the synchrotron is ideal for high resolution tomography with high contrast on small samples.

The opposite is true for an X-ray source, where the beam properties are quite different. The beam is highly divergent, allowing for large fields of view at a short distance. Though the source is too big to produce coherence at a short distance, a source grating can produce an array of line sources that will give enough coherence for grating interferometry. The visibility of the

| Source comparison | X-ray tube | | CLS | ID-19 |
|--|-----------------|-----------------|-----------------|-----------------|
| Talbot order | 1 st | 5 th | 1 st | 9 th |
| Talbot distance [mm] | 44 | 197 | 22 | 361 |
| Energy [keV] | 28 | 28 | 13.5 | 24.9 |
| Monochromatic | no | no | quasi | yes |
| Visibility [%] | 24 | 12 | 80 | 43 |
| Angular range [μrad] | 45 | 10 | 91 | 5.5 |
| Electron density range [\AA^{-3}] | 26 | 5.7 | 12 | 2.5 |

Table 4.2. Comparison of parameters for different setup with a grating interferometer. The electron density range is electron density needed in a 45° wedge to shift the interference pattern half a grating period.

recorded intensity modulation is poor, but improved contrast *is* obtained through the phase contrast and dark-field image signals.

The properties of the Compact Light Source are somewhere in between those of the third generation synchrotron and the X-ray tube. The beam is quasi monochromatic with a divergence allowing for centimeter sized samples ten meters from the source. The coherence is worse than at the synchrotron but better than at the X-ray tube, and the Compact Light Source is thus well suited for imaging tasks where the beam quality of the tube is insufficient, but where the sample is too large for the synchrotron beam. This makes the Compact Light Source a possible solution to high contrast, high resolution, X-ray imaging at hospitals or in clinical environments.

Further, high resolution tomography may be obtained at the Compact Light Source of samples that are inconvenient to transport to a synchrotron radiation facility.

Finally it should be noted that the Compact Light Source and the X-ray tube data presented here are not suffering from visibility loss due to X-ray optics, as nothing except gratings and sample is present in the beam. At ID-19 the visibility is lower than expected due to noise in the interference pattern.

Chapter 5

Conclusion

Grating based X-ray imaging has been described and experimental results have been presented.

The principles behind using gratings for imaging, and the theoretical description of wave propagation has been given and the revival of periodic waves, the Talbot effect, has been derived. The Fourier space propagation function derived from the Fresnel diffraction integral is used to simulate the propagation of different grating structures, and the fractional Talbot effect is illustrated. The grating interferometer described in this work utilizes the fractional Talbot affect to produce interference fringes.

The shape of the interference pattern recorded in the detector is depending on the size of the X-ray source size. This shape has been described in terms of the Fourier series, and the need for higher order cosine terms to describe the intensity modulation is accounted for. This also lead to a description of the recorded visibility as a function of source size. At setups with a long transverse beam coherence, the visibility decrease as a function of source size is linear. When the visibility is less than 50 %, the dependence is no longer linear, but exponential.

Basic image processing to produce projection images by Fourier analysis is described, and the resulting three kinds of image contrast have been illustrated. *Standard absorption* is the average reduced intensity in a pixel due to attenuation in the sample, *differential phase contrast* is the phase shift of the interference pattern caused by refraction in the sample, and *dark-field contrast* is the reduced visibility of the interference pattern caused by scattering in the sample.

The physical principles behind absorption and refraction are well understood from the complex index of refraction $n = 1 - \delta + i\beta$. The values of δ and β has a well known dependence on element number and X-ray photon

energy, which is described in the literature. A quantitative description of the dark-field signal has not previously been published, and a material dependent variable ϵ is introduced here as the *linear diffusion coefficient*, equivalent to the linear attenuation coefficient describing absorption. The exponentially decaying visibility as a function of sample thickness is justified by experimental data where the thickness of a scattering sample (paper) is increased in discrete steps.

Tomographic reconstruction by filtered backprojection is a well known process, and the procedure has been outlined here. Further, the tomographic reconstruction from differential projection data has been deduced, giving a reconstruction procedure involving an imaginary filtering function. Dark-field data can be reconstructed from the novel linear diffusion coefficient introduced, with a procedure identical to that of standard absorption data.

The experimental results presented here include data from three different types of X-ray sources; X-ray tube, synchrotron wiggler source, and the Compact Light Source based on inverse compton scattering. Both standard absorption, phase contrast, and dark-field images are presented from each source type.

Tomographic reconstructions of all three image signals are presented for X-ray tube and synchrotron source data. The presented tomography data include a sample with two substances that absorb equally well but are distinguishable in phase contrast (chicken heart in formaline solution, section 4.1.5), and a sample of the opposite case where the phase contrast of two substances is the same but the absorption is different (sugar solution in polymer container, section 4.1.7). This is a fundamental property of phase contrast imaging, as the response to photon energy and chemical composition of a compound is different for β and δ in the complex index of refraction. Further, dark-field tomography data of a cotton wool sample and high contrast reconstruction of a frog were presented. These results are previously unpublished.

For the Compact Light Source and the synchrotron radiation experiments where no source gratings are used and where the beam is mono-chromatic, the recorded visibility of the empty reference beams are displayed and compared to the expected visibility as calculated from the equations deduced theoretically.

Perspectives

It is evident that phase contrast is a source of extended contrast in X-ray imaging. This has been proven for all the different techniques reviewed in section 1.3, and this thesis adds to that conclusion.

There are different advantages to the techniques, in terms of resolution, dynamical range, field of view and beam requirements. The advantages of grating based imaging make this technique the most promising method for clinical use. The fact that grating interferometry works well at short setups with a standard X-ray tube makes it feasible for medical imaging at local hospitals or clinics. Very high contrast is also attainable at sources with better coherence properties such as the Compact Light Source, synchrotron radiation sources or even microfocus X-ray tubes.

Further, the dark-field image obtained from reduced visibility in the interference pattern is a great advantage of the grating based interferometer. The ability to image X-ray scattering may prove to be very useful, both in the area of medical imaging where the dark-field signal could add information to *e.g.* osteoporosis diagnosis, but also in industrial testing or in areas of national security (see publication II, Pfeiffer et al. (2008a) *supplementary online material*). The fact that dark-field imaging rely on a contrast modality fundamentally different from absorption and phase contrast makes it a valuable complement to X-ray imaging.

In conclusion, there is a great potential for grating based interferometry in the field of X-ray imaging.

Bibliography

- Als-Nielsen, J. & McMorrow, D. (2001), *Elements of Modern X-ray Physics*, John Wiley & Sons Ltd.
- Bech, M., Bunk, O., David, C., Kraft, P., Brönnimann, C., Eikenberry, E. F. & Pfeiffer, F. (2008), 'X-ray imaging with the pilatus 100k detector', *Appl. Radiat. Isotopes* **66**, 474–478.
- Bech, M., Bunk, O., David, C., Ruth, R., Rifkin, J., Loewen, R., Feidenhans'l, R. & Pfeiffer, F. (2009a), 'Hard x-ray phase-contrast imaging with the compact light source based on inverse compton x-rays', *Journal of Synchrotron Radiation* **16**, 43–47.
- Bech, M., Jensen, T. H., Feidenhans'l, R., Bunk, O., David, C. & Pfeiffer, F. (2009b), 'Soft-tissue phase-contrast tomography with an x-ray tube source', *Physics in Medicine and Biology* **54**, 2747–2753.
- Beckmann, F., Bonse, U., Busch, F. & Günnewig, O. (1997), 'X-ray microtomography (μ CT) using phase contrast for the investigation of organic matter', *Journal of Computer Assisted Tomography* **21**(4), 539–553.
- Bonse, U. & Hart, M. (1965), 'An x-ray interferometer with long separated interfering beam paths', *Appl. Phys. Lett.* **6**, 155–156.
- Bravin, A. (2003), 'Exploiting the x-ray refraction contrast with an analyser: the state of the art', *J. Phys. D: Appl. Phys.* **36**, A24–A29.
- Brönnimann, C., Eikenberry, E., Henrich, B., Horisberger, R., Huelsen, G., Pohl, E., Schmitt, B., Schulze-Briese, C., Suzuki, M., Tomizaki, T., Toyokawa, H. & Wagner, A. (2006), 'The pilatus 1m detector', *J. Syn. Rad.* **13**, 120–130.
- Clauser, J. F. (1998), 'Us patent no. 5,812,629: Ultrahigh resolution interferometric x-ray imaging'.

- Cloetens, P., Ludwig, W., Baruchel, J., Dyck, D. V., Landuyt, J. V., Guigay, J.-P. & Schlenker, M. (1999a), 'Holotomography: Quantitative phase tomography with micrometer resolution using hard synchrotron radiation x rays', *Appl. Phys. Lett.* **75**(19), 2912–2914.
- Cloetens, P., Ludwig, W., Baruchel, J., Guigay, J.-P., Pernot-Rejmánková, P., Salomé-Pateyron, M., Schlenker, M., Buffière, J.-Y., Maire, E. & Peix, G. (1999b), 'Hard x-ray phase imaging using simple propagation of a coherent synchrotron radiation beam', *Journal of Physics D: Applied Physics* **32**, A145–A151.
- Cloetens, P., Pateyron-Salomé, M., Buffière, J.-Y., Peix, G., Baruchel, J., Peyrin, F. & Schlenker, M. (1997), 'Observation of microstructure and damage in materials by phase sensitive radiography and tomography', *Journal of Applied Physics* **81**(9), 5878–5886.
- Cormack, A. M. (1963), 'Representation of a function by its line integrals, with some radiological applications', *J. Applied Physics* **34**, 2722.
- David, C., Bruder, J., Rohbeck, T., Grunzweig, C., Kottler, C., Diaz, A., Bunk, O. & Pfeiffer, F. (2007a), 'Fabrication of diffraction gratings for hard x-ray phase contrast imaging', *Microelectron. Eng.* **84**, 1172–1177.
- David, C., Nöhammer, B., Solak, H. H. & Ziegler, E. (2002), 'Differential x-ray phase contrast imaging using a shearing interferometer', *Appl. Phys. Lett.* **81**(17), 3287–3289.
- David, C., Weitkamp, T., Pfeiffer, F., Diaz, A., Bruder, J., Rohbeck, T., Groso, A., Bunk, O., Stampanoni, M. & Cloetens, P. (2007b), 'Hard x-ray phase imaging and tomography using a grating interferometer', *Spectrochim. Acta B* **62**, 626–630.
- Davis, T. J., Gao, D., Gureyev, T. E., Stevenson, A. W. & Wilkins, S. W. (1995), 'Phase-contrast imaging of weakly absorbing materials using hard x-rays', *Nature* **373**, 595–598.
- Engelhardt, M., Baumann, J., Schuster, M., Kottler, C., Pfeiffer, F., Bunk, O. & David, C. (2007), 'High-resolution differential phase contrast imaging using a magnifying projection geometry with a microfocus x-ray source', *Appl. Phys. Lett.* **90**, 224101.
- Engelhardt, M., Kottler, C., Bunk, O., David, C., Schroer, C., Baumann, J., Schuster, M. & Pfeiffer, F. (2008), 'The fractional talbot effect in differential x-ray phase-contrast imaging for extended and polychromatic x-ray sources', *Journal of Microscopy* **232**(1), 145–157.

- ESRF (2007), ‘www.esrf.eu/usersandscience/experiments/imaging/id19/’.
- Fowles, G. R. (1975), *Introduction to Modern Optics*, Dover Publications, Inc., New York.
- Hecht, E. (2002), *Optics*, Addison Wesley.
- Henke, B. L., Gullikson, E. M. & Davis, J. C. (1993), ‘X-ray interactions: photoabsorption, scattering, transmission, and reflection at $E=50\text{--}30000\text{ eV}$, $Z=1\text{--}92$ ’, *Atomic Data and Nuclear Data Tables* **54**, 181–342.
- Hounsfield, G. N. (1973), ‘Computerized transverse axial scanning (tomography): Part i. description of system’, *Br. J. Radiol.* **46**(552), 1016–1022.
- Huang, Z. & Ruth, R. D. (1998), ‘Laser-electron storage ring’, *Phys. Rev. Lett.* **80**(5), 976–979.
- Ingal, V. & Beliaevskaya, E. (1995), ‘X-ray plane-wave topography observation of the phase contrast from a non-crystalline object.’, *J. Phys. D Appl. Phys.* **28**, 2314–2317.
- Kak, A. C. & Slaney, M. (2001), *Principles of Computerized Tomographic Imaging*, Society for Industrial and Applied Mathematics.
- Kottler, C., David, C., Pfeiffer, F. & Bunk, O. (2007), ‘A two-directional approach for grating based differential phase contrast imaging using hard x-rays’, *Optics Express* **15**(3), 1175–1181.
- Loewen, R. J. (2003), *A Compact Light Source: Design and Technical Feasibility Study of a Laser-Electron Storage Ring X-ray Source*, SLAC-Report-632, Stanford University.
- Lohmann, A. W. & Silva, D. E. (1971), ‘An interferometer based on the talbot effect’, *Optics Communications* **2**(9), 413–415.
- Mack, H., Bienert, M., Haug, F., Straub, F. S., Freyberger, M. & Schleicher, W. P. (2002), ‘Wave packet dynamics and factorization of numbers’, *arXiv:quant-ph/0204040v1*.
- Momose, A. & Fukuda, J. (1995), ‘Phase-contrast radiographs of nonstained rat cerebellar specimen’, *Med. Phys.* **22**(4), 375–379.
- Momose, A., Kawamoto, S., Koyama, I., Hamaishi, Y., Takai, K. & Suzuki, Y. (2003a), ‘Demonstration of x-ray talbot interferometry’, *Jpn. J. Appl. Phys.* **42**, L866–L868.

- Momose, A., Takeda, T., Yoneyama, A., Koyama, I. & Itai, Y. (2001), 'Phase-contrast x-ray imaging using an x-ray interferometer for biological imaging', *Analytical sciences* **17**(supp.), i527–i530.
- Momose, A., Yashiro, W., Takeda, Y., Suzuki, Y. & Hattori, T. (2006), 'Phase tomography by x-ray talbot interferometry for biological imaging', *Jpn. J. Appl. Phys.* **45**(6A), 5254–5262.
- Murphy, D. B. (2001), *Fundamentals of Light Microscopy and Electronic Imaging*, Wiley, New York.
- Nesterets, Y. I. & Wilkins, S. W. (2008), 'Phase-contrast imaging using a scanning-double-grating configuration', *Opt Express* **16**(8), 5849–5867.
- Pfeiffer, F., Bech, M., Bunk, O., Donath, T., Henrich, B. & David, P. K. C. (2009), 'X-ray dark-field and phase-contrast imaging using a grating interferometer', *Journal of Applied Physics* **105**, 102006.
- Pfeiffer, F., Bech, M., Bunk, O., Kraft, P., Eikenberry, E. F., Brönnimann, C., Grünzweig, C. & David, C. (2008a), 'Hard-x-ray dark-field imaging using a grating interferometer', *Nat. Mater.* **7**, 134–137.
- Pfeiffer, F., Bunk, O., David, C., Bech, M., Duc, G. L., Bravin, A. & Cloetens, P. (2007), 'High-resolution brain tumor visualization using three-dimensional x-ray phase contrast tomography', *Phys. Med. Biol.* **52**, 6923–6930.
- Pfeiffer, F., Bunk, O., Kottler, C. & David, C. (2007a), 'Tomographic reconstruction of three-dimensional objects from hard x-ray differential phase contrast projection images', *Nucl. Instr. Meth. A* **580**, 925–928.
- Pfeiffer, F., Bunk, O., Schulze-Briese, C., Diaz, A., Weitkamp, T., David, C., van der Veen, J. F., Vartanyants, I. & Robinson, I. K. (2005), 'Shearing interferometer for quantifying the coherence of hard x-ray beams', *Phys. Rev. Lett.* **94**, 164801.
- Pfeiffer, F., David, C., Bunk, O., Donath, T., Bech, M., Duc, G. L., Bravin, A. & Cloetens, P. (2008b), 'Region-of-interest tomography for grating-based x-ray differential phase-contrast imaging', *Physical review letters* **101**(16), 168101.
- Pfeiffer, F., Kottler, C., Bunk, O. & David, C. (2007b), 'Hard x-ray phase tomography with low-brilliance sources', *Phys. Rev. Lett.* **98**, 108105.

- Pfeiffer, F., Weitkamp, T., Bunk, O. & David, C. (2006), 'Phase retrieval and differential phase-contrast imaging with low-brilliance x-ray sources', *Nat. Phys.* **2**, 258–261.
- Rayleigh, L. (1881), 'Experiments with and theory of diffraction gratings', *Phil. Mag.* **11**, 196.
- Snigirev, A., Snigireva, I., Kohn, V., Kuznetsov, S. & Schelokov, I. (1995), 'On the possibilities of x-ray phase contrast microimaging by coherent high-energy synchrotron radiation', *Rev. Sci. Instrum.* **66**(12), 5486–5492.
- Suleski, T. J. (1997), 'Generation of lohmann images from binary-phase talbot array illuminators', *Applied Optics* **36**(20), 4686–4691.
- Takeda, Y., Yashiro, W., Suzuki, Y. & Momose, A. (2007), 'X-ray phase microtomography by single transmission grating', *Synchrotron Radiation Instrumentation* **879**(AIP Conf. Proc.), 1361–1364.
- Talbot, H. F. (1836), 'Facts relating to optical science', *Phil. Mag.* **9**, 401.
- Weitkamp, T., David, C., Kottler, C., Bunk, O. & Pfeiffer, F. (2006), Tomography with grating interferometers at low-brilliance sources, in 'Developments in X-Ray Tomography V', Vol. 6318, Proc. SPIE, p. 631828.
- Weitkamp, T., Diaz, A., David, C., Pfeiffer, F., Stampanoni, M., Cloetens, P. & Ziegler, E. (2005), 'X-ray phase imaging with a grating interferometer', *Opt Express* **12**(16), 6296–6304.
- Wernick, M. N., Wirjadi, O., Chapman, D., Zhong, Z., Galatsanos, N. P., Yang, Y., Brankov, J. G., Oltulu, O., Anastasio, M. A. & Muehleman, C. (2003), 'Multiple-image radiography', *Physics in Medicine and Biology* **48**, 3875–3895.
- Wilkins, S. W., Gureyev, T. E., Gao, D., Pogany, A. & Stevenson, A. W. (1996), 'Phase-contrast imaging using polychromatic hard x-rays.', *Nature* **384**, 335–337.
- Zhong, Z., Thominson, W., Chapman, D. & Sayers, D. (2000), 'Implementation of diffraction-enhanced imaging experiments: at the nsls and aps', *Nucl. Instr. Meth. A* **450**, 556–567.

Publication I

Physics in Medicine and Biology (2007)

Franz Pfeiffer, Oliver Bunk, Christian David, **Martin Bech**, Geraldine Le Duc, Alberto Bravin and Peter Cloetens

High-resolution Brain Tumor Visualization using Three-dimensional X-ray Phase Contrast Tomography

Physics in Medicine and Biology 52 (2007) 6923–6930

High-resolution brain tumor visualization using three-dimensional x-ray phase contrast tomography

F Pfeiffer^{1,2}, O Bunk¹, C David¹, M Bech³, G Le Duc⁴, A Bravin⁴
and P Cloetens⁴

¹ Paul Scherrer Institut, CH-5232 Villigen PSI, Switzerland

² Ecole Polytechnique Fédérale de Lausanne, CH-1015 Lausanne, Switzerland

³ Niels Bohr Institute, University of Copenhagen, DK-2100 Copenhagen, Denmark

⁴ European Synchrotron Radiation Facility, B.P. 220, 38043 Grenoble Cedex, France

E-mail: franz.pfeiffer@psi.ch

Received 6 August 2007, in final form 15 October 2007

Published 8 November 2007

Online at stacks.iop.org/PMB/52/6923

Abstract

We report on significant advances and new results concerning a recently developed method for grating-based hard x-ray phase tomography. We demonstrate how the soft tissue sensitivity of the technique is increased and show *in vitro* tomographic images of a tumor bearing rat brain sample, without use of contrast agents. In particular, we observe that the brain tumor and the white and gray brain matter structure in a rat's cerebellum are clearly resolved. The results are potentially interesting from a clinical point of view, since a similar approach using three transmission gratings can be implemented with more readily available x-ray sources, such as standard x-ray tubes. Moreover, the results open the way to *in vivo* experiments in the near future.

(Some figures in this article are in colour only in the electronic version)

1. Introduction

Phase-sensitive x-ray imaging, which uses the phase shift rather than the absorption as the imaging signal has the potential of substantially increased contrast in biological samples (Fitzgerald 2000, Momose 2005). Various phase-sensitive x-ray imaging methods were developed in the past years. They can be classified into interferometric methods (Bonse and Hart 1965, Momose *et al* 2003, Weitkamp *et al* 2005), techniques using an analyzer (Davis *et al* 1995, Ingal and Beliaevskaya 1995, Chapman *et al* 1997), and free-space propagation methods (Snigirev *et al* 1995, Nugent *et al* 1996, Wilkins *et al* 1996). Some of the methods not only generate a form of phase contrast, but also provide quantitative phase information, which can be used for advanced image analysis. The extension to computed tomography (CT) is one such interesting possibility providing three-dimensional information about the specimen (Momose *et al* 1996, Beckmann *et al* 1997, Cloetens *et al* 1999, McMahon *et al* 2003, 2006, Groso *et al* 2006, Pfeiffer *et al* 2007a).

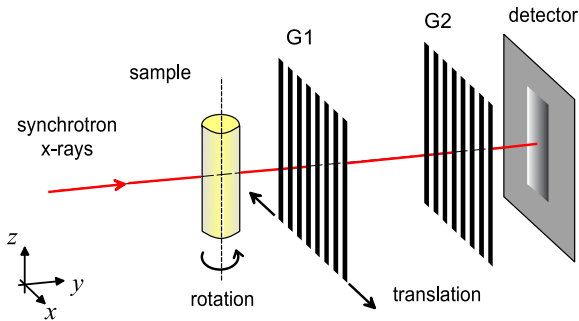


Figure 1. Schematic of the setup for x-ray phase tomography using a grating interferometer. For each projection a series of at least four images is recorded while one of the gratings (G1) is scanned along the x -direction.

In this paper we report on significant advances of a recently developed method for grating-based hard x-ray phase tomography (Weitkamp *et al* 2005, Momose *et al* 2006). More precisely, we describe the combination of three particular improvements concerning (i) the application of gratings with higher contrast made by a novel fabrication process, (ii) a high precision and high speed setup for the phase stepping procedure and (iii) the application of an improved tomographic phase reconstruction algorithm.

2. Materials and methods

2.1. Experimental setup

The principles of differential phase contrast imaging using a grating interferometer have been described in detail in Weitkamp *et al* (2005), Momose *et al* (2006), Pfeiffer *et al* (2006a), and are only briefly reviewed here. Figure 1 shows our experimental arrangement. It consists of the specimen on a rotation stage, a phase grating G1 and an analyzer absorption grating G2. The first grating (G1) acts as phase mask, and imprints periodic phase modulations onto the x-ray wave front. Through the Talbot effect, the phase modulation is transformed into an intensity modulation in the plane of the second grating (G2), forming a linear periodic fringe pattern perpendicular to the optical axis and parallel to the lines of G1 (Momose *et al* 2006, Weitkamp *et al* 2007). The second grating (G2) with absorbing lines and the same periodicity and orientation as the fringes created by G1 is placed in the detection plane, immediately in front of the detector. When one of the gratings is scanned along the transverse direction ('phase stepping'), the intensity signal in each pixel in the detector plane oscillates as a function of the grating position. The fundamental idea of the method is to analyze, for each pixel, the changes of these oscillations, when an object is placed into the x-ray beam. As described in more detail in Weitkamp *et al* (2005), Pfeiffer *et al* (2006a), a single phase-stepping scan (a series of at least four images taken at different positions of the scanned grating) yields both quantitative images of the specimen's phase shift gradient, $d\Phi(x, z)/dx$, and the conventional transmission projection.

Three-dimensional (3D) information of the specimen using computed tomography (CT) can be obtained, when the specimen is rotated around the rotation axis and a phase stepping series is recorded for each angle. The tomography data set can be reconstructed by integrating the pre-processed differential phase contrast projection images line by line and then performing

a standard tomographic reconstruction (Weitkamp *et al* 2005). A method that not only saves computing time but also generally yields better reconstructions is to directly reconstruct the 3D volume data set from the pre-processed differential phase contrast projections by using a modified filter kernel (Hilbert transform) in the FBP reconstruction (see Pfeiffer *et al* (2007a), (2007b), Faris and Byer (1988) for a more detailed description). The latter approach was used for the present study. The reconstructed quantity is the real part of the x-ray refractive index (as opposed to standard absorption-contrast tomography, where it is the absorption coefficient).

2.2. Image acquisition

The imaging experiments were carried out at the beamline ID19 while the tumor implantation was performed at the BioMedical Facility of the European Synchrotron Radiation Facility (ESRF, Grenoble). A monochromatic x-ray beam of 24.9 keV ($\lambda = 0.498 \text{ \AA}$) was used for the measurements. The interferometer was placed at a distance of 140 m from the wiggler source. The gratings were fabricated by a process involving photolithography, deep etching into silicon and electroplating of gold. The first grating (Si phase grating, G1) had a period of $p_1 = 3.99 \mu\text{m}$ and a height of $h_1 = 31.7 \mu\text{m}$. The corresponding values for the second grating (gold absorber grating, G2) were $p_2 = 2.00 \mu\text{m}$ and $h_2 = 30 \mu\text{m}$. In contrast to the earlier experiments (Weitkamp *et al* 2005), a novel grating fabrication protocol was used (David *et al* 2007). This allowed the fabrication of unprecedentedly high aspect ratios (60:1) for the absorbing lines of the analyzer grating (G2), thus increasing the contrast of the intensity modulation recorded during a phase-stepping scan. The field-of-view was matched to the size of the specimen (rat brain) and was $16.1 \times 16.1 \text{ mm}^2$. To achieve a very high angular, and thus phase sensitivity, the distance between G1 and G2 was chosen to be as large as 361 mm (ninth fractional Talbot distance (Weitkamp *et al* 2007)). The images were recorded using a $15 \mu\text{m}$ thick polycrystalline gadolinium oxysulfide scintillation screen with a magnifying optical lens system and a cooled charge coupled device (CCD). We used the FReLoN 2000 (a fast-readout, low-noise CCD developed at the ESRF) with 1024×1024 pixels and a $28.0 \times 28.0 \mu\text{m}^2$ pixel size (in the 2×2 binning mode). Due to the magnifying lens system, the effective pixel size in the recorded images was $15.7 \times 15.7 \mu\text{m}^2$.

For the acquisition of a full tomographic data set, the object was rotated around the tomographic rotation axis and images were recorded for each projection angle. To both increase the positioning accuracy of the grating during the phase stepping scan and to decrease the overhead time due to motor movements, a piezo-driven translation stage with an active feedback loop was used for this experiment. The latter consisted of a PI Hera piezo nano-positioning system (P-621.1CL) with the corresponding analog amplifier in a closed loop operation with a positioning accuracy of $< 10 \text{ nm}$. A detailed analysis (standard deviation) of the background regions in the differential phase contrast projection images showed that due to the high positioning accuracy of the piezo stage an angular sensitivity of $0.014 \mu\text{rad}$ could be obtained in the measured data. Furthermore, this configuration enabled us to acquire a whole data set of 721 projections, each consisting of eight images, within a total exposure time of less than 40 min (0.4 s exposure time per individual image). This proved to be of crucial importance to achieve a high sensitivity, because it suppresses artifacts in the data, which are otherwise unavoidable due to long term drifts or instabilities of the mechanical setup, the monochromator or the synchrotron beam itself. Note that the total exposure time can potentially be reduced to below 10 min for future *in vivo* experiments by reducing both the number of tomographic projections and the exposure time for each individual image by 50% without significantly compromising on the spatial resolution and sensitivity in the reconstructed 3D images.

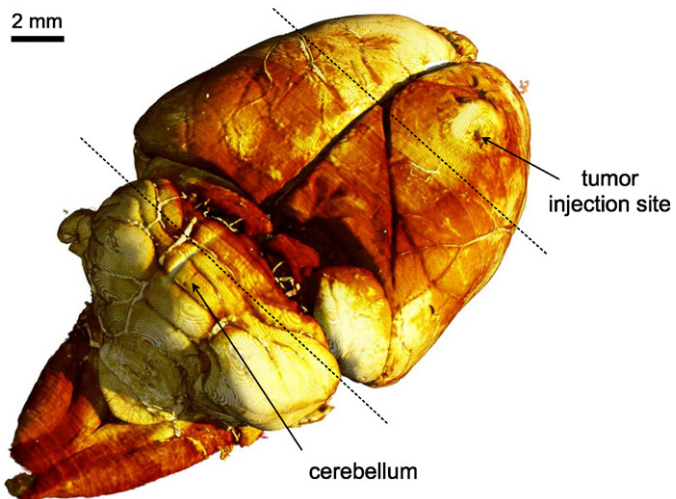


Figure 2. Post mortem three-dimensional image obtained on a rat brain bearing a 9 L gliosarcoma. The volume data set was reconstructed from 721 high sensitivity differential phase contrast projections measured at a synchrotron x-ray source.

2.3. Sample preparation

The rat brain specimen was prepared according to the following details.

Cell line: the 9 L gliosarcoma cell line (Coderre *et al* 1994) was established by (Benda *et al* 1971). Cells were grown as monolayers with Dulbecco's Modified Eagle Medium (DMEM) (Gibco-Invitrogen, France; Cergy-Pontoise, France) without sodium pyruvate (with 4500 mg l⁻¹ of glucose and pyridoxine HCl) supplemented with 10% fetal calf serum, 0.2% penicillin/streptomycin and incubated at 37 °C in a mixture of air-CO₂ (95%–5%).

Tumor implantation: the male Fisher 344 rats (180–280 g, Charles River, L' Arbresle, France) were placed on a stereotactic head holder (model 900, David Kopf Instruments, Tujunga, USA). The tumor cells were injected at D0 as described previously (Kobayashi *et al* 1980). Before injection in the brain, 10⁴ cells were suspended into 1 μl DMEM with antibiotics (1%) manually injected using a 1 μl Hamilton syringe through a burr hole in the right caudate nucleus (7.5 mm anterior to the ear bars, 3.5 mm lateral to the midline and 5.5 mm depth from the skull) (Paxinos and Watson 1986). The burr hole was plugged and the scalp sutured. All operative procedures related to animal care strictly conformed to the Guidelines of the French Government (licenses 380324/380456 and A3818510002) and were reviewed by the Comité d'Ethique Régional Rhône-Alpes.

3. Results and discussion

For an overview, figure 2 shows a three-dimensional rendering of the reconstructed volume data set. The reconstructed quantity that is displayed is the real part of the x-ray refractive index.

Figures 3 and 4 show slices through the specimen, revealing two interesting findings. The first observation, supported by what can be seen in the tomographic image slice through the brain region containing the rat's *cerebellum* (figure 3(a)), concerns the contrast between the brain's white and gray matter. Although such differentiation is usually hardly possible based

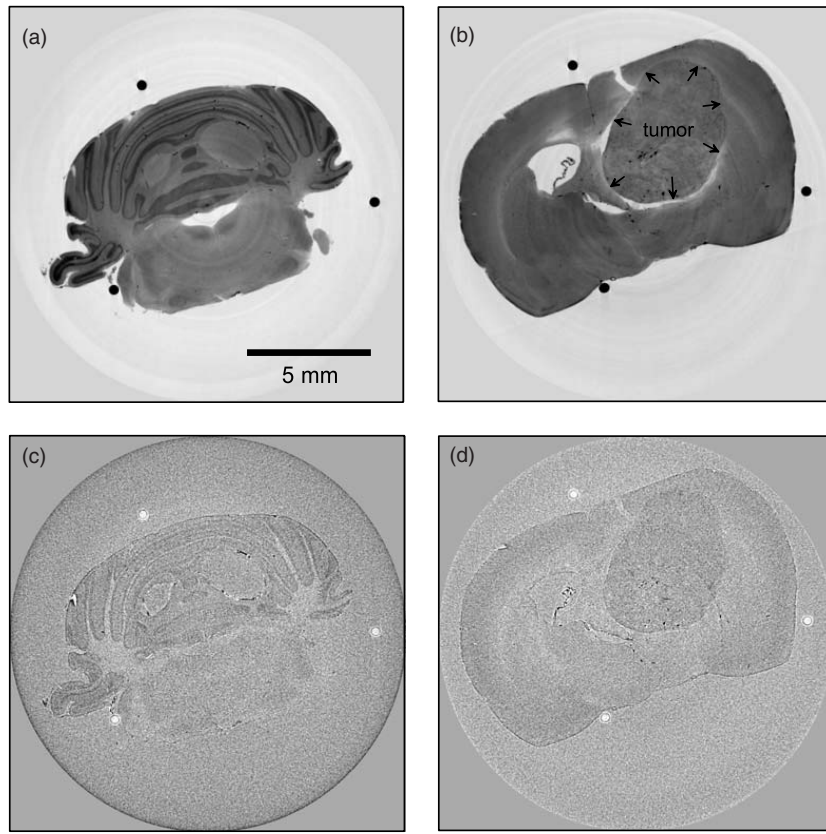


Figure 3. Phase and attenuation-based tomography results. (a) Phase tomography slice through the rat's cerebellum showing a clear contrast between the white and gray brain matter. (b) Slice through a region of the brain containing a tumor (arrows indicate the tumor's ‘pushing front’, the border between the tumor-invaded and healthy brain tissue). (c) and (d) Corresponding slices through the absorption-based reconstruction of the specimen. All images are displayed on a linear gray scale corresponding to $\pm 2\sigma$, where σ is the standard deviation of the pixel gray values in the image.

on x-ray CT scans, our method clearly resolves these small density differences in the brain tissue structure. Based on the standard deviation of the gray values in background (formalin) regions of the reconstructed tomographic slices, we deduce a measurement sensitivity for the real part of the refractive index of 2.0×10^{-10} . This corresponds to an electron density sensitivity of 0.18 e nm^{-3} and a mass density sensitivity of approximately 0.53 mg cm^{-3} for aqueous specimens. For comparison, a corresponding tomographic slice through the conventional absorption-based reconstruction is shown in figure 3(c). For the latter, we have averaged all frames recorded at each viewing angle to yield a non-interferometric projection image and used a standard absorption-based CT reconstruction protocol (Kak and Slaney 1987). Importantly, both results (figures 3(a) and (c)) have been obtained from the same data set, i.e., with the same exposure time.

The second observation, which confirms the enhanced tissue sensitivity of the method, is shown in figure 3(b). It displays a tomographic slice through a region in the brain which contains pathologic tissue, i.e. a brain tumor. Figure 3(b) shows clearly the presence of a 9 L gliosarcoma in the right caudate nucleus of the brain. Due to the presence of the tumor,

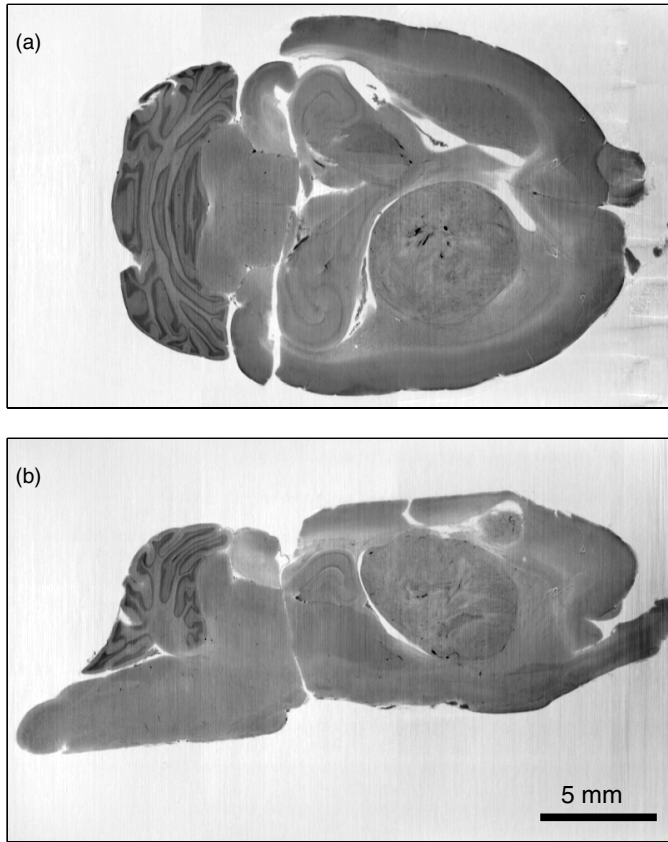


Figure 4. Additional slices through the phase tomography reconstruction: (a) frontal slice and (b) sagittal slice.

the midline is shifted and the left ventricle is dilated. The boundaries between the tumor and the healthy tissues are clearly defined. Moreover, the intra-tumoral heterogeneity can be seen with patches of various gray levels in the tumor itself. This probably corresponds to the presence of both necrotic and viable (with a high cellularity) areas as defined for that model (Henderson *et al* 1981). It has to be noted that our technique reveals the difference between corpus callosum and caudate nucleus.

Based on these results we conclude that both the differentiation of the white from the gray brain matter and details of the tumor invasion clearly demonstrate the potential of the method for biomedical studies, i.e. for high-resolution brain investigations. Since the spatial resolution of the presented results was mainly limited by the point spread function of the detection system, which typically is a factor of two larger than the effective pixel size, further improvements are easily possible in that respect. Increasing the resolution to a length scale corresponding to the second grating period ($2 \mu\text{m}$) is straightforward and can be achieved by changing the detector optics accordingly.

4. Summary

In summary, we have demonstrated how an improved grating-based phase contrast tomography setup yields images of biomedical specimens with unprecedented soft tissue sensitivity at

synchrotron x-ray sources. In particular we have shown that this x-ray method can be used to discern between subtle details of the tissue structure of animal brains, an application field which until now has almost exclusively been reserved for other, e.g. MRI, techniques. While the results can be applied immediately for biomedical studies at synchrotron x-ray sources, they are potentially interesting from a clinical point of view, since a similar approach can be implemented with more readily available x-ray sources, such as standard x-ray tubes (Pfeiffer *et al* 2007a, Pfeiffer *et al* 2006a).

Acknowledgments

We gratefully acknowledge J Bruder and C Grünzweig for the grating fabrication, C Kottler for help during the experiments and T Weitkamp for fruitful discussions. This work was supported by the European Synchrotron Radiation Facility (project MI-825) by allocation of beam time.

References

- Beckmann F, Bonse U, Busch F and Gunnewig O J 1997 X-ray microtomography (mu CT) using phase contrast for the investigation of organic matter *J. Comput. Assist. Tomogr.* **21** 539–53
- Benda P, Someda K, Messer J and Sweet W H 1971 Morphological and immunochemical studies of rat glial tumors and clonal strains propagated in culture *J. Neurosurg.* **34** 310–23
- Bonse U and Hart M 1965 An x-ray interferometer *Appl. Phys. Lett.* **6** 155–6
- Chapman L D, Thominson W C, Johnston R E, Washburn D, Pisano E, Gmuer N, Zhong Z, Menk R, Arfelli F and Sayers D 1997 Diffraction enhanced x-ray imaging *Phys. Med. Biol.* **42** 2015–25
- Cloetens P, Ludwig W, Baruchel J, van Dyck D, van Landuyt J, Guigay J P and Schlenker M 1999 Holotomography: quantitative phase tomography with micrometer resolution using hard synchrotron radiation x rays *Appl. Phys. Lett.* **75** 2912–4
- Coderre J A, Button T M, Micca P L, Fisher C D, Nawrocky M M and Liu H B 1994 Neutron-capture therapy of the 9 L rat gliosarcoma using the p-borophenylalanine-fructose complex *Int. J. Radiat. Oncol. Biol. Phys.* **30** 643–52
- David C, Bruder J, Rohbeck T, Grünzweig C, Kottler C, Diaz A, Bunk O and Pfeiffer F 2007 Fabrication of diffraction gratings for hard x-ray phase contrast imaging *Microelectron. Eng.* **84** 1172–7
- Davis T J, Gao D, Gureyev T E, Stevenson A W and Wilkins S W 1995 Phase-contrast imaging of weakly absorbing materials using hard x-rays *Nature* **373** 595–8
- Faris G W and Byer R L 1988 3-dimensional beam-deflection optical tomography of a supersonic jet *Appl. Opt.* **27** 5202–6
- Fitzgerald R 2000 Phase-sensitive x-ray imaging *Phys. Today* **53** 23–7
- Grosu A, Stampanoni M, Abela R, Schneider P, Linga S and Müller R 2006 Phase contrast tomography: an alternative approach *Appl. Phys. Lett.* **88** 214104
- Henderson S D, Kimler B F and Morantz R A 1981 Radiation-therapy of 9 L rat-brain tumors *Int. J. Radiat. Oncol. Biol. Phys.* **7** 497–502
- Ingal V N and Beliaevskaya E A 1995 X-ray plane wave topography observation of the phase contrast from a noncrystalline object *J. Phys. D* **28** 2314–7
- Kak A C and Slaney M 1987 *Principles of Computerized Tomography* (New York: IEEE Press)
- Kobayashi N, Allen N, Clendenon N R and Ko L W 1980 An improved rat-brain tumor model *J. Neurosurg.* **53** 808–15
- McMahon P J, Peele A G, Paterson D, Lin J J A, Irving T H K, McNulty I and Nugent K A 2003 Quantitative x-ray phase tomography with sub-micron resolution *Opt. Commun.* **217** 53–7
- Momose A 2005 Recent advances in x-ray phase imaging *Japan. J. Appl. Phys.* **44** 6355–9
- Momose A, Kawamoto S, Koyama I, Hamaishi Y, Takai K and Suzuki Y 2003 Demonstration of x-ray Talbot interferometry *Japan. J. Appl. Phys.* **42** 866–9
- Momose A, Takeda T, Itai Y and Hirano K 1996 Phase-contrast x-ray computed tomography for observing biological soft tissues *Nat. Med.* **2** 473–5
- Momose A, Yashiro W, Takeda Y, Suzuki Y and Hattori T 2006 Phase tomography by x-ray Talbot interferometry for biological imaging *Japan. J. Appl. Phys.* **45** 5254–62

- Paxinos G and Watson C (ed) 1986 *The Rat Brain in Stereotaxic Coordinates* (New York: Academic)
- Pfeiffer F, Grünzweig C, Bunk O, Frei G, Lehmann E and David C 2006a Neutron phase imaging and tomography *Phys. Rev. Lett.* **96** 215505
- Pfeiffer F, Kottler C, Bunk O and David C 2007a Hard x-ray phase tomography with low-brilliance sources *Phys. Rev. Lett.* **98** 108105
- Pfeiffer F, Kottler C, Bunk O and David C 2007b Tomographic reconstruction of three-dimensional objects from hard x-ray differential phase contrast projection images *Nucl. Instrum. Meth. Phys. Res. A* **580** 925–8
- Pfeiffer F, Weitkamp T, Bunk O and David C 2006b Phase retrieval and differential phase-contrast imaging with low-brilliance x-ray sources *Nat. Phys.* **2** 258–61
- Nugent K A, Gureyev T E, Cookson D F, Paganin D and Barnea Z 1996 *Phys. Rev. Lett.* **77** 2961–4
- Snigirev A, Snigireva I, Kohn V, Kuznetsov S and Schelokov I 1995 On the possibilities of x-ray phase contrast microimaging by coherent high-energy synchrotron radiation *Rev. Sci. Instrum.* **66** 5486–92
- Wilkins S W, Gureyev T E, Gao D, Pogany A and Stevenson A W 1996 Phase-contrast imaging using polychromatic hard x-rays *Nature* **384** 35–37
- Weitkamp T, David C, Kottler C, Bunk O and Pfeiffer F 2007 Tomography with grating interferometers at low-brilliance sources *Proc. SPIE* **6318** 28–31
- Weitkamp T, Diaz A, David C, Pfeiffer F, Stampaoni M, Cloetens P and Ziegler E 2005 X-ray phase imaging with a grating interferometer *Opt. Exp.* **13** 6296–304

Publication II

Nature Materials (2008)

Franz Pfeiffer, **Martin Bech**, Oliver Bunk, Phillip Kraft, Eric F. Eikenberry,
Christian Brönnimann, Christian Grünzweig and Christian David

Hard-X-ray Dark-field Imaging using a Grating Interferometer

Nature Materials 7 (2008) 134–137

LETTERS

Hard-X-ray dark-field imaging using a grating interferometer

F. PFEIFFER^{1,2*}, M. BECH³, O. BUNK¹, P. KRAFT¹, E. F. EIKENBERRY¹, CH. BRÖNNIMANN¹, C. GRÜNZWEIG¹ AND C. DAVID¹

¹Paul Scherrer Institut, CH-5232 Villigen PSI, Switzerland

²École Polytechnique Fédérale de Lausanne, CH-1015 Lausanne, Switzerland

³Niels Bohr Institute, University of Copenhagen, DK-2100 Copenhagen, Denmark

*e-mail: franz.pfeiffer@psi.ch

Published online: 13 January 2008; doi:10.1038/nmat2096

Imaging with visible light today uses numerous contrast mechanisms, including bright- and dark-field contrast, phase-contrast schemes and confocal and fluorescence-based methods¹. X-ray imaging, on the other hand, has only recently seen the development of an analogous variety of contrast modalities. Although X-ray phase-contrast imaging could successfully be implemented at a relatively early stage with several techniques^{2–11}, dark-field imaging, or more generally scattering-based imaging, with hard X-rays and good signal-to-noise ratio, in practice still remains a challenging task even at highly brilliant synchrotron sources^{12–18}. In this letter, we report a new approach on the basis of a grating interferometer that can efficiently yield dark-field scatter images of high quality, even with conventional X-ray tube sources. Because the image contrast is formed through the mechanism of small-angle scattering, it provides complementary and otherwise inaccessible structural information about the specimen at the micrometre and submicrometre length scale. Our approach is fully compatible with conventional transmission radiography and a recently developed hard-X-ray phase-contrast imaging scheme¹¹. Applications to X-ray medical imaging, industrial non-destructive testing and security screening are discussed.

Visible-light microscopy is a standard and widely used tool with a broad range of applications in science, industry and everyday life. Besides standard bright-field imaging, many more contrast mechanisms have been developed, and dark-field-imaging, phase-contrast, confocal and fluorescence microscopy are routine methods in today's light-microscopy applications¹. It is not surprising that this development has stimulated a similar progress in imaging applications with other forms of radiation. In electron microscopy, for example, where the first electron-microscope image was produced in the early 1930s, dark-field imaging was introduced in the late 1930s¹⁹, and imaging on the basis of phase contrast in the 1940s²⁰.

In X-ray microscopy, or more generally X-ray imaging, the development of a similar range of contrast modalities proceeded much more slowly and is still a very active field of research. Despite the early pioneering work on X-ray interferometry in the 1960s², the majority of phase-contrast imaging^{2–11} and dark-field imaging^{12–18} methods were introduced in the late 1990s. The development of such advanced imaging methods is particularly difficult for hard X-rays (with energies in the

multi-keV range), because of the lack of efficient X-ray optics. Existing hard-X-ray dark-field-imaging methods, for example, rely on the use of crystal optics that can accept only a very narrow energy bandwidth ($\approx 0.01\%$) and angular divergence^{3,15–18} (≈ 1 arcsec). This is why dark-field or scattering-based imaging is currently restricted in practice to applications at highly brilliant synchrotron X-ray sources^{14–18} and is not available for widespread applications that require a method applicable to standard X-ray tubes. In the following we describe a new approach, which helps overcome these restrictions and can produce high-quality X-ray dark-field scatter images using conventional X-ray tube sources.

Figure 1 shows our experimental arrangement. It consists of a source grating G0, a phase grating G1 and an analyser absorption grating G2 (Fig. 1a). The source grating (G0), typically placed close to the X-ray tube, is an aperture mask with transmitting slits. It creates an array of periodically repeating line sources and effectively enables the use of relatively large, that is, square-millimetre-sized, X-ray sources, without compromising the coherence requirements of the arrangement formed by G1 and G2 (ref. 11). The image contrast itself is formed via the combined effect of the two gratings G1 and G2. The second grating (G1) acts as a phase mask, and imprints periodic phase modulations onto the incoming wave field. Through the Talbot effect^{21–24}, the phase modulation is transformed into an intensity modulation in the plane of G2, forming a linear periodic fringe pattern perpendicular to the optical axis and parallel to the lines of G1 (Fig. 1b). The third grating (G2), with absorbing lines and the same periodicity and orientation as the fringes created by G1, is placed in the detection plane, immediately in front of the detector. When one of the gratings is scanned along the transverse direction x_g , the intensity signal $I(m, n)$ in each pixel (m, n) in the detector plane oscillates as a function of x_g (Fig. 1c).

The fundamental idea of the method presented here is to evaluate the local changes of the oscillation $I(m, n, x_g)$ induced by an object and determine from these several imaging signals, including the dark-field contrast. To analyse these changes quantitatively, we write the intensity oscillation for each detector pixel in a Fourier series

$$I(m, n, x_g) = \sum_i a_i(m, n) \cos(ikx_g + \phi_i(m, n)) \\ \approx a_0(m, n) + a_1(m, n) \cos(kx_g + \phi_1(m, n)), \quad (1)$$

nature materials | VOL 7 | FEBRUARY 2008 | www.nature.com/naturematerials

where a_i are the amplitude coefficients, ϕ_i the corresponding phase coefficients, $k = 2\pi/p_2$ and p_2 is the period of G2. Then the normalized average transmission of the specimen in each detector pixel is given by $T(m, n) = a_0^s(m, n)/a_0^r(m, n)$, where the superscripts s and r denote the values measured with the specimen in place (s) and as a reference without (r). Note that $T(m, n)$ is identical to what would be measured with a conventional X-ray radiography set-up. Furthermore, we have previously shown¹¹ that differential phase-contrast images can be obtained by analysing the lateral shift of intensity modulation, that is, the quantity $\phi_1(m, n)$ in equation (1).

The new aspect and particular focus of the work presented here is how dark-field images, or more generally images on the basis of the local scattering power of the sample, can be obtained with such a set-up. In terms of visible-light Fourier optics, dark-field illumination removes the zeroth order (unscattered light) from the diffraction pattern formed at the rear focal plane of the objective. This results in an image formed exclusively from higher-angle diffraction intensities scattered by the specimen. Quite similarly, information about the scattering power of the specimen is contained in our case in the higher order, that is, the first Fourier component of $I(m, n, x_g)$. More precisely, the amplitude of the first Fourier component, a_1 , is decreased when X-rays are scattered or reflected at internal inhomogeneities or interfaces on their passage through the specimen (Fig. 1b).

For a quantitative description of this effect, we first define the normalized oscillation amplitude, the visibility of the intensity modulation of $I(m, n, x_g)$, by the ratio $V^r(m, n) \equiv (I_{\max} - I_{\min})/(I_{\max} + I_{\min}) = a_1^r(m, n)/a_0^r(m, n)$; see equation (1). The relative decrease of the visibility due to the specimen can be quantified by defining the normalized visibility, $V(m, n) \equiv V^s(m, n)/V^r(m, n)$. For homogeneous specimens, that is, for samples with negligible small-angle X-ray scattering contribution, the value for the visibility remains unchanged, and $V(m, n) = 1$. However, specimens that, for example, show strong internal density fluctuations on micrometre length scales, and thus produce a strong small-angle X-ray scattering signal, show a significant decrease of the visibility and yield values of $V < 1$ (ref. 23). More generally, we note that the quantity $V(m, n)$ is inversely proportional to the effective integrated local small- (and ultrasmall-) angle scattering power of the sample and therefore refer to it as a 'dark-field' image of the specimen. Most simply, this can be understood by considering that the amplitude of the oscillations in $I(m, n, x_g)$ is most effectively reduced by X-rays scattered from the object at wavevectors corresponding to diffraction angles defined by the ratio of half the period of G2 over the distance between the object and G2 (see also Fig. 1b).

Figure 2 shows the experimental results obtained for a test sample made out of a Teflon plastic tube and a natural rubber tube. The conventional transmission image is shown in Fig. 2a, the novel dark-field image in Fig. 2b and the differential phase-contrast image in Fig. 2c (ref. 11). Whereas the inner part of the two tubes looks very similar in the transmission image (Fig. 2a) and the differential phase-contrast image (Fig. 2c), clear differences are visible in the dark-field image (Fig. 2b). The microscopic density fluctuations (pore structure) in the rubber tube produce a strong small-angle scattering signal and thus significantly smaller intensity modulations (Fig. 2d) in $I(m, n, x_g)$ and correspondingly low values in the dark-field image (Fig. 2b). The inner parts of the Teflon tube, on the other hand, show no significant contributions to the dark-field signal, because the plastic is a homogenous material with essentially no density fluctuations on the relevant length scales. However, at the interfaces of the Teflon tube, small-angle reflections reveal more structural details. Both the dark-field image (Fig. 2b) and the differential phase-contrast image show (Fig. 2c),

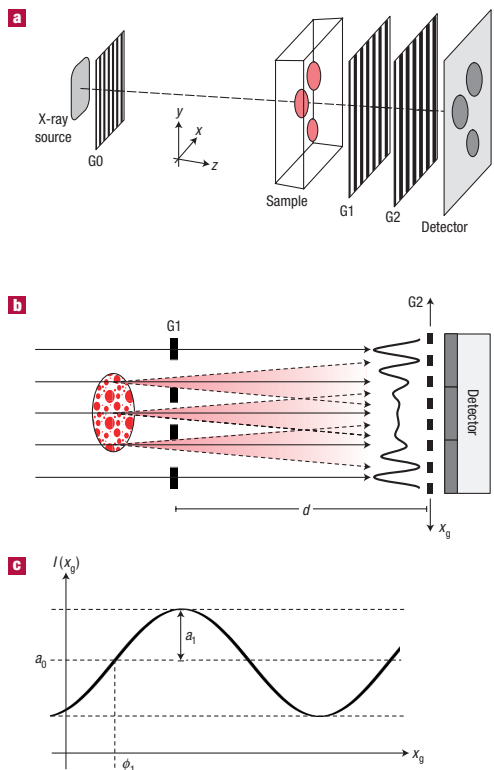


Figure 1 X-ray grating interferometer. **a**, Set-up with a source grating G0, a phase grating G1 and an analyser absorption grating G2. **b**, Through the Talbot effect a linear periodic fringe pattern is created behind G1 in the plane of G2. **c**, Intensity modulation detected in a detector pixel when one of the gratings is scanned along x_g . A loss in the amplitude of the oscillation due to the scattering of X-rays in the specimen (degradation of the coherent wavefront) can be used to extract images with dark-field contrast.

more clearly than the absorption image (Fig. 2a), that the thick walls of the Teflon tube were actually made by inserting a thinner tube into a tube with a larger diameter.

More generally, the small-angle scattering signal as recorded in the dark-field image is particularly sensitive to density variations in the object on the length scale of a few tenths of nanometres to several micrometres. It naturally complements the length scales that can be imaged directly by radiographic methods into the submicrometre range.

Although we have applied our method to obtain dark-field images of numerous specimens, proving the method to be of potential interest for a broad range of applications, we can report here on only one in detail (a second is in the Supplementary Information, Fig. S2). This example is shown in Fig. 3 and particularly demonstrates the potential for improved contrast in medical imaging. As a biological test specimen, a chicken wing was used. The conventional transmission contrast is shown in Fig. 3a and the dark-field contrast in Fig. 3b. Note that, because both

LETTERS

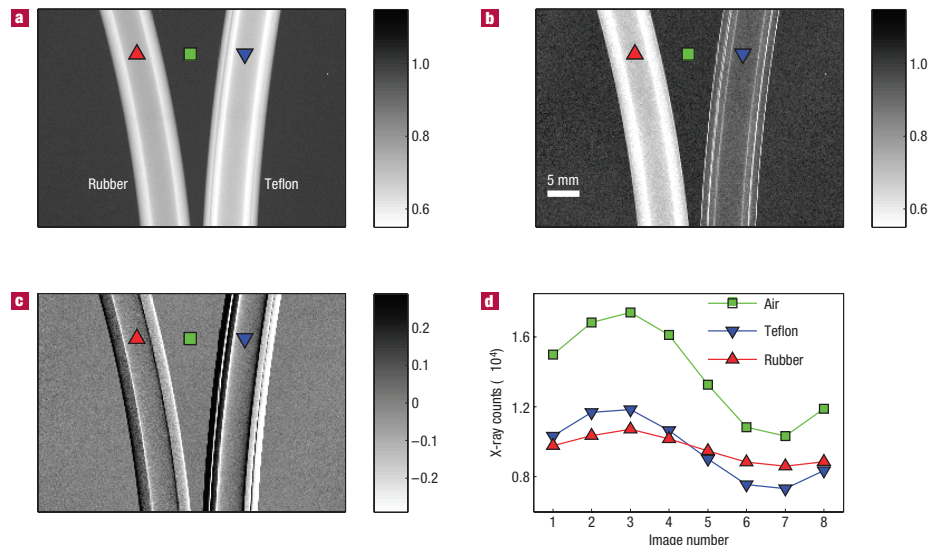


Figure 2 X-ray imaging of a test sample consisting of a PTFE (Teflon) plastic tube and a natural rubber tube. **a**, Conventional X-ray transmission image (normalized to the empty beam). **b**, Dark-field image of the same sample (normalized visibility, see text). **c**, Differential phase-contrast image. All images are shown on a linear grey scale. **d**, Intensity oscillations for three detector pixels extracted from a series of eight images taken at different values of x_i . Clearly visible is the loss of fringe visibility in the detector pixel behind the natural rubber tube due to the strong small-angle scattering produced by microscopic density fluctuations (pore structure). The total exposure time for the whole data set was 40 s.

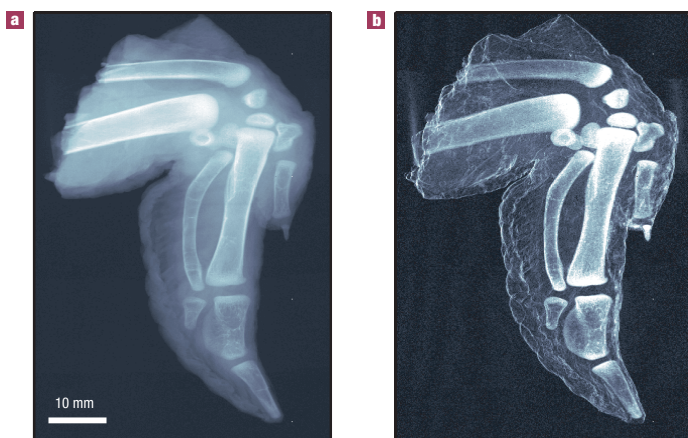


Figure 3 Imaging of a biological specimen (chicken wing). **a**, Conventional transmission image. **b**, Dark-field image. The X-ray scattering due to the porous microstructure of the bones and the reflection at internal or external interfaces produce a strong signal in the dark-field image. The total exposure time to obtain the whole data set, from which the images were processed, was 40 s. Both images are shown on a linear grey scale corresponding to four times the standard deviation of the range of pixel grey-scale values.

images were obtained from the same data set, the radiation dose was identical in both cases.

In agreement with what was observed in the images of the tube sample (Fig. 2), we find that also in this biological specimen the

boundaries and interfaces produce a strong signal in the dark-field image (see Fig. 3b). Furthermore, we observe that the chicken bones obviously consist of a highly porous and strongly scattering microstructure, because they are clearly visible in the dark-field

contrast (Fig. 3b). However, it is surprising that the differences in the grey-scale values of the bone and the tissue are significantly different in Fig. 3a and b. Although the soft tissue provides a still well-defined signal in the transmission image, the scattering of the tissue is obviously too weak to produce a significant contribution to the dark-field image contrast. We conclude that, although bones are generally already well represented in the transmission images, dark-field imaging can potentially yield a complementary and even enhanced contrast^{17,18}. For example, in cases of complicated bone fractures, where small splinters can intrude into the surrounding tissue, dark-field contrast could provide the necessary specificity to visualize subtle details.

In summary, we have shown how a grating interferometer can be used to produce dark-field images with hard X-rays. We have demonstrated that, in contrast to existing crystal-analyser-based methods^{15–17}, our method can efficiently be implemented with a standard X-ray tube source. The approach is potentially interesting for a wide range of applications including medical imaging¹⁸, security screening¹⁹ (see Supplementary Information, Fig. S2), industrial non-destructive testing²⁰, food inspection and small-animal imaging. In future, a further increase in the sensitivity of the method could also provide contrast between healthy and diseased breast tissue, because breast tumours show a different small-angle scattering signature than the healthy adipose matrix^{27,28}. Generally, we believe that the method is of particular interest for challenging X-ray imaging applications, because it simultaneously provides dark-field, transmission and differential phase contrast, thus providing maximum information about the specimen (see Supplementary Information, Fig. S1). Finally, this approach can be extended into three dimensions using computer tomographic techniques, coupled with a synchrotron source to yield micrometre-resolution hard-X-ray dark-field images, or implemented with other types of radiation, such as neutrons.

METHODS

The experiments were carried out on a Seifert ID 3000 X-ray generator operated at 40 kV/30 mA. We used a tungsten (W) line focus tube (DX-W8 × 0.4-L) with a focus size of 8 (horizontal) × 0.4 (vertical) mm². Owing to the inclination of the target with respect to the optical axis of 6°, the effective source size was 0.8 (h) × 0.4 (v) mm².

The gratings were fabricated by a process involving photolithography, deep etching into silicon and electroplating of gold²⁹. The size of the active area was limited in the present study by the processing technology (100 mm wafers) to 64 × 64 mm². No principle constraints hinder the upscaling of the method to larger areas. The gratings had periods of $p_0 = 73 \mu\text{m}$, $p_1 = 3.9 \mu\text{m}$ and $p_2 = 2.0 \mu\text{m}$. The heights of the grating structures, which were optimized for a mean X-ray energy of 28 keV, were 42 μm (G0), 35 μm (G1) and 26 μm (G2). The distance between G0 and G1 was 1.57 m and that between G1 and G2 43 mm, corresponding to the first fractional Talbot distance²⁴.

The images were recorded using a PILATUS 100K pixel detector³⁰. The module consists of an array of 487 × 195 pixels, with a pixel size of 0.172 × 0.172 mm². For the results shown in Fig. 3, three images were stacked on top of one another to increase the field of view in the vertical direction. The quantum detection efficiency is determined by the probability of absorbing an X-ray in the 320-μm-thick Si sensor and is ≈10% (at 28 keV). For the results shown in Figs 2 and 3, a series of eight individual images with exposure times of 5 s each was recorded. We believe that the exposure time can be reduced by at least by a factor of 60 by (1) using a rotating-anode X-ray generator with a power of a ≥10 kW, instead of the current 1 kW (a factor of 10), (2) increasing the detector efficiency from currently 10% to 30% using a thicker sensor (a factor of three) and (3) decreasing the distance between the source and the sample (a factor of two).

The two polytetrafluoroethylene (PTFE, Teflon) plastic tubes used in the experiment had a density of $\rho_{\text{PTFE}} = 2.2 \text{ g cm}^{-3}$ and a radius of $R_1 = 4.0 \text{ mm}$

with a hollow core of $r_1 = 3.0 \text{ mm}$ and $R_2 = 3.0 \text{ mm}$ with $r_2 = 2.0 \text{ mm}$, respectively. The natural rubber tube had a density of $\rho_{\text{rubber}} \approx 1.13 \text{ g cm}^{-3}$ and a radius of $R = 4.0 \text{ mm}$ with a hollow core of $r = 2.0 \text{ mm}$.

To extract the dark-field, phase and absorption contrast signals from the measured intensity modulation $I(m, n, x_g)$, one-dimensional discrete fast Fourier transforms were computed for each pixel. The resulting values for the Fourier coefficients were normalized to the corresponding values obtained without the specimen in place. On a standard personal computer (1.7 GHz processor, 2 GB memory), the processing time needed for a series of eight images with 10^5 pixels was of the order of a few seconds.

Received 18 September 2007; accepted 26 November 2007; published 13 January 2008.

References

1. Murphy, D. B. *Fundamentals of Light Microscopy and Electronic Imaging* (Wiley, New York, 2001).
2. Bonse, U. & Hart, M. An X-ray interferometer with long separated interfering beam paths. *Appl. Phys. Lett.* **6**, 155–156 (1965).
3. Davis, T. J., Gao, D., Gureyev, T. E., Stevenson, A. W. & Wilkins, A. W. Phase-contrast imaging of weakly absorbing materials using hard X-rays. *Nature* **373**, 595–598 (1995).
4. Ingall, V. N. & Beliaevskaya, E. A. X-ray plane-wave topography observation of the phase contrast from non-crystalline objects. *J. Phys. D* **28**, 2314–2317 (1995).
5. Chapman, D. et al. Diffraction enhanced x-ray imaging. *Phys. Med. Biol.* **42**, 2015–2025 (1997).
6. Snigirev, A., Snigireva, I., Kohn, V., Kuznetsov, S. & Schelokov, I. On the possibilities of X-ray phase contrast microimaging by coherent high-energy synchrotron radiation. *Rev. Sci. Instrum.* **66**, 5486–5492 (1995).
7. Wilkins, S. W., Gureyev, T. E., Gao, D., Pogany, A. & Stevenson, A. W. Phase-contrast imaging using polychromatic hard X-rays. *Nature* **384**, 335–337 (1996).
8. Momose, A. Recent advances in X-ray phase imaging. *Japan. J. Appl. Phys.* **44**, 6355–6267 (2005).
9. Momose, A., Yoshiro, W., Takeda, Y., Suzuki, Y. & Hattori, T. Phase tomography by X-ray Talbot interferometry for biological imaging. *Japan. J. Appl. Phys.* **45**, 5254–5262 (2006).
10. Weitkamp, T. et al. Quantitative X-ray phase imaging with a grating interferometer. *Opt. Express* **13**, 6296–6304 (2005).
11. Pfeiffer, F., Weitkamp, T., Bunk, O. & David, C. Phase retrieval and differential phase-contrast imaging with low-brilliance X-ray sources. *Nature Phys.* **2**, 258–261 (2006).
12. Morrison, G. R. & Browne, M. T. Dark-field imaging with the scanning-transmission X-ray microscope. *Rev. Sci. Instrum.* **63**, 611–614 (1992).
13. Chapman, H. N., Jacobsen, C. & Williams, S. A characterisation of dark-field imaging of colloidal gold labels in a scanning transmission X-ray microscope. *Ultramicroscopy* **62**, 191–213 (1996).
14. Suzuki, Y. & Uchida, F. Dark-field imaging in hard X-ray scanning microscopy. *Rev. Sci. Instrum.* **66**, 1468–1470 (1995).
15. Pagot, E. et al. A method to extract quantitative information in analyzer-based X-ray phase contrast imaging. *Appl. Phys. Lett.* **82**, 3421–3423 (2003).
16. Levine, L. E. & Long, G. G. X-ray imaging with ultra-small-angle X-ray scattering as a contrast mechanism. *J. Appl. Cryst.* **37**, 757–765 (2004).
17. Ando, M. et al. Clinical step onward with X-ray dark-field imaging and perspective view of medical applications of synchrotron radiation in Japan. *Nucl. Instrum. Methods A* **548**, 1–16 (2005).
18. Shima, D., Sugiyama, H., Kunisada, S. & Ando, M. Articular cartilage depicted at optimized angular position of Laue angular analyzer by X-ray dark-field imaging. *Appl. Radiat. Isot.* **64**, 868–874 (2006).
19. von Ardenne, H. M. *Das Elektronen-Rastermikroskop*. Z. Tech. Phys. **19**, 407–416; Z. Phys. **109**, 553–572 (1938).
20. Ramberg, E. G. Phase contrast in electron microscope images. *J. Appl. Phys.* **20**, 441–444 (1949).
21. Lohmann, A. W. & Silva, D. E. An interferometer based on the Talbot effect. *Opt. Commun.* **2**, 413–415 (1971).
22. Yokozaki, S. & Suzuki, T. Shearing interferometer using grating as beam splitter. *Appl. Opt.* **10**, 1575–1579 (1971).
23. Pfeiffer, F. et al. Shearing interferometer for quantifying the coherence of hard X-ray beams. *Phys. Rev. Lett.* **94**, 164801 (2005).
24. Weitkamp, T., David, C., Kottler, C., Bunk, O. & Pfeiffer, F. Tomography with grating interferometers at low-brilliance sources. *SPIE Int. Soc. Opt. Eng.* **6318**, 28–32 (2006).
25. Harding, G. X-ray scatter tomography for explosives detection. *Radiat. Phys. Chem.* **71**, 869–881 (2004).
26. Harding, G. & Schreiber, B. Coherent X-ray scatter imaging and its applications in biomedical science and industry. *Radiat. Phys. Chem.* **56**, 229–245 (1999).
27. Fernandez, M. et al. Small-angle X-ray scattering studies of human breast tissue samples. *Phys. Med. Biol.* **47**, 577–592 (2002).
28. Fernandez, M. et al. Human breast cancer in vitro: Matching histo-pathology with small-angle X-ray scattering and diffraction enhanced X-ray imaging. *Phys. Med. Biol.* **50**, 2991–3006 (2005).
29. David, C. et al. Fabrication of diffraction gratings for hard X-ray phase contrast imaging. *Microelectron. Eng.* **84**, 1172–1177 (2007).
30. Bech, M. et al. X-Ray imaging with the PILATUS 100K detector. *Appl. Radiat. Isot.* (2007, in press) (doi:10.1016/j.apradiso.2007.10.003).

Acknowledgements

We gratefully acknowledge C. Kottler for help with the experiments and T. Weitkamp and S. Wilkins for discussions.

Correspondence and requests for materials should be addressed to F.P.

Supplementary Information accompanies this paper on www.nature.com/naturematerials.

Author contributions

F.P., M.B. and C.D. conceived the experimental set up. C.D. and C.G. designed and fabricated the gratings. O.B. interfaced the experimental hardware and data acquisition system. F.P. wrote the data analysis software. C.B., E.F.E. and P.K. were responsible for the detector hardware, software and calibration. F.P. and M.B. analysed and interpreted the data.

Reprints and permission information is available online at <http://npg.nature.com/reprintsandpermissions/>

SUPPLEMENTARY INFORMATION - PFEIFFER ET AL.

I. Comparison of transmission, dark-field, and differential phase contrast images for the specimen shown in Fig. 3 of the manuscript

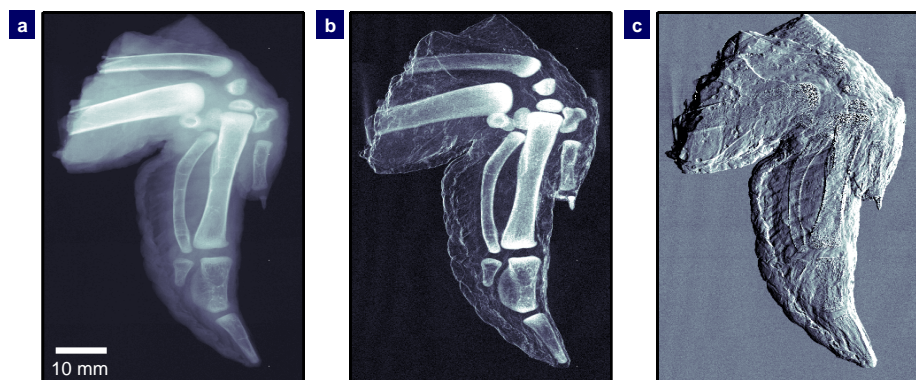


FIG. S1: Imaging of a biological specimen (chicken wing). (As Fig. 3, but with the addition of the differential phase contrast image.) (a) Conventional x-ray transmission image (normalized to the empty beam). (b) Dark-field image of the same sample (normalized visibility, see text). (c) Differential phase contrast image, obtained simultaneously with the images displayed in (a) and (b).

II. Application example for security screening

Using currently existing x-ray inspection systems, it can be very difficult, if not impossible, to discern explosives from harmless materials such as food products. Several types of cheese or chocolate, for example, have almost the same absorption cross sections for hard x-rays as plastic explosives, such as PETN (pentaerythritol tetranitrate) or Semtex (cyclotrimethylenetrinitramine & pentaerythritol tetranitrate). Quite unexpectedly, we observed that the presented dark-field imaging method evidenced to be a helpful tool in this respect. Because of the differences in the microstructure of the materials and the correspondingly different signatures in the scattering behavior, a distinction between the food product and the explosives becomes possible on the basis of the dark-field image.

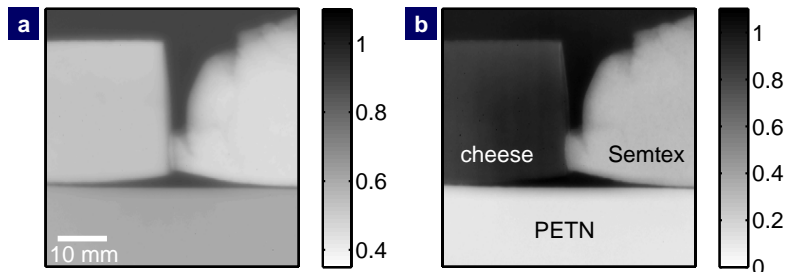


FIG. S2: Results for a test sample containing explosives (PETN, Semtex) and a food product (cheese). (a) Conventional x-ray transmission image. (b) Dark-field image. While a differentiation of the explosives from the food product is impossible on the basis of the transmission image alone, a clear difference is seen in the dark-field image. A granular microstructure, which is present in the explosives, causes strong small-angle scattering and the corresponding signal in the dark-field image.

Figure 2S, for example, shows results obtained for a test sample containing explosives (PETN, Semtex) and a food product (young Swiss cheese, type *Gruyère*). We observe that the granular microstructure which is present in the explosives, causes strong small-angle scattering and the corresponding signal in the dark-field image. The homogeneous density distribution in cheese, on the other hand, does not yield significant amounts of scattering and can thus be used to discern the two classes of materials in this case.

Publication III

Applied Radiation and Isotopes (2008)

Martin Bech, Oliver Bunk, Christian David, Phillip Kraft, Christian Brönnimann, Eric F. Eikenberry and Franz Pfeiffer

X-ray Imaging with the PILATUS 100k Detector

Applied Radiation and Isotopes 66 (2008) 474–478

X-Ray Imaging with the PILATUS 100K Detector

M. Bech,¹ O. Bunk,² C. David,² C. Brönnimann,² E. F. Eikenberry,² and F. Pfeiffer^{2,*}

¹*Niels Bohr Institute, University of Copenhagen, DK-2100 Copenhagen, Denmark*

²*Paul Scherrer Institut, CH-5232 Villigen PSI, Switzerland*

(Dated: March 7, 2007)

Abstract

We report on the application of the PILATUS 100K pixel detector for medical imaging. Experimental results are presented in the form of x-ray radiographs using standard x-ray absorption contrast and a recently developed phase contrast imaging method. The results obtained with the PILATUS detector are compared to results obtained with a conventional x-ray imaging system consisting of a x-ray scintillation screen, lens optics and a charge coupled device. Finally the results for both systems are discussed more quantitatively based on an image power spectrum analysis.

PACS numbers:

*To whom correspondence should be addressed; e-mail: franz.pfeiffer@psi.ch

I. INTRODUCTION

The penetrating power of x-rays has been used to reveal hidden inner structures non-destructively since the discovery of x-rays by Röntgen in 1895. X-ray imaging is nowadays indispensable in a variety of fields, including medicine and industry. Image quality is particularly important when further quantitative data processing is the subject of interest, as is the case in tomographic reconstruction of three dimensional objects based on measurements of a series of two dimensional projections. Modern digital imaging systems presently used in medical or industrial applications typically consist of combined devices, which first convert the x-rays into visible light and then detect the visible light photons by charge coupled devices (CCDs) or complementary metal oxide semiconductor (CMOS) sensors. Amorphous silicon flat panel detectors can be used either to detect visible light or electrons produced by the photoelectric effect in a suitable convertor. A third class of detector that is widely used is the storage phosphor, which stores part of the incident x-ray energy and releases it later when the phosphor sheet is scanned.

A direct consequence of such an indirect detection scheme is, however, that the image quality can be degraded by several sources of noise from all components of the imaging system. In the case of CCDs, for example, the image quality can be degraded due to the presence of a remaining dark current or shot noise in the read out, and by the point spread function (PSF) of the phosphor and of the optics. Direct detection of the individual x-rays can avoid these sources of image noise and can, in principle, reduce the error in each detector pixel to the theoretical limit given by the Poisson counting statistics for the x-ray photons detected in each individual pixel.

Here we report on a first evaluation of the direct detection PILATUS pixel detector for x-ray imaging purposes. We evaluate the performance of the system for conventional x-ray absorption contrast radiography and a recently developed phase contrast radiography scheme [1]. In order to directly compare the performance of the PILATUS pixel detector to a conventional imaging system, we have recorded images for the same test sample under identical experimental conditions both with the Pilatus detector and a CCD based imaging system.

II. EXPERIMENTAL

In the following the two detection systems and the x-ray generator setup are briefly described.

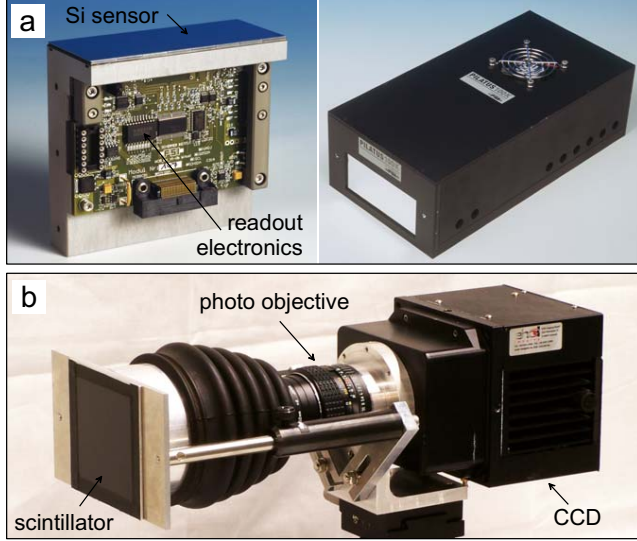


FIG. 1: (a) The PILATUS 100K module and the detector box. (b) CCD imaging system consisting of a scintillator, a photo objective, and a cooled CCD.

A. PILATUS pixel detector

The PILATUS detector is a novel single-photon counting pixel detector that was developed for x-ray diffraction experiments at the Paul Scherrer Institut [2, 3, 4], see Fig. 1a. We used a PILATUS 100K module which consists of an array of 487 x 195 pixels, with a pixel size of $0.172 \times 0.172 \text{ mm}^2$. Each pixel is operated in single-photon-counting mode, i.e. only x-rays above a certain threshold energy are counted. The pixels feature 20-bit counters, i.e. up to 10^6 photons can be counted in a pixel per exposure. The outstanding features of the detector are: (i) no dark current or read-out noise leading to an excellent signal-to-noise ratio, (ii) short readout time of 2.59 ms, (iii) electronic gating, i.e. synchronization of the

exposure with an external trigger is easily performed, and (iv) very simple operation at room temperature. The detector was operated with its threshold set to 17 keV which is significantly below the mean x-ray energy of 28 keV used in the measurements. The quantum detection efficiency is determined by the probability of absorbing an x-ray in the 320 μm thick Si sensor and is $\approx 10\%$ (at 28 keV).

B. CCD based x-ray imaging system

The CCD based x-ray imaging system, which was used as a conventional x-ray imaging reference system, consists of a 150 μm thick Cesium Iodide (CsI) scintillation screen [5] with a demagnifying ($M = 1 : 2.53$) optical lens system [6] and a cooled charge coupled device [7], see Fig. 1b. The theoretical resolution of the imaging system is determined by the CCD pixel size (24 \times 24 μm^2) corrected for the demagnification factor to $\approx 61 \times 61 \mu\text{m}^2$. In practice this theoretical pixel size is enlarged due to the influence of several effects, e.g. a blurring due to the thickness of the scintillation screen, the intrinsic width of the point spread function of the CCD, and the limited optical resolution of the lens system.

C. Experimental setup

The experiments were carried out on a Seifert ID 3000 x-ray generator operated at 40 kV/ 25 mA. We used a tungsten (W) line focus tube (DX-W8 \times 0.4-L) with a focus size of 8 \times 0.4 mm 2 . Due to the inclination of the target with respect to the optical axis of our setup of 6°, the effective source size was 0.8 \times 0.4 mm 2 . The sample was placed between the x-ray source and the detector. Since the distance between the sample and the source was much larger (≈ 1.6 m) than the distance between the sample and the detector (≈ 60 mm), blurring of the image due to the source size was negligible in our case.

III. RESULTS

Figure 2 shows measured absorption contrast images for a test sample (chicken wing) obtained with the PILATUS detector (Fig. 2a) and the CCD based imaging system (Fig. 2b). Importantly, both results were obtained using the identical experimental parameters,

i.e. the same exposure times, x-ray tube acceleration voltage settings, and filters. The images have been corrected using a flat-field image (an exposure without the sample in the beam). In the case of the CCD an additional correction using a dark-field (an exposure with the x-ray generator switched off) has been applied to correct for the dark current and the offset of the analogue to digital converter (ADC). For the pixel detector, the dark-field correction is not required, since this system does not produce any dark counts.

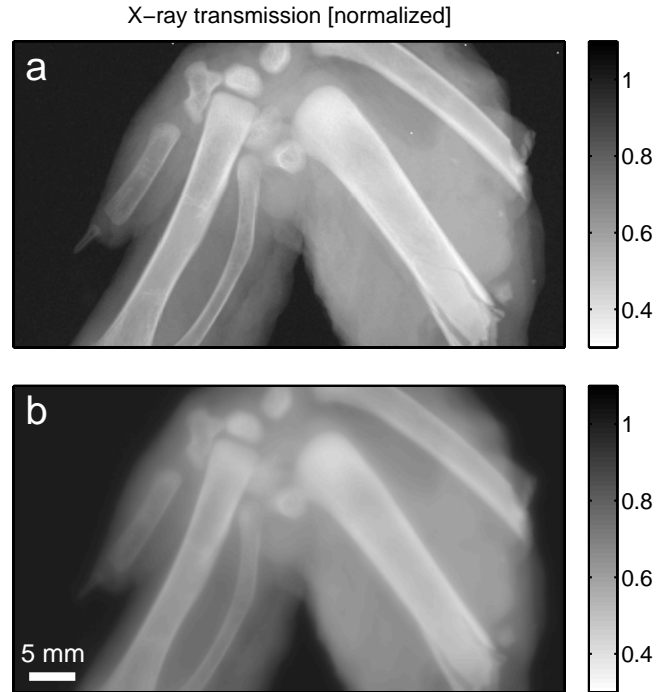


FIG. 2: X-ray absorption images of a chicken wing test sample. (a) Results obtained with the PILATUS pixel detector. (b) Results obtained with the CCD imaging system. Both images were acquired using the same total exposure time (80 sec) and identical settings on the x-ray generator (40 kV/ 25 mA).

As can be seen already qualitatively by comparing the images shown in Fig. 2a (PILATUS) and Fig. 2b (CCD), the results obtained with the PILATUS exhibit much finer details. For comparison, the images have been cropped to the same region of interest of 60

x 33 mm². Significantly better resolved are, for example, the image details showing smaller bone fragments, as can be seen on the lower, right half of the image.

In addition to standard x-ray absorption imaging we have carried out further tests to characterize the applicability of the PILATUS detector especially for x-ray phase contrast imaging [8, 9]. Phase contrast imaging has, particularly in the context of medical imaging and for relatively large samples, only very recently become possible with standard x-ray tubes [1]. Phase contrast imaging is believed to complement absorption based imaging and provide more contrast where the x-ray absorption contrast is relatively poor, e.g. in those cases where different forms of tissue with similar absorption cross-sections are under investigation (e.g., mammography or angiography).

Figure 3 shows phase contrast imaging results for both detection systems, which were obtained using a three grating interferometer setup and the same test sample. The gratings were fabricated for an x-ray energy band pass of $\pm 10\%$ around a design energy of 28 keV and the interferometer was operated in the first Talbot distance (see [1] and [10] for more details on the principles of grating based x-ray phase contrast imaging).

Because of the differential nature of the phase gradient images obtained with a grating interferometer, the images exhibit more edge contrast than the conventional absorption images. Due to the emphasis of such edge contrast effects, the image quality can be degraded severely if the effective point spread function of a detection system significantly differs from a box function given by the size of a single pixel. This effect is clearly observed for the CCD based imaging system (Fig. 3b). In this case it is mainly a result of multiple light reflections in the scintillator and the intrinsic optical resolution of the lens objective, which yield an effective point spread function with non-negligible tails extending over several pixels. Due to the box-like point spread function of the PILATUS detector, such an image degradation is not observed in Fig. 3a, where the edge contrast is very clearly reproduced.

For a more quantitative assessment of the imaging performance of the two detection systems, a power spectrum analysis of the obtained images was carried out. More precisely, the corrected images, as shown in Fig. 2 and Fig. 3 have been Fourier transformed using a discrete two-dimensional fast fourier transform and radially integrated. The resulting power spectra for both the PILATUS and the CCD imaging system are plotted in a double logarithmic representation as a function of the spatial frequency in Figure 4. Due to the symmetry of the Fourier transform, the power spectrum is truncated at a maximum spatial

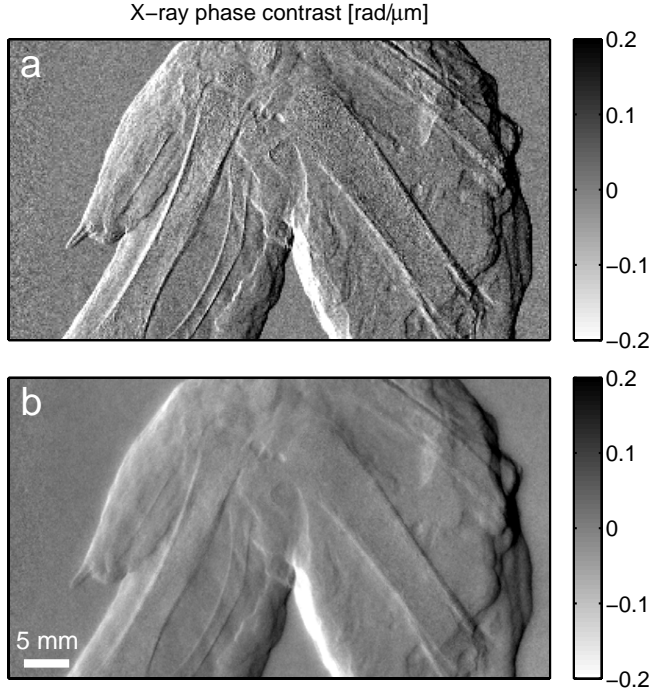


FIG. 3: X-ray phase contrast images of the test sample. (a) Results obtained with the PILATUS pixel detector. (b) Results obtained with the CCD imaging system. Both images were acquired using the same total exposure time (80 sec) and identical settings on the x-ray generator (40 kV/25 mA).

frequency which corresponds to half of the inverse pixel size (Nyquist frequency). In the case of the PILATUS pixel size of 0.172 mm, this maximum spatial frequency corresponds to 2.91 mm^{-1} . Both the results for the absorption images (Fig. 4a) and the phase contrast images (Fig. 4b) are shown.

What has been observed qualitatively further above (Fig. 2 and Fig. 3), namely that the image quality produced by the PILATUS detector produces sharper contrast features, is clearly reflected in the corresponding power spectra. The faster decay of the power spectra towards higher spatial frequencies for the CCD imaging system (blue curves in Fig. 4) are a direct consequence of the broader point spread function of this detection system. Especially

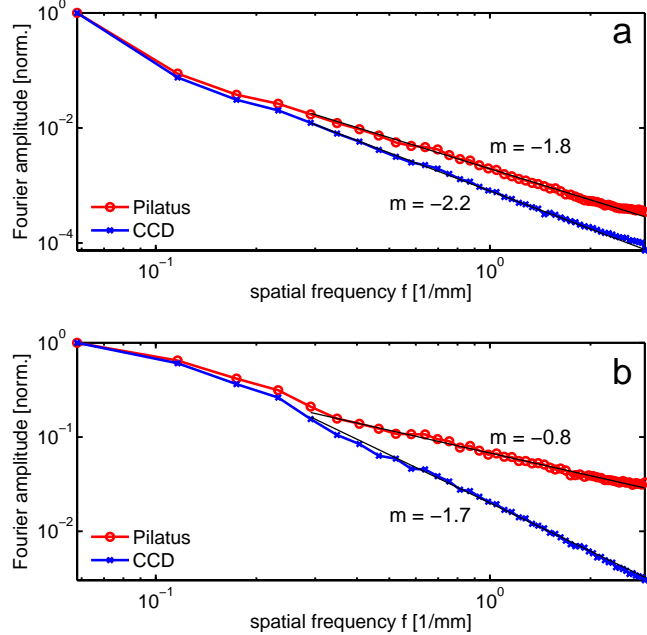


FIG. 4: Power spectrum analysis of the images shown in (a) Fig. 2 and (b) Fig. 3. The solid black lines represent power law fits to the experimental data (see text).

clear is the difference in the detector response functions if the power spectra of the differential phase contrast images are compared (Fig. 4b). Due to the fact that the differential signal *per se* drops more slowly for higher frequencies, the effects of the different point spread functions are even more pronounced than in the corresponding absorption spectra.

Because of the almost linear behavior of the asymptotic drop-off in a double logarithmic representation toward higher spatial frequencies (Fig. 4) the data lends itself to an analysis using a simple power law function in the form of f^m , where f is the spatial frequency and m the power law exponent of the radially averaged image power spectrum. Fits of power law functions to the measured power spectra together with values for the slope are shown as black lines in Figure 4. For the power spectra of the absorption images (Fig. 4a), we find values of $m = -1.8$ (PILATUS) and $m = -2.2$ (CCD). The corresponding values for the phase contrast curves could be determined to: $m = -0.8$ (PILATUS) and $m = -1.7$ (CCD), respectively.

IV. CONCLUSIONS

Based on the results we conclude that the PILATUS detector can very well be used for x-ray imaging applications. Particularly for applications, where high resolution, i.e. spatial resolution of less than 100 microns, is not required, the PILATUS represents an excellent alternative to conventional x-ray imaging systems. Particularly in those cases where the imaging method crucially depends on a correct representation of high spatial frequencies in the image, as is, for example, the case in phase contrast imaging, the PILATUS offers clear advantages over conventional systems.

Future improvement of the PILATUS system, in particular in the direction of smaller pixels and a higher absorption cross section of the sensor for hard x-rays [11], will result in a further improvement of the image quality and efficiency. These improvements together with the fast read out system and the high signal to noise ratios will then open up the way for applications of the PILATUS detector in more challenging applications, as e.g. medical computerized tomography (CT) or non-destructive industrial inspection systems.

V. ACKNOWLEDGEMENTS

We gratefully acknowledge the assistance of M. Dierolf in the experiments and C. Grünzweig for the grating fabrication.

-
- [1] F. Pfeiffer, T. Weitkamp, O. Bunk, and C. David, *Nature Physics* **2**, 258-261 (2006).
 - [2] C. M. Schlepütz, R. Herger, P. R. Willmott, B. D. Patterson, O. Bunk, Ch. Brönnimann, B. Henrich, G. Hülsen, and E. F. Eikenberry, *Acta Cryst. A* **61**, 418-425 (2005).
 - [3] C. Brönnimann, E. F. Eikenberry, B. Henrich, R. Horisberger, G. Hülsen, E. Pohl, B. Schmitt, C. Schulze-Briese, M. Suzuki, T. Tomizaki, H. Toyokawa, and A. Wagner, *J. Syn. Rad.* **13**, 120-130 (2006).
 - [4] G. Hülsen, C. Brönnimann, E. F. Eikenberry, and A. Wagner, *J. Appl. Cryst.* **39**, 550-557 (2006).
 - [5] Hamamatsu x-ray scintillation screen, ACS type, Nr. J8734-01.
 - [6] Pentax 50 mm (1:1.2) photo objective and close-up lens.

- [7] Fingerlakes Instruments, FLI IMG 1001, KODAK chip with 1024 x 1024 pixels, $24 \times 24 \mu\text{m}^2$ pixel size.
- [8] R. Fitzgerald, Physics Today **53** 7, 23-27 (2000).
- [9] A. Momose, Jap. J. Appl. Phys **44**, 6355 (2005).
- [10] T. Weitkamp, A. Diaz, C. David, F. Pfeiffer, M. Stampanoni, P. Cloetens, and E. Ziegler, Optics Express **13**, 6296-6304 (2005).
- [11] The current version of the PIATUS II features a $300 \mu\text{m}$ thick Si sensor, which has a quantum detection efficiency given by the absorption probability of the x-rays in the material of $\simeq 10\%$ (at 28 keV). Thicker Si sensors (up to $700 \mu\text{m}$ or more) are a possible improvement and could increase the quantum efficiency significantly ($\simeq 23\%$ at 28 keV for $700 \mu\text{m}$ silicon). Even higher energies would be accessible if other sensor materials, i.e. stronger x-ray absorbers, such as GaAs or Ge, could be used.

Publication IV

Physical Review Letters (2008)

Franz Pfeiffer, Christian David, Oliver Bunk, Tilman Donath, **Martin Bech**,
Geraldine Le Duc, Alberto Bravin and Peter Cloetens

Region-of-Interest Tomography for Grating-Based X-Ray Differential Phase-Contrast Imaging

Physical Review Letters 101 (2008) 168101

Region-of-Interest Tomography for Grating-Based X-Ray Differential Phase-Contrast Imaging

F. Pfeiffer

*Paul Scherrer Institut, 5232 Villigen PSI, Switzerland
Ecole Polytechnique Fédérale de Lausanne, 1015 Lausanne, Switzerland*

C. David, O. Bunk, and T. Donath

Paul Scherrer Institut, 5232 Villigen PSI, Switzerland

M. Bech

Niels Bohr Institute, University of Copenhagen, 2100 Copenhagen, Denmark

G. Le Duc, A. Bravin, and P. Cloetens

*European Synchrotron Radiation Facility, B.P. 220, 38043 Grenoble Cedex, France
(Received 28 April 2008; revised manuscript received 18 August 2008; published 16 October 2008)*

We report numerical and experimental results demonstrating accurate region-of-interest computed tomography (CT) reconstruction based on differential phase-contrast projection (DPC) images. The approach removes the constraint of covering the entire sample within the field of view of the image detector. Particularly for biomedical applications, the presented DPC-CT region-of-interest approach will allow for the visualization of previously inaccessible details deep inside an entire animal or organ. We envisage that this development will also be of interest for potential future clinical applications, because grating-based DPC-CT can be implemented with standard x-ray tube sources.

DOI: 10.1103/PhysRevLett.101.168101

PACS numbers: 87.59.-e, 07.85.Fv, 87.85.Pq

Absorption-based x-ray computed tomography (CT) is a well-established, nondestructive investigation method with numerous applications in life and material science. Phase-contrast computed tomography (PC-CT), which uses the phase shift rather than the absorption as the imaging signal, offers the potential of substantially increased contrast in soft tissue samples [1,2]. Several approaches for PC-CT have been developed in the past years [3–13]. One of the more recent developments is differential phase-contrast computed tomography (DPC-CT), based on a grating interferometer [10,12,14,15]. DPC-CT has successfully been implemented at x-ray synchrotron radiation sources for high-resolution and high-sensitivity micro-CT investigations [10,16,17]. The method is furthermore interesting for potential future medical applications of phase-contrast CT, since DPC-CT can also be implemented with more readily available x-ray sources, such as standard x-ray tubes [18].

That computed tomography image reconstruction based on differential phase-contrast projection data can conveniently be achieved by combining a backprojection procedure with a Hilbert filter has been demonstrated by several groups [18–20]. A major experimental constraint until now, however, is the requirement that the object has to fit entirely into the field of view covered by the image detector. This poses a severe limitation on practical applications, where, e.g., a small region of interest deep inside a large specimen is to be imaged with high resolution.

Here we report numerical and experimental results that demonstrate the feasibility of DPC-CT based on projection

images that do not entirely cover the whole object. Moreover, we show that artifacts, which are known to appear in the case of conventional, absorption-based region-of-interest CT reconstructions [21], are not present in DPC-CT.

For the following, we consider a three-dimensional (3D) object described by a refractive index distribution $n(x, y, z) = 1 - \delta(x, y, z) + i\beta(x, y, z)$. In a conventional, absorption-based CT setup, the imaginary part β is measured by the attenuation of the x rays transmitted through the specimen. A transmission projection t_θ in a plane defined by $z = z_0$ through the object can be described by combining the Radon transform of the object with Beer-Lambert's law [22]:

$$t_\theta(y') = \exp \left[- \int_{-\infty}^{\infty} \frac{4\pi}{\lambda} \beta(x', y') dx' \right], \quad (1)$$

where x' and y' denote a coordinate system which is rotated by an angle θ around the z axis with respect to x and y , respectively, and λ the x-ray wavelength. Note that we have omitted the variable z because it does not affect the further derivation.

In differential phase-contrast imaging, one measures the effect of variations of the real part δ of the refractive index of the object by evaluating the tiny refraction angles of x rays induced by the specimen. Correspondingly, a differential phase-contrast projection α_θ can be expressed by [19]

$$\alpha_\theta(y') = \frac{\lambda}{2\pi} \frac{\partial \Phi_\theta(y')}{\partial y'} = \int_{-\infty}^{\infty} \frac{\partial \delta(x', y')}{\partial y'} dx', \quad (2)$$

where $\Phi_\theta(y')$ is the spatially dependent, total relative phase shift imprinted on the x-ray wave front upon propagating through the specimen.

To reconstruct the original complex refractive index distribution of the object, i.e., $\beta(x, y)$ and $\delta(x, y)$, from a set of projection images described by Eqs. (1) and (2), a filtered backprojection (FBP) algorithm is usually employed [22]. In the case of the transmission projections, as obtained in conventional CT, the reconstruction formula can be written as [22]

$$\beta(x, y) = - \int_0^\pi \mathcal{FT}^{-1}[\tilde{p}_\theta(v')\tilde{k}(v')]d\theta, \quad (3)$$

where $\tilde{p}_\theta(v')$ represents the Fourier transform of the logarithm of the normalized transmission projection $t_\theta(y')$, v' is the Fourier space coordinate corresponding to the real space coordinate y' , \mathcal{FT}^{-1} denotes the inverse Fourier transform operator, and $\tilde{k}(v')$ is the filter function in Fourier space. The latter is given by $\tilde{k}(v') = |v'|$ [23].

In the case where differential phase-contrast projections [Eq. (2)] are measured, a reconstruction of $\delta(x, y)$ is achieved by [22]

$$\delta(x, y) = \int_0^\pi \mathcal{FT}^{-1}[\tilde{\alpha}_\theta(v')\tilde{h}(v')]d\theta, \quad (4)$$

where $\tilde{\alpha}_\theta(v')$ represent the Fourier transform of the projections of the measured deflection angles and $\tilde{h} = 1/2\pi i \text{sgn}(v')$ is the imaginary filter function for gradient projections [23].

In order to investigate the validity of the CT reconstructions obtained through Eqs. (3) and (4), in particular, for the case of region-of-interest reconstructions, we have carried out numerical tests. In the first step, we calculated both absorption and phase-contrast projection images for a phantom consisting of a distribution of circles [Fig. 1(a)] characterized by a refractive index of $n = 1 - 4.26 \times 10^{-7} + i1.57 \times 10^{-10}$ [24]. The corresponding absorption and differential phase-contrast sinograms were calculated using an algorithm based on Eqs. (1) and (2) for an angular interval $\theta \in [0, \pi]$ and are shown in Figs. 1(b) and 1(c). The calculated sinograms consist of 1500 steps along the angular coordinate and 1024 pixels along the transverse y' coordinate. In the following step, CT reconstructions, according to Eqs. (3) and (4), were carried out and compared to the original phantom.

Figures 2(a)–2(c) display the results of the CT reconstructions of the phantom $\beta(x, y)$ distribution, obtained by applying Eq. (3) to the calculated absorption sinogram [Fig. 1(b)]. Line profiles through the center of the reconstructed (solid red line) and original β values of the phantom (dashed black line) are shown in Figs. 2(d)–2(f). In Fig. 2(a) [and 2(d)], the full extent ($\gamma = 1$) of the sinogram in the y' direction was used as input for the re-

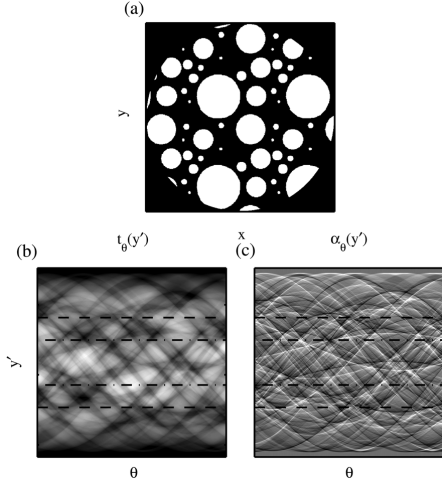


FIG. 1. (a) Schematic representation of the phantom used for the numerical simulation. The white areas denote values of $\beta = 1.57 \times 10^{-10}$ and $\delta = 4.26 \times 10^{-7}$. (b) Calculated attenuation sinogram, as given by Eq. (1). (c) Calculated phase gradient sinogram, as given by Eq. (2). The dashed-dotted and dashed lines mark the selected projection range for the region-of-interest reconstructions displayed in Figs. 2(b), 2(c), 3(b), and 3(c).

construction, whereas Fig. 2(b) [and 2(e)] and Fig. 2(c) [and 2(f)] represent results where only the center half ($\gamma = 0.5$) or quarter ($\gamma = 0.25$) was used. We observe that, apart from some high frequency noise induced by the FBP

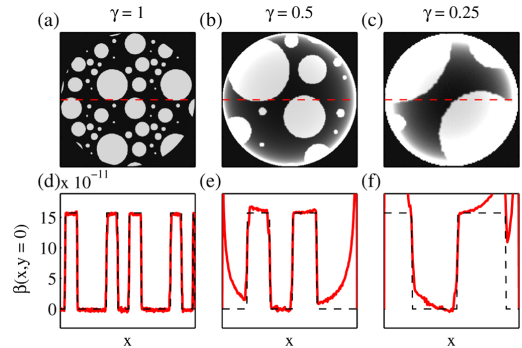


FIG. 2 (color online). (a)–(c) CT reconstructions of the phantom $\beta(x, y)$ distribution from the calculated absorption sinogram [Fig. 1(b)], using Eq. (3). (d)–(f) Line profiles through the center of the reconstructed (solid red line) and original β values (dashed black line). In (a),(d), the full extent ($\gamma = 1$) of the sinogram in the y' direction was used as input for the CT reconstruction, whereas (b),(e) and (c),(f) represent results where only the center half ($\gamma = 0.5$) or quarter ($\gamma = 0.25$) was used.

algorithm, the phantom is correctly reconstructed when the full sinogram is used, i.e., when the sample is entirely contained in the field of view [$\gamma = 1$, Figs. 2(a) and 2(d)]. In the cases where truncated projections ($\gamma < 1$) are used as input for the FBP, low spatial frequency artifacts occur in the corresponding reconstructions [see Fig. 2(b) or 2(e) and 2(c) or 2(f)]. These artifacts, which increasingly harm the reconstruction with increasing distance from the center of rotation, are well-known and reported in the literature (see, for example, [25]). These artifacts basically stem from the fundamental mathematical properties of the Radon transform that cause a nonlocality in the case of absorption-based CT reconstructions [21,25].

In contrast to this, we do not observe these artifacts in the case of CT reconstructions based on differential phase-contrast projections. This is shown in Fig. 3, where panels (a)–(c) display DPC-CT reconstructions of the phantom $\delta(x, y)$ distribution, obtained by applying Eq. (4) to the calculated phase-contrast sinogram [Fig. 1(c)]. Additional line profiles through the center of the reconstructed (solid blue line) and original δ values (dashed black line) are shown in Figs. 3(d)–3(f). In Fig. 3(a) [and 3(d)], the full extent ($\gamma = 1$) of the sinogram in the y' direction was used as input for the CT reconstruction, whereas Fig. 3(b) [and 3(e)] and Fig. 3(c) [and 3(f)] represent results where only the center half ($\gamma = 0.5$) or quarter ($\gamma = 0.25$) was used. We observe that, apart from some high spatial frequency noise induced by the FBP algorithm, the phantom is correctly reconstructed in all cases, even for $\gamma < 1$, i.e., also in the cases where the sample is not entirely contained in the field of view. These findings are in agreement with what was predicted theoretically [26,27] and demonstrated

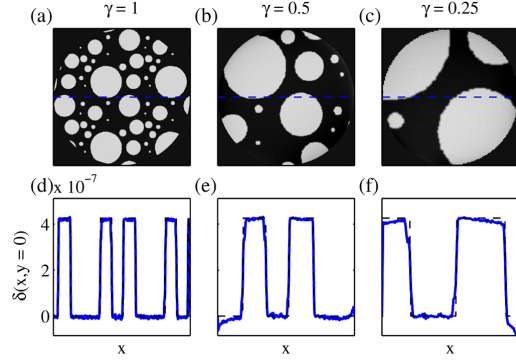


FIG. 3 (color online). (a)–(c) CT reconstructions of the phantom $\delta(x, y)$ distribution from the calculated phase-contrast sinogram [Fig. 1(c)], using Eq. (4). (d)–(f) Line profiles through the center of the reconstructed (solid blue line) and original δ values (dashed black line). In (a),(d), the full extent ($\gamma = 1$) of the sinogram in the y' direction was used as input for the CT reconstruction, whereas (b),(e) and (c),(f) represent results where only the center half ($\gamma = 0.5$) or quarter ($\gamma = 0.25$) was used.

for the case of propagation-based (inline) phase-contrast imaging in Ref. [21].

We experimentally verified our conclusions drawn from the numerical studies presented further above by reconstructing regions of interests from measured DPC sinograms [see Fig. 4(a)]. The experimental data set used for the reconstruction was recorded in an imaging experiment carried out at the beam line ID19 of the European Synchrotron Radiation Facility (ESRF, Grenoble) using a two-grating interferometer [17]. The specimen was a rat brain fixed in a 4% formalin solution. A monochromatic x-ray beam of 24.9 keV ($\lambda = 0.498 \text{ \AA}$) was used for the measurements. The images were recorded using a $15 \mu\text{m}$ thick polycrystalline gadolinium oxysulphide scintillation screen with a magnifying optical lens system and a cooled charge coupled device (CCD) [28]. The full field of view was $16.1 \times 16.1 \text{ mm}^2$. For the acquisition of a full tomographic data set, the object was rotated around the tomographic rotation axis and differential phase-contrast projection images were recorded for each projection angle [29]. In total, 721 differential phase-contrast projections over an angular range of $\theta \in [0, 2\pi]$ were recorded (see [17,30] for further details on the experimental setup).

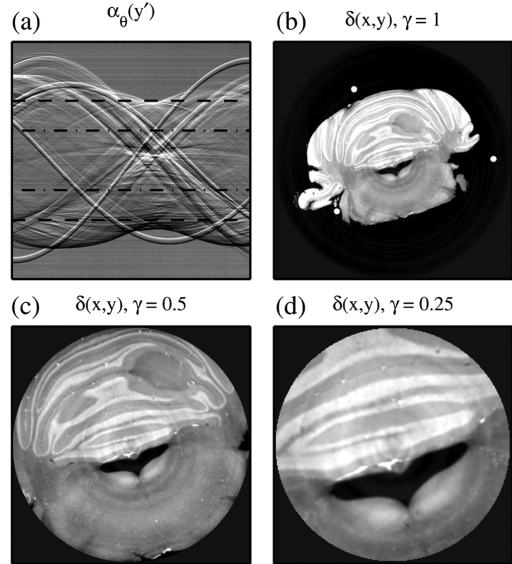


FIG. 4. (a) Measured differential phase-contrast projection sinogram of a rat brain specimen ($\theta \in [0, \pi]$). (b) Full DPC-CT reconstruction and (c),(d) region-of-interest DPC-CT reconstruction of the specimen $\delta(x, y)$ distribution using Eq. (4). In (b), the full extent ($\gamma = 1$) of the sinogram in the y' direction was used as input for the DPC-CT reconstruction, whereas (c),(d) represent results where only the center half ($\gamma = 0.5$) or the center quarter ($\gamma = 0.25$) was used.

Figure 4(b) displays a DPC-CT reconstruction of δ using the full data set ($\gamma = 1$). In this case, the specimen is fully contained in the field of view of the image detector, for all angular projections. Figures 4(c) and 4(d) show reconstructions where only the center half [the region between the two dashed lines in Fig. 4(a)] or the center quarter [the region between the two dashed-dotted lines in Fig. 4(a)] was used as input for Eq. (4). In both cases, where $\gamma < 1$, we do not observe any artifacts from the truncation of the sinograms.

In summary we have demonstrated, both numerically and with real experimental data, that artifact-free region-of-interest tomography reconstructions based on differential phase-contrast projection images are possible. This procedure removes the constraint of fully covering the whole sample within the field of view given by the detector. We envisage that, particularly for medical applications, where phase-contrast DPC-CT has been proven to be a uniquely powerful method, a region-of-interest approach will allow for the visualization of previously inaccessible, high-resolution details deep inside a whole animal or organ. In such a way, micron-resolved three-dimensional imaging of, e.g., the detailed blood-vessel network structure in a living rat or mouse can be envisioned in the future [17]. Finally, we believe that the method will also be of interest for future clinical applications of x-ray CT, because DPC-based imaging can be carried out with standard x-ray tube sources [14,18] and extended to fan-beam CT reconstruction schemes.

We gratefully acknowledge C. Grünzweig for the fabrication of the grating structures, the assistance of C. Kottler during the experiments, and T. Weitkamp for fruitful discussions.

- [1] R. Fitzgerald, Phys. Today **53**, No. 7, 23 (2000).
- [2] A. Momose, Jpn. J. Appl. Phys. **44**, 6355 (2005).
- [3] U. Bonse and F. Busch, Prog. Biophys. Molec. Biol. **65**, 133 (1996).
- [4] C. Raven, A. Snigirev, I. Snigireva, P. Spanne, A. Suvorov, and V. Kohn, Appl. Phys. Lett. **69**, 1826 (1996).
- [5] F. Beckmann, K. Heise, B. Kolsch, U. Bonse, M. F. Rajewsky, and T. Biermann, Biophys. J. **76**, 98 (1999).
- [6] P. Cloetens, W. Ludwig, J. Baruchel, D. van Dyck, J. van Landuyt, J. P. Guigay, and M. Schlenker, Appl. Phys. Lett. **75**, 2912 (1999).
- [7] F. A. Dilmanian, Z. Zhong, B. Ren, X. Y. Wu, L. D. Chapman, I. Orion, and W. C. Thominson, Phys. Med. Biol. **45**, 933 (2000).
- [8] S. C. Mayo, T. J. Davis, T. E. Gureyev, P. R. Miller, D. Paganin, A. Pogany, A. W. Stevenson, and S. W. Wilkins, Opt. Express **11**, 2289 (2003).
- [9] P. J. McMahon, A. G. Peele, D. Paterson, J. J. A. Lin, T. H. K. Irving, I. McNulty, and K. A. Nugent, Opt. Commun. **217**, 53 (2003).

- [10] T. Weitkamp, A. Diaz, C. David, F. Pfeiffer, M. Stampanoni, P. Cloetens, and E. Ziegler, Opt. Express **13**, 6296 (2005).
- [11] A. Groso, M. Stampanoni, R. Abela, P. Schneider, S. Linga, and R. Müller, Appl. Phys. Lett. **88**, 214104 (2006).
- [12] A. Momose, W. Yashiro, Y. Takeda, Y. Suzuki, and T. Hattori, Jpn. J. Appl. Phys. **45**, 5254 (2006).
- [13] A. Bravin *et al.*, Phys. Med. Biol. **52**, 2197 (2007).
- [14] F. Pfeiffer, T. Weitkamp, O. Bunk, and C. David, Nature Phys. **2**, 258 (2006).
- [15] F. Pfeiffer, M. Bech, O. Bunk, P. Kraft, E. F. Eikenberry, C. Brönnimann, C. Grünzweig, and C. David, Nature Mater. **7**, 134 (2008).
- [16] C. David, T. Weitkamp, F. Pfeiffer, A. Diaz, J. Bruder, T. Rohbeck, A. Groso, O. Bunk, M. Stampanoni, and P. Cloetens, Spectrochim. Acta, Part B **62**, 626 (2007).
- [17] F. Pfeiffer, O. Bunk, C. David, M. Bech, G. Le Duc, A. Bravin, and P. Cloetens, Phys. Med. Biol. **52**, 6923 (2007).
- [18] F. Pfeiffer, C. Kottler, O. Bunk, and C. David, Phys. Rev. Lett. **98**, 108105 (2007).
- [19] G. W. Faris and R. L. Byer, Appl. Opt. **27**, 5202 (1988).
- [20] Ya. I. Nesterets, T. E. Gureyev, and S. W. Wilkins, Appl. Phys. Lett. **89**, 264103 (2006).
- [21] T. E. Gureyev, Ya. I. Nesterets, and S. C. Mayo, Opt. Commun. **280**, 39 (2007).
- [22] C. A. Kak and M. Slaney, *Principles of Computerized Tomography* (IEEE, New York, 1987).
- [23] In practice, where the projections are sampled with a finite resolution $\Delta y'$, the filter is truncated at the Nyquist frequency $1/2\Delta y'$.
- [24] These values for the refractive index correspond to polymethylmethacrylate (C5H8O2) at a wavelength $\lambda = 0.5 \text{ \AA}$ ($E = 25 \text{ keV}$).
- [25] A. G. Ramm and A. I. Katsevich, *The Radon Transform and Local Tomography* (CRC Press, Boca Raton, 1996).
- [26] F. Noo, R. Clackdoyle, and J. D. Pack, Phys. Med. Biol. **49**, 3903 (2004).
- [27] M. A. Anastasio and X. Pan, Opt. Lett. **32**, 3167 (2007).
- [28] We used the FReLoN 2000 (a fast-readout, low-noise CCD developed at the ESRF) with 1024×1024 pixels and a $28.0 \times 28.0 \mu\text{m}^2$ pixel size (in the 2×2 binning mode). Because of the magnifying lens system, the effective pixel size in the recorded images was $16.1 \times 16.1 \mu\text{m}^2$. For more details on the CCD, see, e.g., P. Coan *et al.*, J. Synchrotron Radiat. **13**, 260 (2006).
- [29] For one projection, eight individual raw images (phase stepping) with exposure times of 0.4 seconds each were recorded. The DPC projections were obtained by extracting the phase of the first Fourier component after applying a one-dimensional discrete fast Fourier transform on the intensity values recorded during a phase-stepping scan in each detector pixel [10,15,18].
- [30] The interferometer was placed at a distance of 140 m from the wiggler source. The gratings were fabricated by a process involving photolithography, deep etching into silicon, and electroplating of gold. The first grating (Si phase grating, G1) had a period of $p_1 = 3.99 \mu\text{m}$ and a height of $h_1 = 31.7 \mu\text{m}$. The corresponding values for the second grating (gold absorber grating, G2) were $p_1 = 2.00 \mu\text{m}$ and $h_2 = 30 \mu\text{m}$. The distance between G1 and G2 was 361 mm. See [17] for more details on the experimental setup.

Publication V

Journal of Synchrotron Radiation (2009)

Martin Bech, Oliver Bunk, Christian David, Ron Ruth, Jeff Rifkin, Rod Loewen, Robert Feidenhans'l and Franz Pfeiffer

Hard X-ray phase-contrast imaging with the Compact Light Source based on inverse Compton X-rays

Journal of Synchrotron Radiation 16 (2009) 43–47

ISSN 0909-0495

Volume 16

Part 1

January 2009

Synchrotron radiation sources

Beamlines and optics

Detectors

Electronics and data acquisition

Sample chambers and environment

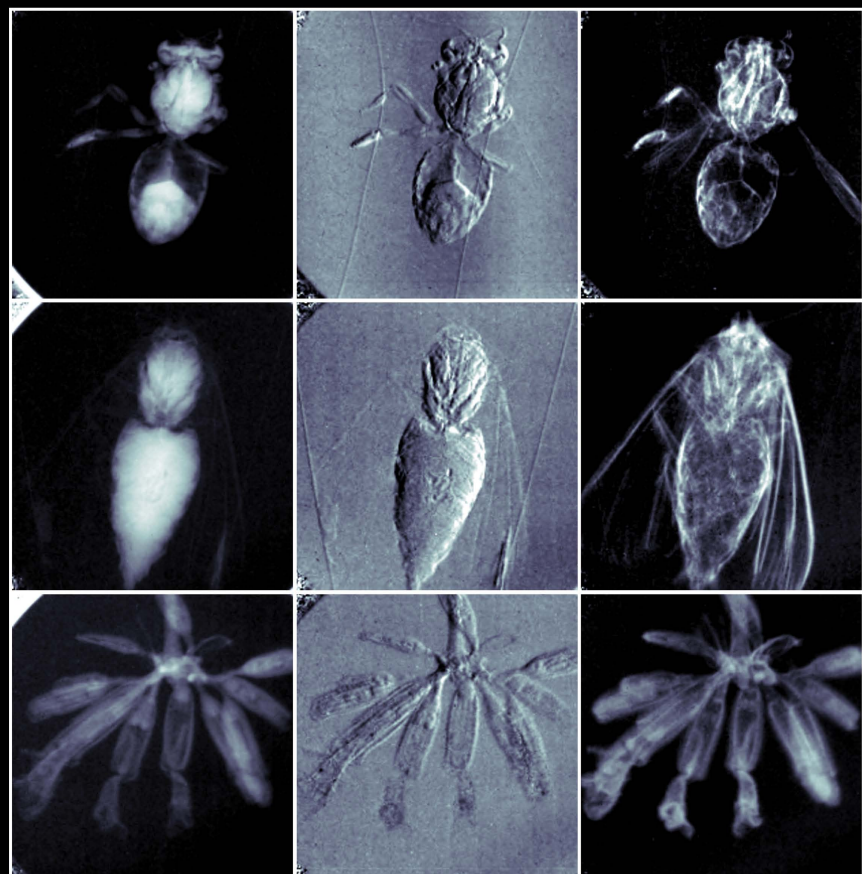
Diffraction

Spectroscopy

Imaging

Journal of Synchrotron Radiation

Editors: G. E. Ice, Å. Kvick and T. Ohta



journals.iucr.org
International Union of Crystallography
Wiley Blackwell

Received 6 September 2008
 Accepted 23 October 2008

Hard X-ray phase-contrast imaging with the Compact Light Source based on inverse Compton X-rays

Martin Bech,^{a*} Oliver Bunk,^b Christian David,^b Ronald Ruth,^{c,d} Jeff Rifkin,^c Rod Loewen,^c Robert Feidenhans'l^a and Franz Pfeiffer^{b,e*}

^aUniversity of Copenhagen, Universitetsparken 5, DK-2100 Copenhagen, Denmark, ^bPaul Scherrer Institut, CH-5232 Villigen PSI, Switzerland, ^cLyncean Technologies Inc., 370 Portage Avenue, Palo Alto, CA 94306, USA, ^dStanford Linear Accelerator Center, 2575 Sand Hill Road, Menlo Park, CA 94025, USA, and ^eÉcole Polytechnique Fédérale de Lausanne, CH-1015 Lausanne, Switzerland.
 E-mail: bech@fys.ku.dk, franz.pfeiffer@psi.ch

The first imaging results obtained from a small-size synchrotron are reported. The newly developed Compact Light Source produces inverse Compton X-rays at the intersection point of the counter propagating laser and electron beam. The small size of the intersection point gives a highly coherent cone beam with a few milliradian angular divergence and a few percent energy spread. These specifications make the Compact Light Source ideal for a recently developed grating-based differential phase-contrast imaging method.

© 2009 International Union of Crystallography
 Printed in Singapore – all rights reserved

Keywords: medical X-ray imaging; phase contrast; inverse Compton X-rays.

1. Introduction

For more than a hundred years X-rays have been used for medical purposes. X-ray imaging has played a key role in medical diagnosis since the discovery of X-rays in 1895 by Röntgen, and the invention of the CAT scanner for which Hounsfield and Cormack received the Nobel prize in 1972. All modern medical X-ray imaging devices are based on the attenuation through photoelectric absorption of the X-rays penetrating the specimen to be imaged. However, for soft tissue with little absorption, this provides poor contrast. It is well known that X-ray imaging of soft tissue, *e.g.* mammography screenings, provides little contrast compared with bone images. This problem of low absorption contrast in soft tissue can be overcome with phase-contrast imaging (Fitzgerald, 2000; Momose, 2005).

During the last few decades several imaging techniques have been developed based on the phase shift of X-ray waves owing to refraction (Bonse & Hart, 1965; Ingal & Beliaevskaya, 1995; Davis *et al.*, 1995; Momose *et al.*, 1996; Wilkins *et al.*, 1996; Nugent *et al.*, 1996). Though the specific requirements are different for the techniques, the X-ray source for medical X-ray phase-contrast imaging must fulfill two requirements: there must be some degree of spatial and temporal coherence, and the beam must be large enough to cover a reasonable field of view.

A standard X-ray tube can be used for phase-contrast imaging by grating interferometry (Pfeiffer *et al.*, 2006, 2008), and, at X-ray tubes with a fine focus, it is possible to perform propagation-based phase-contrast imaging (Wilkins *et al.*,

1996; Nugent *et al.*, 1996). The grating-based method for phase-contrast imaging with standard X-ray tubes is, however, limited by loss of visibility owing to the broad spectrum of the X-ray tube, and, as the propagation-based phase-contrast imaging relies on high-resolution detectors to measure the Laplacian of the phase, it is thus limited in the field of view and does not supply dark-field images (Pfeiffer *et al.*, 2008).

The best results for high-resolution and high-sensitivity phase-contrast applications are obtained on brilliant and narrow band-pass X-ray sources (Momose *et al.*, 2003, 2006; Weitkamp *et al.*, 2005; Tafforeau *et al.*, 2006; Pfeiffer, Bunk *et al.*, 2007; David, Weitkamp *et al.*, 2007). Third-generation synchrotron radiation sources certainly offer the necessary beam quality and brilliance, but they are far too costly and they are incompatible with a clinical environment. The Compact Light Source (CLS) fulfills both requirements mentioned above, and thus is a promising source for future clinical X-ray phase-contrast imaging applications.

In this paper we will present the first phase-contrast images made with the CLS and show that differential phase-contrast imaging based on a grating interferometer is ideally matched to the CLS X-ray beam.

2. The Compact Light Source

The CLS is a miniature synchrotron for the conventional laboratory developed by Lyncean Technologies Inc. Whereas the insertion devices such as undulators and wigglers on third-generation synchrotron radiation facilities are built with permanent magnets, the CLS produces X-rays in the field

of an intense laser undulator [inverse Compton scattering (Huang & Ruth, 1998)]. The characteristic parameters for undulator radiation are γ (electron energy in units of rest mass) and λ_u (spatial period of undulator). The fundamental wavelength of X-rays emitted from a magnetic undulator is $\lambda_u/2\gamma^2$ (Als-Nielsen & McMorrow, 2001), and for magnetic undulators λ_u is typically a few centimeters, so γ needs to be of the order of 10^4 to reach a fundamental wavelength in the range of an angstrom. The fundamental wavelength for a laser undulator is $\lambda_u/4\gamma^2$ (Loewen, 2003), and as the laser undulator at the CLS has a wavelength of $\sim 1 \mu\text{m}$ we only need $\gamma \simeq 50$ to obtain a fundamental wavelength in the angstrom range. For this reason the electron energy is two orders of magnitude lower than at large-scale synchrotron facilities. This allows the CLS storage ring to be scaled down to a few meters in circumference, making it feasible for use in a conventional laboratory or for clinical use.

The beam divergence of the CLS is much larger than at normal synchrotrons (Loewen, 2003). This is an advantage in imaging, as a larger field of view can be obtained at shorter source-to-sample distances. In the current set-up, the CLS is operated at an electron energy of 25 MeV, *i.e.* at $\gamma = 50$ and with the beam collimated to $\alpha = 4 \text{ mrad}$, giving a roughly circular beam size of diameter 4 cm at 10 m from the source. The X-ray aperture can be opened to increase the beam size by trading off bandwidth, up to a maximum $\alpha \simeq 1/\gamma$. For large apertures the angular energy distribution is such that the X-ray energy is high in the forward direction, and falls off with increasing angle, giving a lower E_{peak} at the edges than in the center of the detector. As will be discussed in the *Results* section of this paper, an energy distribution will have little effect on the image quality.

3. Grating interferometer

In this set-up we have used a grating interferometer for differential phase-contrast imaging as described in detail elsewhere (Momose *et al.*, 2003; Weitkamp *et al.*, 2005; David, Bruder *et al.*, 2007; David, Weitkamp *et al.*, 2007; Pfeiffer, Kottler *et al.*, 2007). Two gratings are placed between sample and detector as illustrated in Fig. 1: a phase grating G_1 and an absorption grating G_2 . A number of images are recorded while

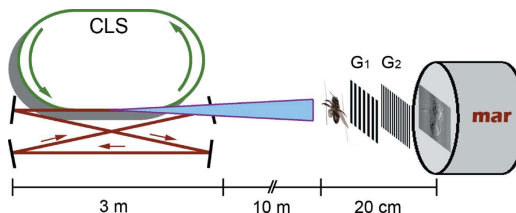


Figure 1

Sketch of the experimental set-up (not to scale). To the left is the Compact Light Source with an electron storage ring and a laser cavity. A conical X-ray beam is produced at the electron-laser intersection point, shining onto the sample. The grating interferometer to the right consists of two gratings, G_1 and G_2 , and a MAR CCD detector.

stepping the absorption grating transversely over a grating period. This will be referred to as phase stepping. If the phase shift of grating G_1 is π , the distance between the gratings must be a fractional Talbot distance d_T (Weitkamp *et al.*, 2005; Momose *et al.*, 2006). In the case of a parallel beam, d_T is given by

$$d_T = n \frac{g_1^2}{8\lambda}, \quad (1)$$

where g_1 is the period of grating G_1 , λ is the wavelength and n is an odd integer. The pitch of G_2 should be half that of G_1 , $g_1 = 2g_2$. However, in the case of a diverging beam, a magnification occurs along the beam, and a magnification factor must be included in the equations (Engelhardt *et al.*, 2007),

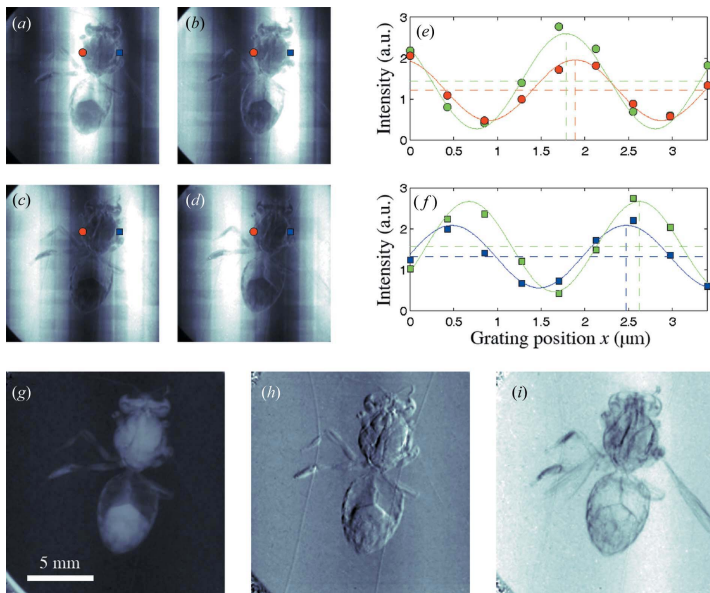
$$d_T = n \frac{g_1^2}{8\lambda} \frac{L + d_T}{L}, \quad (2)$$

$$g_1 = 2g_2 \frac{L}{L + d_T}, \quad (3)$$

where L is the distance from the source to G_1 . For a given set of gratings, these equations can be solved to give values for d_T and L . For each pixel the intensity variations during a phase-stepping period are recorded and the changes induced by the specimen are evaluated (Pfeiffer *et al.*, 2008). From the pixel intensity variations in one data set, both absorption contrast (intensity average) and phase contrast (intensity variation shift) can be extracted, and used for three-dimensional tomographical reconstructions (Pfeiffer, Kottler *et al.*, 2007). Furthermore, the interference visibility $V = (I_{\text{max}} - I_{\text{min}})/(I_{\text{max}} + I_{\text{min}})$ provides information on the local coherence of the wavefront (Pfeiffer *et al.*, 2005), giving an image signal comparable with a dark-field image showing scattered photons (Pfeiffer *et al.*, 2008). Thus one data set can be processed to give three contrast signals that can be plotted individually as images: a standard absorption image, a differential phase-contrast image and a dark-field image. This is illustrated in Fig. 2.

4. Experiment

For this experiment we have used a grating system consisting of a phase grating G_1 with $3.99 \mu\text{m}$ pitch, and an absorption grating G_2 with $2.00 \mu\text{m}$ pitch. The two gratings have an area of $15 \text{ mm} \times 15 \text{ mm}$, thus limiting the field of view to this area. The distance $d_T = 22 \text{ mm}$ between the two gratings corresponds to the first fractional Talbot distance, $n = 1$ in equation (2) when $L = 8.65 \text{ m}$ and $\lambda = 0.92 \text{ \AA}$. The CLS was operated at an X-ray energy of $E_{\text{peak}} = 13.5 \text{ keV}$ ($\lambda_{\text{peak}} = 0.92 \text{ \AA}$), with a full energy spread of $\Delta E/E_{\text{peak}} = 3\%$. The effective X-ray source size was $70 \mu\text{m}$ RMS corresponding to $165 \mu\text{m}$ FWHM, and the angular divergence of the X-ray beam was limited to $\pm 2 \text{ mrad}$ by a cylindrical aperture. For each data set, nine phase steps were performed over two grating periods, yielding nine images from which the absorption, differential phase, and dark-field signals were calculated. Each image was recorded with an exposure time of 100 s , hence the total exposure time

**Figure 2**

X-ray images of a bee and pixel intensity variations. (a)–(d) Raw images during phase stepping. (e)–(f) Intensity plot of two detector pixels during phase stepping. The green plot is from the flat-field data (without sample present), red and blue plots are with sample present corresponding to the intensity in the red and blue pixels in (a)–(d). Panels (g)–(i) show the three types of contrast obtained from data processing: (g) standard absorption image, (h) differential phase-contrast image, (i) dark-field image.

was 900 s per data set. (We note that the exposure time of 100 s per image, as used for this proof-of-principle experiment, is obviously too long for practical applications. However, provided that the CLS reaches its final design specifications, the total exposure could be reduced to below 1 s.) All images were recorded using a MAR CCD detector with square pixels of size $78 \mu\text{m} \times 78 \mu\text{m}$.

5. Results

Figs. 2(a)–2(d) display the first four images of a nine-step phase-stepping series. Two pixels have been marked, and the intensity of these pixels have been plotted in Fig. 2(e) (red circles) and Fig. 2(f) (blue squares). The three types of contrast are obtained from the components of the Fourier series of measured intensity as a function of grating position. The relevant signals are extracted from the amplitude and phase of the first two Fourier components. The Fourier series of the measured intensity I as a function of grating displacement x can be written as

$$I(x) = \sum_n a_n \cos\left(\frac{2\pi n}{g_2}x + \varphi_n\right). \quad (4)$$

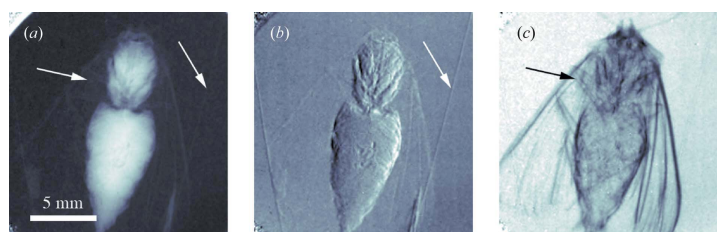
We are interested in determining the average value a_0 , the fringe position shift φ_1 and the fringe depth a_1 . As we perform nine phase steps, and the fringe profile is sufficiently sinusoidal, terms of order $n \geq 2$ can be ignored (Momose *et al.*, 2006) and the equation will read

$$I(x) = a_0 + a_1 \cos\left(\frac{2\pi}{g_2}x + \varphi_1\right), \quad (5)$$

where the average value a_0 (horizontal dashed line) corresponds to the total transmission in this pixel, the shift φ_1 (vertical dashed line) corresponds to the differential phase shift, and the modulation amplitude a_1 corresponds to the dark-field signal. In practice the Fourier components a_0 , φ_1 and a_1 are extracted from the data by use of a fast Fourier transform. To take into account the local intensity, curvature, and coherence of the X-ray beam, the raw data are compared with a set of flat-field images with no sample present. The green data points in Figs. 2(e) and 2(f) are flat-field data. Comparing the sample data with the flat-field data gives the effect on the wavefront caused by the sample. The

images obtained from plotting the relative absorption, phase shift, and visibility are shown in Figs. 2(g), 2(h) and 2(i), referred to as standard absorption (g), differential phase-contrast (h), and dark-field image (i).

A number of different samples have been imaged using the differential phase-contrast technique at the CLS. Fig. 3 shows three images of a moth obtained from one data set: (a) absorption contrast, (b) differential phase-contrast and (c) dark-field image. The arrows point to two regions where the two new types of image contrast reveals details that are very

**Figure 3**

Three types of image contrast of a moth after data processing. (a) Standard absorption-contrast image. (b) Differential phase-contrast image. (c) Dark-field image. All three images are obtained from the same data set. Arrows indicate regions where the phase-contrast and dark-field images reveal details not visible on the standard X-ray image.

research papers

difficult to see on the standard absorption image. One arrow points to a fishing wire (Fig. 3b) used for suspending the moth, the other arrow points to the leg of the moth (Fig. 3c). Obviously the wings of the moth show up nicely in the dark-field image. It is clearly shown here that the three types of contrast supplement each other well, as each image shows details different from the others.

5.1. Beam quality

In the theoretical case of a parallel monochromatic X-ray beam and a perfect absorption-free phase grating giving a π phase-shift, the visibility of the interference pattern created at the first fractional Talbot distance d_T would be 100%. However, in practice the visibility is somewhat lower owing to optical limitations such as beam coherence and grating imperfections. The effect of a finite transverse coherence length l_c on the expected fringe visibility has been calculated elsewhere (Weitkamp *et al.*, 2006) to be

$$V = \exp[-(0.94ng_2/l_c)^2], \quad (6)$$

where n is the fractional Talbot number and g_2 is the grating pitch from equations (2) and (3). The coherence length l_c is defined as $l_c = \lambda L/s$, where s is the FWHM of an assumed Gaussian source. In the current set-up we have $\lambda = 0.92 \text{ \AA}$, $n = 1$, $g_2 = 2 \mu\text{m}$ and $s = 165 \mu\text{m}$, giving a transverse coherence length of $l_c = 4.8 \mu\text{m}$. Inserting these numbers into equation (6) results in an expected visibility of 86%.

On top of the visibility loss owing to a finite transverse coherence length comes losses owing to longitudinal coherence (spectral width) and grating imperfections. When operating at the first fractional Talbot distance, a very broad spectral width is allowed without significant loss of interference visibility. The accepted bandwidth is given by $\Delta\lambda/\lambda \leq 1/n$ (Weitkamp *et al.*, 2005). Clearly the 3% bandwidth of the CLS is well below this requirement, and hence this does not limit the interference visibility.

The gratings used for this experiment were of high quality and caused no significant reduction to the visibility. From the images shown in Fig. 2, a fringe visibility of $\sim 80\%$ has been calculated. This is in good agreement with the expected value of 86%. The slightly decreased visibility may be caused by the fact that our phase grating G_1 had a height of $19.2 \mu\text{m}$, corresponding to a π phase-shift at 15 keV X-ray energy, not 13.5 keV , which was the actual energy used. Though this gives rise to a non-perfect interference pattern, it illustrates the very important fact that good visibility can be achieved at the edges of a larger beam where the X-ray energy is decreased, thus allowing the CLS to be used for grating-based phase-contrast imaging with large fields of view.

It should be noted here that the visibility of interference patterns recorded in a similar way at an X-ray tube source is considerably lower owing to the larger energy bandwidth of the polychromatic X-ray bremsstrahlung spectrum and the fact that three, instead of two, gratings have to be used with low-brilliance sources.

6. Outlook

We conclude that the Compact Light Source in combination with grating-based X-ray phase-contrast imaging has the potential to yield images of a quality previously only obtained at large-scale synchrotron radiation facilities. The small size and low cost of the CLS makes it feasible to install it in hospitals and laboratories, with all of the advantages that phase-contrast and dark-field X-ray images can offer. We believe that such an instrument could provide the required image sensitivity and resolution for improved detection of breast carcinomas in mammography applications (Fiedler *et al.*, 2004; Pisano *et al.*, 2000; Arfelli *et al.*, 2007), better differentiation of materials in security screening applications (Pfeiffer *et al.*, 2008; Harding, 2004), or biomedical investigations of tumor growth morphology in brains (Pfeiffer, Bunk *et al.*, 2007; Risser *et al.*, 2007). In addition, phase-contrast and scattering-based methods may permit a significant reduction in dose per image, since they do not rely on the absorption of an X-ray for the creation of contrast.

The authors would like to thank Jens Als-Nielsen for fruitful discussions. Lyncean Technologies Inc would like to thank Rayonix, LLC, for the loan of the marCCD 165 detector. The Compact Light Source is supported by the Protein Structure Initiative, National Institute of General Medical Sciences, grants: R44 GM 66511, R44 GM 074437, and National Institute of General Medical Sciences/National Center for Research Resources, grant U54-GM074961. These contents are solely the responsibility of the authors and do not necessarily represent the official views of the NIGMS or NCRR.

References

- Als-Nielsen, J. & McMorrow, D. (2001). *Elements of Modern X-ray Physics*. New York: John Wiley and Sons.
Arfelli, F. *et al.* (2007). *AIP Conf. Proc.* **879**, 1895–1898.
Bonse, U. & Hart, M. (1965). *Appl. Phys. Lett.* **6**, 155–156.
David, C., Bruder, J., Rohbeck, T., Grunzweig, C., Kottler, C., Diaz, A., Bunk, O. & Pfeiffer, F. (2007). *Microelectron. Eng.* **84**, 1172–1177.
David, C., Weitkamp, T., Pfeiffer, F., Diaz, A., Bruder, J., Rohbeck, T., Grosu, A., Bunk, O., Stampaoni, M. & Cloetens, P. (2007). *Spectrochim. Acta B*, **62**, 626–630.
Davis, T. J., Gao, D., Gureyev, T. E., Stevenson, A. W. & Wilkins, S. W. (1995). *Nature (London)*, **373**, 595–598.
Engelhardt, M., Baumann, J., Schuster, M., Kottler, C., Pfeiffer, F., Bunk, O. & David, C. (2007). *Appl. Phys. Lett.* **90**, 224101.
Fiedler, S., Bravin, A., Keyrilainen, J., Fernandez, M., Suortti, P., Thominson, W., Tenhunen, M., Virkkunen, P. & Karjalainen-Lindsberg, M. L. (2004). *Phys. Med. Biol.* **49**, 175–188.
Fitzgerald, R. (2000). *Phys. Today*, **53**, 23–26.
Harding, G. (2004). *Radiat. Phys. Chem.* **71**, 869–881.
Huang, Z. & Ruth, R. D. (1998). *Phys. Rev. Lett.* **80**, 976–979.
Ingal, V. & Beliaevskaya, E. (1995). *J. Phys. D*, **28**, 2314–2317.
Loewen, R. J. (2003). *A Compact Light Source: Design and Technical Feasibility Study of a Laser-Electron Storage Ring X-ray Source*. SLAC Report 632, Stanford University, USA.
Momose, A. (2005). *Jpn. J. Appl. Phys.* **44**, 6355–6367.

research papers

- Momose, A., Kawamoto, S., Koyama, I., Hamaishi, Y., Takai, K. & Suzuki, Y. (2003). *Jpn. J. Appl. Phys.* **42**, L866–L868.
- Momose, A., Takeda, T., Itai, Y. & Hirano, K. (1996). *Nat. Med.* **2**, 473–475.
- Momose, A., Yashiro, W., Takeda, Y., Suzuki, Y. & Hattori, T. (2006). *Jpn. J. Appl. Phys.* **45**, 5254–5262.
- Nugent, K. A., Gureyev, T. E., Cookson, D. F., Paganin, D. & Barnea, Z. (1996). *Phys. Rev. Lett.* **77**, 2961–2964.
- Pfeiffer, F., Bech, M., Bunk, O., Kraft, P., Eikenberry, E. F., Brönnimann, C., Grünzweig, C. & David, C. (2008). *Nat. Mater.* **7**, 134–137.
- Pfeiffer, F., Bunk, O., David, C., Bech, M., Duc, G. L., Bravin, A. & Cloetens, P. (2007). *Phys. Med. Biol.* **52**, 6923–6930.
- Pfeiffer, F., Bunk, O., Schulze-Briese, C., Diaz, A., Weitkamp, T., David, C., van der Veen, J. F., Vartanyants, I. & Robinson, I. K. (2005). *Phys. Rev. Lett.* **94**, 164801.
- Pfeiffer, F., Kottler, C., Bunk, O. & David, C. (2007). *Phys. Rev. Lett.* **98**, 108105.
- Pfeiffer, F., Weitkamp, T., Bunk, O. & David, C. (2006). *Nat. Phys.* **2**, 258–261.
- Pisano, E. D., Johnston, R. E., Chapman, D., Geradts, J., Iacobca, M. V., Livasy, C. A., Washburn, D. B., Sayers, D. E., Zhong, Z., Kiss, M. Z. & Thomlinson, W. C. (2000). *Radiology*, **214**, 895–901.
- Risser, L., Plouraboue, F., Steyer, A., Cloetens, P., Duc, G. L. & Fonta, C. (2007). *J. Cerebr. Blood F. Met.* **27**, 293–303.
- Tafforeau, P. *et al.* (2006). *Appl. Phys. A*, **83**, 195–202.
- Weitkamp, T., David, C., Kottler, C., Bunk, O. & Pfeiffer, F. (2006). *Proc. SPIE*, **6318**, 631828.
- Weitkamp, T., Diaz, A., David, C., Pfeiffer, F., Stampanoni, M., Cloetens, P. & Ziegler, E. (2005). *Opt Express*, **12**, 6296–6304.
- Wilkins, S. W., Gureyev, T. E., Gao, D., Pogany, A. & Stevenson, A. W. (1996). *Nature (London)*, **384**, 335–337.

Publication VI

Physics in Medicine and Biology (2009)

Martin Bech, Torben H. Jensen, Robert Feidenhans'l, Oliver Bunk, Christian David and Franz Pfeiffer

Soft-Tissue Phase-Contrast Tomography with X-Ray Tube Sources
Physics in Medicine and Biology 54 (2009) 2747–2753

Soft-Tissue Phase-Contrast Tomography with X-Ray Tube Source

Martin Bech¹, Torben H Jensen¹, Robert Feidenhans'l¹, Oliver Bunk², Christian David², Franz Pfeiffer^{2,3}

¹ Niels Bohr Institute, University of Copenhagen, DK-2100 Copenhagen, Denmark

² Paul Scherrer Institut, CH-5232 Villigen PSI, Switzerland

³ École Polytechnique Fédérale de Lausanne, CH-1015 Lausanne, Switzerland

E-mail: bech@fys.ku.dk, franz.pfeiffer@psi.ch

Abstract. We report the first experimental soft-tissue phase-contrast tomography results using a conventional x-ray tube source, with a millimeter-sized focal spot. The setup is based on a Talbot-Lau grating interferometer operated at a mean energy of 28 keV. We present three-dimensional ex-vivo images of a chicken heart sample, fixated in formalin. The results clearly demonstrate the advantageous contrast attainable through phase-contrast imaging over conventional attenuation-based approaches.

PACS numbers: 07.85.Fv, 87.57.Q-, 87.59.-e

Submitted to: *Phys. Med. Biol.*

1. Introduction

X-ray radiography has been used for medical imaging since the discovery of X-rays more than a hundred years ago. By the development of computed tomography (CT), x-ray imaging could be further improved and non-destructive three-dimensional (3D) views of internal structures became possible (Cormack 1963, Hounsfield 1973). In particular for medical diagnostics applications, X-ray CT became an invaluable tool during the last 30 years.

Today the contrast in x-ray CT images is essentially limited by the maximum tolerable dose, and the resulting statistical constraints when measuring the x-ray attenuation precisely along the ray trajectories. Since the absorption coefficients of soft tissue is very close to that of water, it is very difficult to distinguish internal features in the tissue.

One way to improve the contrast, is through the use of x-ray phase-contrast imaging techniques. Over the last years, essentially three different techniques have been developed: propagation-based phase-contrast imaging (Mayo et al. 2003, Cloetens et al. 2006), crystal or grating analyzer-based phase-contrast imaging (Zhong et al. 2000, Keyriläinen et al. 2002, Bravin 2003, Clauser 1998, David et al. 2002, Momose et al. 2003), and crystal interferometer-based phase-contrast imaging (Bonse & Hart 1965, Beckmann et al. 1999). In particular the recent studies of x-ray phase-contrast imaging using a grating interferometer at a synchrotron demonstrate that it is possible to distinguish subtle details in soft materials that are indistinguishable in standard absorption-based x-ray tomography (Weitkamp et al. 2005, Momose et al. 2006, Pfeiffer et al. 2007a, David et al. 2007b, Pfeiffer et al. 2008, Weitkamp et al. 2008).

Despite of these good results at synchrotron radiation sources, the data recorded at ordinary x-ray tubes has not yet demonstrated clear advantages in soft-tissue phase-contrast CT. Here, we now present the first tomographic phase-contrast images obtained with a grating interferometer, which demonstrate that high soft-tissue contrast can also be obtained with standard x-ray tube sources and centimeter-sized samples. It is obvious that this is important for a potential future medical use of the technique, since synchrotrons are not compatible with routine x-ray diagnostics in the clinics.

2. Experimental setup

In the experiments presented here, a grating interferometer and a PILATUS 100K detector module was used. The setup was installed at a Seifert ID 3000 x-ray generator operated at 40 kV/ 30 mA, with an effective source size of 0.8 mm (hor.) x 0.4 mm (ver.). The detector had 487 x 195 pixels, with a pixel size of 172 x 172 μm^2 , yielding a total field of view of 83 x 33 mm².

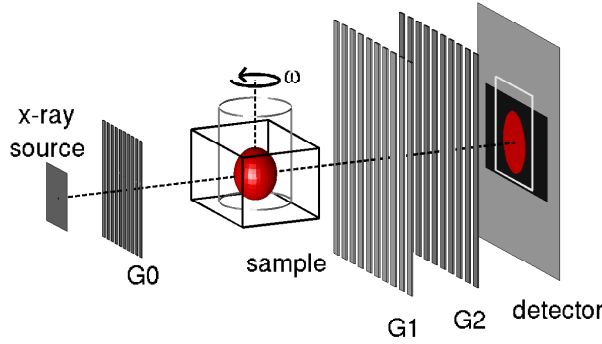


Figure 1. Schematic view of the experimental setup. The G0 grating acts as a slit array, producing parallel line sources. The sample is placed immediately in front of the interferometer, and the detector is placed immediately after.

2.1. Interferometer

For phase-contrast x-ray imaging we used a grating-based interferometer with three gratings in Talbot-Lau geometry (Pfeiffer et al. 2006). See figure 1. The setup comprises an x-ray source, one grating after the source, the sample (on a tomographic rotation stage), two gratings after the sample, and the image detector. The gratings are: source grating G0, phase grating G1 and analyzer grating G2. Grating G1 is a pure Si grating, whereas gratings G0 and G2 are Si/Au absorption gratings made by etching into a Si-wafer and subsequent electro-plating of Au as described elsewhere (David et al. 2007a).

The grating G0 is mounted close to the source, and ensures a suitable transverse coherence length of the x-ray beam for each line source created by G0. The interferometer consisting of gratings G1 and G2 is located at a distance of $L = 1.4$ m from the source. G1 has a period of $3.5 \mu\text{m}$, and a depth of $36 \mu\text{m}$ corresponding to a phase shift of π at 28 keV. Due to the Talbot self-imaging effect (Talbot 1836), interference fringes are formed at fractional Talbot distances corresponding to

$$a = j \frac{g_1^2}{8\lambda}$$

(in plane-wave geometry), where j is an odd integer, g_1 is the period of the phase grating G1 and λ is the wavelength. To account for magnification due to the divergent beam geometry of our experiment, the actual fractional Talbot distances d are rescaled by

$$d = j \frac{g_1^2}{8\lambda} \frac{L + d}{L} = \frac{La}{L - a}.$$

In the current experiment the setup was operated at the fifth fractional Talbot distance

($j = 5$) corresponding to $d = 20$ cm. The period g_2 of grating G2 was $2 \mu\text{m}$, which is equal to the interference fringe period caused by grating G1.

2.2. Data Acquisition and Processing

Differential phase-contrast images are extracted from the raw image data recorded during a phase stepping scan in the following way: A number of exposures are made while stepping the analyzer grating G2 transversely over one period of the grating. The recorded intensity is thus a function of pixel position (p_x, p_y) and grating position x_g . As the analyzer grating G2 has the same period as the interference pattern caused by G1, the exact position of the interference pattern can be extracted from the measured intensity $I(p_x, p_y, x_g)$, transmitted through G2. The shift of the interference pattern from a refracted beam relative to that of the undisturbed beam is a direct measure of the refraction angle. Knowing the angle of refraction, it is trivial to calculate the gradient of the total phase shift $\nabla\Phi = 2\pi\alpha/\lambda$, and the total phase shift by integration. By using computed tomography techniques it is then possible to quantitatively reconstruct a three-dimensional map of the refractive index: $n = 1 - \delta + i\beta$. The real part δ is related to the total electron density ρ and the wavelength λ by:

$$\delta = \frac{\rho r_0 \lambda^2}{2\pi},$$

where $r_0 = 2.82 \cdot 10^{-15}$ m is the Thomson scattering length (Als-Nielsen & McMorrow 2001). The imaginary part β of the refractive index n is related to the absorption coefficient $\mu = 4\pi\beta/\lambda$. The tomographic reconstruction of the attenuation data was carried out using standard filtered back-projection using a Ram-Lak filter, as described, e.g., in Kak & Slaney (2001). The differential phase-contrast signal was reconstructed using an imaginary filter (Hilbert transform) and back-projection, as previously described in Pfeiffer et al. (2007c) and Pfeiffer et al. (2007b).

3. Results

To test the applicability of x-ray tubes for phase-contrast CT on soft tissue, we have measured phase-contrast images of a chicken heart in a tomography setup. The heart was fixated in 4% formalin solution and kept in a cylindrical plastic container. The container was submerged in a water bath as illustrated in figure 1.

The tomography data was recorded with 16 phase steps per projection and a total of 375 projections, covering a 360° sample rotation. In this proof-of-principle experiment the exposure time was 10 seconds per frame, yielding a total exposure time of 13 hours. Figure 2 shows the conventional x-ray transmission image and the phase-contrast image from a single projection. The fact that muscle tissue and water has almost the same attenuation coefficient makes it difficult to see the heart in the standard x-ray image. But the less dense adipose tissue in the top part of the image is visible. In the differential

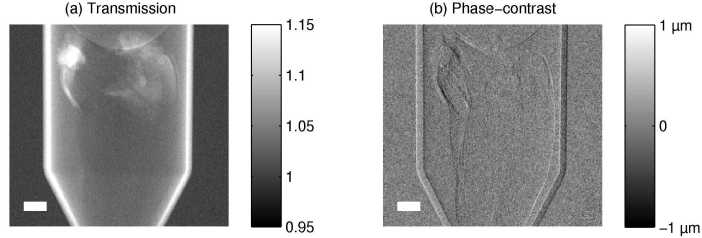


Figure 2. X-ray images of a chicken heart. (a) Conventional x-ray image, attenuation contrast. (b) Phase-contrast image. The images show a single projection, which is part of a 375 image projection data set. The images are displayed using a linear gray scale. The transmission values (a) are given relative to water. The phase-contrast values (b) are given as the transverse shift of the interference pattern in the plane of G2. The white scale bar corresponds to 5 mm.

phase-contrast image, the contour of the heart can be faintly distinguished from the surrounding water.

Though the image contrast in a single projection (figure 2) is relatively poor, images with much higher contrast can be obtained from virtually slicing the tomographically reconstructed 3D volume, owing to the increased statistics obtained through the many projections. As illustrated in figure 3(a) and 3(e), the adipose tissue visible in figure 2 is clear and distinct in the reconstructed absorption contrast image. But the signal from the heart muscle itself is still comparable to the background noise level. In the phase tomography data set, figure 3(b,c,d and f,g,h), both the adipose tissue and the heart muscle itself is clearly visible.

In the processing of the data, a flat-field correction of the beam transmitted through the water tank (40 mm thickness) without the sample in place is used to correct for inhomogeneities in the illumination and the sensitivity response of the detector. As a result the attenuation is normalized to that of water during reconstruction, and hence the data is subsequently calibrated to the table values for the index of refraction for water. The table values are: $\mu = 0.36 \text{ cm}^{-1}$ and $\delta = 2.94 \cdot 10^{-7}$ (Henke et al. 1993), respectively.

To provide a quantitative comparison of absorption contrast to phase contrast, figure 4, left panel, displays the pixel values along the red bold dashed line in figure 3(a,b,e and f). We observe that the differences in the attenuation values (μ) between the heart tissue and water are buried in the noise level, whereas they are well resolved in the corresponding phase-contrast signals (δ). The improved contrast is further exposed in figure 4, right panel, which shows a histogram representation of all pixels in the axial slices in figure 3(a) and 3(b). In the phase-contrast histogram two distinct peaks are seen at $\delta = 2.94 \cdot 10^{-7}$ and $\delta = 3.07 \cdot 10^{-7}$, corresponding to water and heart tissue, respectively. It is also noteworthy that the cylindrical sample container and adipose tissue are distinguishable in the phase-contrast signal at $\delta = 2.71 \cdot 10^{-7}$ and

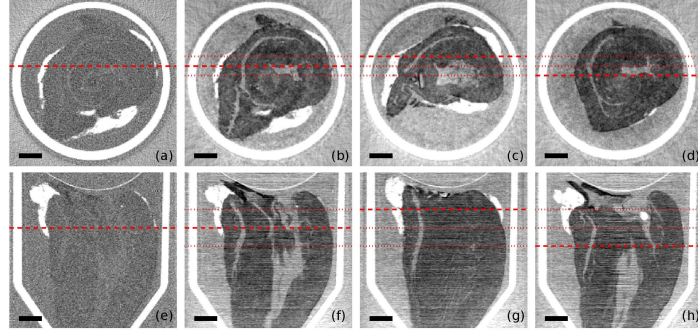


Figure 3. Slices through the reconstructed 3D tomography volume. (a) Axial slice, absorption contrast. (b,c,d) Axial slices, phase contrast. (e) Frontal slice, absorption contrast. (f,g,h) Frontal slices, phase-contrast. The images are displayed on a linear gray scale. The absorption-contrast gray scale ranges from $\mu = 0.31 \text{ cm}^{-1}$ to $\mu = 0.41 \text{ cm}^{-1}$ (symmetrically around the water peak), and the phase-contrast gray scale ranges from $\delta = 2.8 \cdot 10^{-7}$ to $\delta = 3.2 \cdot 10^{-7}$ (covers water and muscle tissue). Frontal and axial slices are vertically ordered pairwise such that they intersect in the red dashed line. Voxel values along the red dashed lines of panels (a), (b), (e) and (f) are plotted in figure 4(left panel). The black scale bar corresponds to 5 mm.

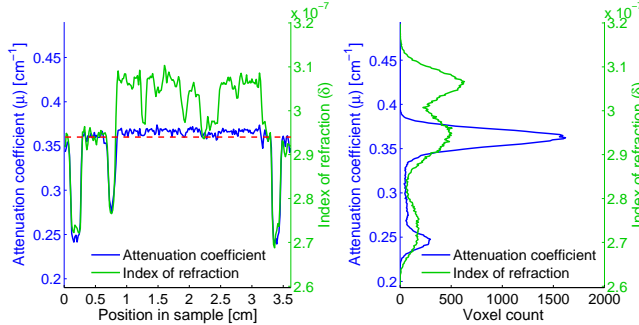


Figure 4. Left panel: Plot of absorption coefficient μ and real part of refractive index δ along the red dashed line in figure 3(a, b, e and f). Right panel: Histogram of the voxels in the entire axial slice in figure 3(a and b).

$\delta = 2.75 \cdot 10^{-7}$, respectively. The absorption histogram has only two peaks, one at $\mu = 0.36 \text{ cm}^{-1}$ corresponding to water/heart, and one at $\mu = 0.24 \text{ cm}^{-1}$, corresponding to adipose tissue/plastic. This clearly illustrates far better contrast using the phase signal.

Note that the y -axis scales on left and right panels of figure 4, are identical.

4. Conclusions

In summary, we have presented the first, grating-based experimental soft-tissue phase-contrast computed tomography results using a conventional x-ray tube source with millimeter-sized focal spot. The results clearly demonstrate the advantageous contrast attainable through phase-contrast imaging over conventional attenuation-based approaches, and present a significant step forward toward future medical applications. We have particularly shown that a quantitative analysis of the sample composition is feasible on the basis of the phase-contrast data, even though the absorption data hardly provides any contrast at all. More precisely, we have demonstrated that quantitative electron densities can be obtained from the measured δ values. For a chicken heart test sample fixated in formalin, we deduced electron densities of $\rho = 3.49 \cdot 10^{23} \text{ cm}^{-3}$ for the muscle tissue, $\rho = 3.13 \cdot 10^{23} \text{ cm}^{-3}$ for the adipose tissue and $\rho = 3.08 \cdot 10^{23} \text{ cm}^{-3}$ for the plastic cylinder, when calibrating against an electron density for water of $\rho = 3.34 \cdot 10^{23} \text{ cm}^{-3}$.

We expect that future work with an improved setup (more powerful x-ray tube, higher efficiency detector, and better grating structures) will allow for the feasibility of first in-vivo, pre-clinical demonstration experiments.

5. References

- Als-Nielsen J & McMorrow D 2001 *Elements of Modern X-ray Physics* John Wiley & Sons Ltd.
 Beckmann F, Heise K, Kolsch B, Bonse U, Rajewsky M F, Bartscher M & Biermann T 1999 *Biophysical Journal* **76**, 98–102.
 Bonse U & Hart M 1965 *Appl. Phys. Lett.* **6**, 155–156.
 Bravin A 2003 *J. Phys. D: Appl. Phys.* **36**, A24–A29.
 Clauser J F 1998 ‘Us patent no. 5,812,629: Ultrahigh resolution interferometric x-ray imaging’.
 Cloetens P, Mache R, Schlenker M & Lerbs-Mache S 2006 *Proc. Nat. Acad. Sci. USA* **103**(39), 14626–14630.
 Cormack A M 1963 *J. Applied Physics* **34**, 2722.
 David C, Bruder J, Rohbeck T, Grunzweig C, Kottler C, Diaz A, Bunk O & Pfeiffer F 2007a *Microelectron. Eng.* **84**, 1172–1177.
 David C, Nöhammer B, Solak H H & Ziegler E 2002 *Appl. Phys. Lett.* **81**(17), 3287–3289.
 David C, Weitkamp T, Pfeiffer F, Diaz A, Bruder J, Rohbeck T, Groso A, Bunk O, Stampaoni M & Cloetens P 2007b *Spectrochim. Acta B* **62**, 626–630.
 Henke B L, Gullikson E M & Davis J C 1993 *Atomic Data and Nuclear Data Tables* **54**, 181–342.
 Hounsfield G N 1973 *Br. J. Radiol.* **46**(552), 1016–1022.
 Kak A C & Slaney M 2001 *Principles of Computerized Tomographic Imaging* Society for Industrial and Applied Mathematics.
 Keyriläinen J, Fernandez M & Suortti P 2002 *Nucl. Instr. Meth. A* **488**, 419–427.
 Mayo S, Davis T, Gureyev T, Miller P, Paganin D, Pogany A, Stevenson A & Wilkins S 2003 *Opt Express* **11**(19), 2289–2302.
 Momose A, Kawamoto S, Koyama I, Hamaishi Y, Takai K & Suzuki Y 2003 *Jpn. J. Appl. Phys.* **42**, L866–L868.
 Momose A, Yashiro W, Takeda Y, Suzuki Y & Hattori T 2006 *Jpn. J. Appl. Phys.* **45**(6A), 5254–5262.
 Pfeiffer F, Bunk O, David C, Bech M, Duc G L, Bravin A & Cloetens P 2007a *Phys. Med. Biol.* **52**, 6923–6930.

- Pfeiffer F, Bunk O, David C, Bech M, Duc G L, Bravin A & Cloetens P 2008 *in* ‘Developments in X-Ray Tomography VI’ Vol. 7078 Proc. SPIE p. 707815.
- Pfeiffer F, Bunk O, Kottler C & David C 2007b *Nucl. Instr. Meth. A* **580**, 925–928.
- Pfeiffer F, Kottler C, Bunk O & David C 2007c *Phys. Rev. Lett.* **98**, 108105.
- Pfeiffer F, Weitkamp T, Bunk O & David C 2006 *Nat. Phys.* **2**, 258–261.
- Talbot H F 1836 *Phil. Mag.* **9**, 401.
- Weitkamp T, David C, Bunk O, Bruder J, Cloetens P & Pfeiffer F 2008 *European Journal of Radiology* **68**(3), 13–17.
- Weitkamp T, Diaz A, David C, Pfeiffer F, Stampaponi M, Cloetens P & Ziegler E 2005 *Opt Express* **12**(16), 6296–6304.
- Zhong Z, Thomlinson W, Chapman D & Sayers D 2000 *Nucl. Instr. Meth. A* **450**, 556–567.

Publication VII

Journal of Applied Physics (2009)

Franz Pfeiffer, **Martin Bech**, Oliver Bunk, Tilman Donath, Beat Henrich, Phillip Kraft and Christian David

X-ray dark-field and phase-contrast imaging using a grating interferometer

Journal of Applied Physics 105 (2009)

Accepted for publication.

X-ray dark-field and phase-contrast imaging using a grating interferometer

F. Pfeiffer,^{1,a)} M. Bech,² O. Bunk,³ T. Donath,³ B. Henrich,³ P. Kraft,³ and C. David³

¹Department of Physics, Technische Universität München, 85748 Garching, Germany

²Niels Bohr Institute, University of Copenhagen, 2100 Copenhagen, Denmark

³Paul Scherrer Institut, 5232 Villigen PSI, Switzerland

(Received 14 April 2008; accepted 8 August 2008; published online 19 May 2009)

In this letter, we report results obtained with a recently developed approach for grating-based x-ray dark-field imaging [F. Pfeiffer *et al.*, Nat. Mater. **7**, 134 (2008)]. Since the image contrast is formed through the mechanism of small-angle scattering, it provides complementary and otherwise inaccessible structural information about the specimen at the micron and submicron length scales. Our approach is fully compatible with conventional transmission radiography and the grating-based hard x-ray phase-contrast imaging scheme [F. Pfeiffer *et al.*, Nat. Phys. **2**, 258 (2006)]. Since it can be used with standard x-ray tube sources, we envisage widespread applications to x-ray medical imaging, industrial nondestructive testing, or security screening. © 2009 American Institute of Physics. [DOI: [10.1063/1.3115639](https://doi.org/10.1063/1.3115639)]

I. INTRODUCTION

Visible light microscopy is a standard and widely utilized tool with a broad range of applications in science, industry, and everyday life. Besides standard bright-field imaging, many more contrast mechanisms have been developed, and dark-field imaging, phase-contrast, confocal, and fluorescence microscopies are routine methods in today's light microscopy applications.¹ It is not surprising that this development has stimulated a similar progress in imaging applications with other forms of radiation. In electron microscopy, for example, where the initial electron microscope image was produced in the early 1930s, dark-field imaging was introduced in the late 1930s,² and imaging based on phase contrast in the 1940s.³

In x-ray microscopy or, more generally, x-ray imaging, the development of a similar range of contrast modalities proceeded much more slowly and is still a very active field of research. Despite the early pioneering work on x-ray interferometry by Bonse and Hart⁴ in the 1960s, the majority of phase-contrast imaging^{4–13} and dark-field imaging^{14–20} methods were introduced in the late 1990s. The development of such advanced imaging methods is particularly difficult for hard x rays (with energies in the multi-keV range) because of the lack of efficient x-ray optics. Existing hard x-ray dark-field imaging methods, for example, rely on the use of crystal optics that can only accept a very narrow energy band width ($\approx 0.01\%$) and angular divergence (≈ 1 arc sec).^{6,17–20} This is why dark-field or scattering-based imaging is currently restricted in practice to applications at highly brilliant synchrotron x-ray sources^{16–20} and is not available for widespread applications that require a method applicable to standard x-ray tubes. In the following we show results obtained with our recently developed grating-based dark-field imaging approach.²¹

II. PRINCIPLES

Figure 1 shows our experimental arrangement. It consists of a source grating G0, a phase grating G1, and an analyzer absorption grating G2 [Fig. 1(a)]. The source grating (G0), typically placed close to the x-ray tube, is an aperture mask with transmitting slits. It creates an array of periodically repeating line sources and effectively allows the use of relatively large, i.e., square-millimeter-sized x-ray sources, without compromising the coherence requirements

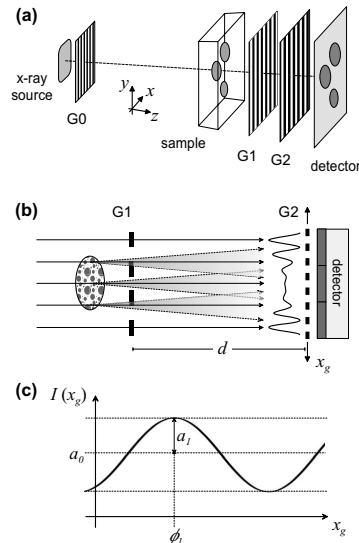


FIG. 1. X-ray grating interferometer. (a) Setup with a source grating G0, a phase grating G1, and an analyzer absorption grating G2. (b) Through the Talbot effect a linear periodic fringe pattern is created behind G1 in the plane of G2. (c) Intensity modulation detected in a detector pixel when one of the gratings is scanned along x_g . A loss in the amplitude of the oscillation due to the scattering of x rays in the specimen (degradation of the coherent wave front) can be used to extract images with dark-field contrast.

^{a)}Author to whom correspondence should be addressed. Electronic mail: franz.pfeiffer@ph.tum.de.

of the arrangement formed by G1 and G2.⁵ The image contrast itself is formed via the combined effect of the two gratings G1 and G2. The second grating (G1) acts as phase mask and imprints periodic phase modulations onto the incoming wave field. Through the Talbot effect,^{22–25} the phase modulation is transformed into an intensity modulation in the plane of G2, forming a linear periodic fringe pattern perpendicular to the optical axis and parallel to the lines of G1 [Fig. 1(b)]. The third grating (G2) with absorbing lines and the same periodicity and orientation as the fringes created by G1 is placed in the detection plane, immediately in front of the detector. When one of the gratings is scanned along the transverse direction x_g , the intensity signal $I(m,n)$ in each pixel (m,n) in the detector plane oscillates as a function of x_g [Fig. 1(c)].

The fundamental idea of the method presented here is to evaluate the local changes in the oscillation $I(m,n,x_g)$ induced by an object and determine from these several imaging signals, including the dark-field contrast. To analyze these changes quantitatively, we write the intensity oscillation for each detector pixel in a Fourier series

$$\begin{aligned} I(m,n,x_g) &= \sum_i a_i(m,n) \cos[i k x_g + \phi_i(m,n)] \\ &\approx a_0(m,n) + a_1(m,n) \cos[k x_g + \phi_1(m,n)], \quad (1) \end{aligned}$$

where a_i are the amplitude coefficients, ϕ_i are the corresponding phase coefficients, $k = 2\pi/p_2$, and p_2 is the period of G2. Then the normalized average transmission of the specimen in each detector pixel is given by $T(m,n) = a_0^s(m,n)/a_0^r(m,n)$, where the superscripts s and r denote the values measured with the specimen in place (s) and as a reference without (r). Note that $T(m,n)$ is identical to what would be measured with a conventional x-ray radiography setup. Furthermore, we have previously shown⁵ that differential phase-contrast images can be obtained by analyzing the lateral shift of intensity modulation, i.e., the quantity $\phi_1(m,n)$ in Eq. (1).

Dark-field images are based on the local scattering power of the sample and can also be obtained with such a setup. In terms of visible-light Fourier optics, dark-field illumination removes the zeroth order (unscattered light) from the diffraction pattern formed at the rear focal plane of the objective. This results in an image formed exclusively from higher angle diffraction intensities scattered by the specimen. Quite similarly, information about the scattering power of the specimen is contained in our case in the higher order, i.e., the first Fourier component of $I(m,n,x_g)$. More precisely, the amplitude of the first Fourier component, a_1 , is decreased when x rays are scattered or reflected at internal inhomogeneities or interfaces on their passage through the specimen [Fig. 1(c)].

For a quantitative description of this effect, we first define the normalized oscillation amplitude, the visibility of the intensity modulation of $I(m,n,x_g)$, by the ratio

$$V'(m,n) \equiv \frac{I_{\max}^r - I_{\min}^r}{I_{\max}^r + I_{\min}^r} = \frac{a_1^r(m,n)}{a_0^r(m,n)}, \quad (2)$$

see Eq. (1). The relative decrease in the visibility due to the specimen can be quantified by defining the normalized visibility

$$V(m,n) \equiv \frac{V^s(m,n)}{V'(m,n)} = \frac{a_0^r(m,n)a_1^s(m,n)}{a_0^s(m,n)a_1^r(m,n)}. \quad (3)$$

For homogeneous specimens, i.e., for samples with negligible small-angle x-ray scattering (SAXS) contribution, the value for the visibility remains unchanged, and $V(m,n)=1$. But specimens, which, e.g., exhibit strong internal density fluctuations on micrometer length scales and thus produce a strong SAXS signal, show a significant decrease in the visibility and yield values of $V < 1$.²⁴ More generally, we note that the quantity $V(m,n)$ is an inverse measure for the effective integrated local small (and ultrasmall)-angle scattering power of the sample and therefore refer to it as a “dark-field” image of the specimen. Most simply this can be understood by considering that the amplitude of the oscillations in $I(m,n,x_g)$ is most effectively reduced by x rays scattered from the object at wave vectors corresponding to diffraction angles defined by the ratio of half the period of G2 over the distance between the object and G2 [see also Fig. 1(b)].

III. EXPERIMENTAL

The experiments were carried out on a Seifert ID 3000 x-ray generator operated at 40 kV/25 mA. We used a tungsten (W) line focus tube (DX-W8×0.4-L) with a focus size of 8(horizontal)×0.4(vertical) mm². Due to the inclination of the target with respect to the optical axis of 6°, the effective source size was 0.8(h)×0.4(v) mm².

The gratings were fabricated by a process involving photolithography, deep etching into silicon, and electroplating of gold.²⁶ The size of the active area was limited in the present study by the processing technology (100 mm wafers) to 64×64 mm². The gratings had periods of $p_0=14$ μm, $p_1=3.5$ μm, and $p_2=2.0$ μm. The heights of the grating structures, which were optimized for a mean x-ray energy of 28 keV, were 42 μm (G0), 35 μm (G1), and 26 μm (G2). The distance between G0 and G1 was 1.4 m and between G1 and G2 0.2 m, corresponding to the fifth fractional Talbot distance.²⁵

The images were recorded using a PILATUS 100 K pixel detector.²⁷ The module consists of an array of 487×195 pixels with a pixel size of 0.172×0.172 mm². For the results displayed in Fig. 3, several images were stitched together to increase the effective field of view. The quantum detection efficiency is determined by the probability of absorbing an x ray in the 320 μm thick Si sensor and is ≈10% (at 28 keV). For the results shown in Figs. 2 and 3, a series of eight individual images with exposure times of 10 s each was recorded.

To extract the dark-field, phase-contrast, and absorption-contrast signals from the measured intensity modulation $I(m,n,x_g)$, one-dimensional discrete fast Fourier transforms were computed for each pixel. The resulting values for the

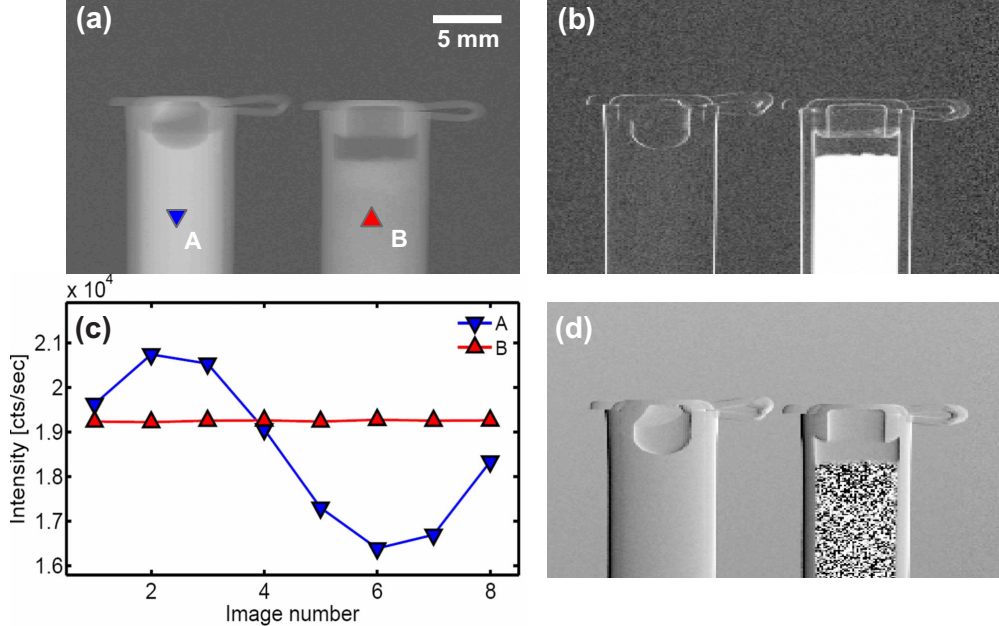


FIG. 2. (Color online) X-ray images of a test sample containing two plastic containers filled with a liquid (water, left, A) and a powder (sugar, right, B). (a) Conventional x-ray transmission image. (b) Dark-field image of the same sample. (c) Intensity oscillations observed in detector pixels corresponding to two regions of the sample, extracted from a series of eight images taken at different values of x_g (averaged over 50 pixels). (d) Differential phase-contrast image.

Fourier coefficients were normalized to the corresponding values obtained without specimen in place. On a standard personal computer (1.7 GHz processor, 2 Gbyte memory), the processing time needed for a series of eight images with 10^5 pixels was on the order of a few seconds.

IV. RESULTS

Figure 2 displays the experimental results obtained for a test sample comprising two plastic containers filled with a liquid (water) and a powder (sugar). The conventional transmission image is shown in Fig. 2(a), the dark-field image in Fig. 2(b), and the differential phase-contrast image in Fig. 2(d). The two substances (water and sugar) both absorb some fraction of the incident x-ray beam and therefore show up in the transmission image [Fig. 2(a)]. In contrast, a quite different picture is observed in the dark-field image [Fig. 2(b)], where only the powder sample (and the edges of the plastic containers) produced a strong contrast. This is because the microscopic density fluctuations present in the powder produce a strong small-angle scattering signal. Thus the intensity modulations in $I(m, n, x_g)$ [Fig. 2(c)] are lowered significantly, and a strong contrast is produced in the the dark-field image [Fig. 2(b)]. The liquid, on the other hand, shows no significant contributions to the dark-field signal since water is a homogeneous material with essentially no density fluctuations on the relevant length scales. The fact that the powder very effectively lowers the visibility in the corresponding pixels is also reflected in the differential phase-contrast image shown in Fig. 2(d). In the region, where the visibility is

almost zero, the algorithm can no longer determine the phase-contrast signal correctly and yields a random distribution of black and white pixels [behind the strongly scattering powder, see Fig. 2(d)]. The small-angle scattering signal as recorded in the dark-field image is particularly sensitive to density variations in the object on the length scale of a few tenths of nanometers to several micrometers. It naturally complements the length scales which can be imaged directly by radiographic methods into the submicrometer range.

Figure 3 displays results of imaging a biological specimen, i.e., the wing of a blackbird (*postmortem*). The conventional absorption-contrast image is shown in Fig. 3(a), the dark-field image in Fig. 3(b), and the phase-contrast image in Fig. 3(c). Note that, since all three images were obtained from the same data set, the radiation dose was identical in all three cases. In agreement with what was observed in the images of the test sample shown in Fig. 2, we find that also in this biological specimen the boundaries and interfaces produce a strong signal in the dark-field image [see Fig. 3(b)]. This is particularly reflected in the high contrast produced by the detailed fine structure of, for example, the feathers in the wing. They obviously consist of a light, but highly structured and strongly scattering fiber network since they are clearly visible in the dark-field contrast [Fig. 3(b)]. These details are difficult to see in the absorption image [Fig. 3(a)]. The bones in the wing, however, are very nicely resolved in the absorption image [Fig. 3(a)]. The phase-contrast image [Fig. 3(c)] complements the details visible in the dark-field and absorption image by highlighting, in par-

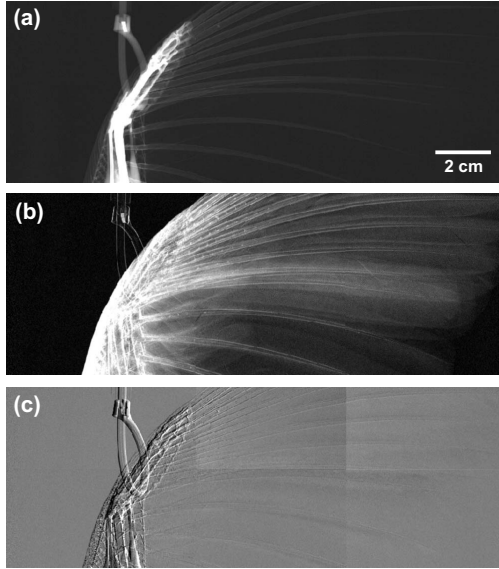


FIG. 3. *Postmortem* images obtained for a biological specimen (wing of a blackbird). (a) Conventional transmission image. (b) Dark-field image. (c) Differential phase-contrast image.

ticular, the edges of the core structure of the wing.

V. SUMMARY AND OUTLOOK

In summary, we have shown how a grating interferometer can be used to simultaneously produce dark-field, phase-contrast, and the conventional absorption images with hard x-rays. We have demonstrated that, in contrast to existing crystal analyzer based methods,^{17–20} our method can efficiently be implemented with a standard x-ray tube source. The approach is potentially interesting for a wide range of applications including medical imaging,²⁰ security screening,²⁸ industrial nondestructive testing,²⁹ food inspection, and small animal imaging. In the future, a further increase in the sensitivity of the method could also provide contrast between healthy and diseased breast tissue since breast tumors exhibit a different small-angle scattering signature than the healthy adipose matrix.^{30,31} Generally, we believe that the method is of particular interest for challenging x-ray imaging applications because it simultaneously provides dark field, transmission, and differential phase contrast, thus providing maximum information about the specimen. Finally, this approach can be extended into three dimensions using computer tomographic techniques,³² coupled with a synchrotron source to yield micrometer-resolution hard x-ray dark-field images,³³ or implemented with other types of radiation, such as neutrons.³⁴

ACKNOWLEDGMENTS

We gratefully acknowledge C. Grünzweig for the grating fabrication, J. Herzen for assistance during the experiments, and Ch. Brönnimann and E. F. Eikenberry for providing the detector. F. P. acknowledges support through the DFG Cluster of Excellence Munich-Center for Advanced Photonics.

- ¹D. B. Murphy, *Fundamentals of Light Microscopy and Electronic Imaging* (Wiley, New York, 2001).
- ²M. von Ardenne, Z. Tech. Phys. (Leipzig) **19**, 407 (1938).
- ³E. G. Ramberg, J. Appl. Phys. **20**, 441 (1949).
- ⁴U. Bonse and M. Hart, Appl. Phys. Lett. **6**, 155 (1965).
- ⁵F. Pfeiffer, T. Weitkamp, O. Bunk, and C. David, Nat. Phys. **2**, 258 (2006).
- ⁶T. J. Davis, D. Gao, T. E. Gureyev, A. W. Stevenson, and S. W. Wilkins, Nature (London) **373**, 595 (1995).
- ⁷V. N. Ingal and E. A. Beliaevskaya, J. Phys. D: Appl. Phys. **28**, 2314 (1995).
- ⁸A. Snigirev, I. Snigireva, V. Kohn, S. Kuznetsov, and I. Schelokov, Rev. Sci. Instrum. **66**, 5486 (1995).
- ⁹S. W. Wilkins, T. E. Gureyev, D. Gao, A. Pogany, and A. W. Stevenson, Nature (London) **384**, 335 (1996).
- ¹⁰D. Chapman, Phys. Med. Biol. **42**, 2015 (1997).
- ¹¹A. Momose, Jpn. J. Appl. Phys., Part 1 **44**, 6355 (2005).
- ¹²A. Momose, W. Yashiro, Y. Takeda, Y. Suzuki, and T. Hattori, Jpn. J. Appl. Phys., Part 1 **45**, 5254 (2006).
- ¹³T. Weitkamp, A. Diaz, C. David, F. Pfeiffer, M. Stampanoni, P. Cloetens, and E. Ziegler, Opt. Express **13**, 6296 (2005).
- ¹⁴G. R. Morrison and M. T. Browne, Rev. Sci. Instrum. **63**, 611 (1992).
- ¹⁵H. N. Chapman, C. Jacobsen, and S. Williams, Ultramicroscopy **62**, 191 (1996).
- ¹⁶Y. Suzuki and F. Uchida, Rev. Sci. Instrum. **66**, 1468 (1995).
- ¹⁷E. Pagot, S. Fiedler, P. Cloetens, A. Bravin, P. Coan, K. Fezzaa, J. Baruchel, and J. Härtwig, Appl. Phys. Lett. **82**, 3421 (2003).
- ¹⁸L. E. Levine and G. G. Long, J. Appl. Crystallogr. **37**, 757 (2004).
- ¹⁹M. Ando, E. Hashimoto, H. Hashizume, K. Hyodo, H. Inoue, T. Kunisada, A. Maksimenko, K. Mori, E. Rubenstein, J. Roberson, D. Shimaoc, H. Sugiyama, K. Takeda, F. Toyofuku, E. Ueno, K. Umetani, H. Wada, and W. Pattanaesriwasa, Nucl. Instrum. Methods Phys. Res. A **548**, 1 (2005).
- ²⁰D. Shima, H. Sugiyama, T. Kunisada, and M. Ando, Appl. Radiat. Isot. **64**, 868 (2006).
- ²¹F. Pfeiffer, M. Bech, O. Bunk, P. Kraft, E. F. Eikenberry, C. Brönnimann, C. Grünzweig, and C. David, Nature Mater. **7**, 134 (2008).
- ²²A. W. Lohmann and D. E. Silva, Opt. Commun. **2**, 413 (1971).
- ²³S. Yokozeki and T. Suzuki, Appl. Opt. **10**, 1575 (1971).
- ²⁴F. Pfeiffer, O. Bunk, C. Schulze-Briese, A. Diaz, T. Weitkamp, C. David, J. F. van der Veen, I. Vartanyants, and I. K. Robinson, Phys. Rev. Lett. **94**, 164801 (2005).
- ²⁵T. Weitkamp, C. David, C. Kottler, O. Bunk, and F. Pfeiffer, SPIE Int. Soc. Opt. Eng. **6318**, 28 (2006).
- ²⁶C. David, J. Bruder, T. Rohbeck, C. Grünzweig, C. Kottler, A. Diaz, O. Bunk, and F. Pfeiffer, Microelectron. Eng. **84**, 1172 (2007).
- ²⁷M. Bech, O. Bunk, C. David, P. Kraft, C. Brönnimann, E. F. Eikenberry, and F. Pfeiffer, Appl. Radiat. Isot. **66**, 474 (2008).
- ²⁸G. Harding, Radiat. Phys. Chem. **71**, 869 (2004).
- ²⁹G. Harding and B. Schreiber, Radiat. Phys. Chem. **56**, 229 (1999).
- ³⁰M. Fernandez, J. Keyriläinen, R. Serimaa, M. Torkkeli, M.-L. Karjalainen-Lindsberg, M. Tenhunen, W. Thomlinson, V. Urban, and P. Suortti, Phys. Med. Biol. **47**, 577 (2002).
- ³¹M. Fernández, J. Keyriläinen, R. Serimaa, M. Torkkeli, M.-L. Karjalainen-Lindsberg, M. Leidenius, K. von Smitten, M. Tenhunen, S. Fiedler, A. Bravin, T. M. Weiss, and P. Suortti, Phys. Med. Biol. **50**, 2991 (2005).
- ³²F. Pfeiffer, C. Kottler, O. Bunk, and C. David, Phys. Rev. Lett. **98**, 108105 (2007).
- ³³F. Pfeiffer, O. Bunk, C. David, M. Bech, G. Le Duc, A. Bravin, and P. Cloetens, Phys. Med. Biol. **52**, 6923 (2007).
- ³⁴F. Pfeiffer, C. Grünzweig, O. Bunk, G. Frei, E. Lehmann, and C. David, Phys. Rev. Lett. **96**, 215505 (2006).